High-Order Finite-Volume CENO Scheme for Large-Eddy Simulation of Premixed Flames

by

Luiz Tobaldini Neto

A thesis submitted in conformity with the requirements
for the degree of Doctor of Philosophy
Graduate Department of Aerospace Science and Engineering
University of Toronto

Abstract

High-Order Finite-Volume CENO Scheme for Large-Eddy Simulation of Premixed Flames

Luiz Tobaldini Neto
Doctor of Philosophy
Graduate Department of Aerospace Science and Engineering
University of Toronto
2019

A novel, parallel, high-order, central essentially non-oscillatory (CENO), cell-centered, finite-volume scheme is developed and applied to large-eddy simulation (LES) of turbulent premixed flames. The high-order CENO finite-volume scheme is applied to the solution of the Favre-filtered Navier-Stokes equations governing turbulent flows of a fully compressible reactive mixture on a three-dimensional, multi-block, body-fitted, computational mesh consisting of hexahedral volume elements. The CENO method uses a hybrid reconstruction approach based on a fixed central stencil. The discretization of the inviscid fluxes combines an unlimited high-order least-squares reconstruction technique based on the optimal central stencil with a monotonicity-preserving, limited, linear, reconstruction algorithm. Switching in the hybrid procedure is determined by a smoothness indicator such that the unlimited high-order reconstruction is retained for smooth solution content that is fully resolved and reverts to the limited lower-order scheme, enforcing solution monotonicity, for regions with abrupt variations (i.e., discontinuities and under-resolved regions). The high-order viscous fluxes are computed to the same order of accuracy as the hyperbolic fluxes based on a high-order accurate cell interface gradient derived from the unlimited, cell-centered, reconstruction. The proposed cell-centered finite-volume scheme is formulated for three-dimensional multi-block mesh consisting of generic hexahedral cells and applied to LES of premixed flames. For the reactive flows of interest here, a flamelet-based subfilter-scale (SFS) model is used to describe the unresolved influences of interaction between the turbulence and combustion. This SFS combustion model is based on a presumed conditional moment (PCM) approach in conjunction with flame prolongation of intrinsic low-dimensional manifold (FPI) tabulated chemistry. Numerical results are discussed for a laboratory-scale lean

premixed methane-air Bunsen-type flame. The performance of the proposed high-order scheme for turbulent reactive flows is analysed by a systematic mesh refinement study using different spatial orders of accuracy.

Dedication

To Hellen and Lara

Acknowledgements

It is a hard task to make sure all the people who somehow contributed to this work are properly acknowledged. It is a pleasure to try it, despite the risks of failing.

I would like to start thanking my supervisor, Prof. Clinton Groth: for the amazing opportunity and all the structure he offered me, for his untiring guidance, for the excellent classes and for his always precise observations, from soccer to turbulence. Also, I would like to thank the members of my committee for the fruitful discussions and orientation: Prof. Steinberg, Dr. Sampath and Prof. Gülder. I also thank Prof. Gülder and Prof. Gottlieb for the thorough revision of my thesis, Prof. Zingg for the great talks and classes and Prof. Damaren for all the support and kind assistance provided. I acknowledge and thank the SciNet HPC Consortium, where all the computations presented here were performed. I also recognize the staff at UTIAS, who allow our academic lives to flow much more smoothly. In particular, I express my gratitude to the patient ears and big hearts of Gail Holiwell, Carmela Versace and Joan DaCosta with their remarkable dedication to the students. I would like to thank all my lab colleagues during those 4 years in Canada. Unfortunately I can not name them all here, but I must mention the brilliant minds of Marc Charest and Lucian Ivan for all the knowledge and helpful insights shared and also Jon West and Nasim Shahbazian for being so close, sharing thoughts, views and coffees.

My sincerest appreciation to Embraer S.A., Mr. Mario Lott and Dr. Luis Carlos de Castro Santos, for their views on education and for all the support and assistance I received, in many forms at all moments. I thank them above all, for the encouragement and camaraderie. Also, thanks to those at Embraer whose advices and presence were always inspiring me, in special to my friends Antonio, Celso, Trapp, Areal. I also acknowledge and thank CNPq-Brazil for the financial support received. I also would like to thank Prof. Marcos Pimenta, for all the accurate advices.

Thanks to those who transformed my family's experience in Canada and are forever in our lives: Fabio, Veka, Ricardo, Ana, Vivi, Domingo. I also sincerely thank my friends and family back home, always so present.

My deepest gratitude to my dear mother and father for presenting me the world, to my beloved, patient Hellen, for sharing with me her world, and to my dearest, little Lara, for re-imagining all worlds.

Luiz Tobaldini Neto

Toronto, 2018

Contents

List of Tables

List of Figures

Chapter 1

Introduction

In this introductory chapter the motivation for the thesis is discussed, starting with the importance of combustion to our society and a brief discussion of the sustainability and environmental impacts associated with this chemical process. A brief comment on aviation biofuels is also made, emphasizing the fact that some sustainable alternatives to fossil fuels would still rely on combustion as a means of energy transformation. The chapter is concluded recognizing that, due to the complexity of practical combustion problems, the importance of computational simulation is increasing going forward and there is an increasing need for the development of faster, more accurate techniques for simulating combustion problems. The introduction establishes the starting point of this research. The performance of a high-order numerical scheme in the simulation of combustion via large-eddy simulation is then investigated in the remainder of the thesis for a laboratory-scale, turbulent, premixed flame.

1.1 Motivations

1.1.1 Importance of Combustion Science

Fossil fuels, and particularly oil are vital sources of energy to the world and will remain so for many years to come, even under the most optimistic assumptions about the pace of development of alternative technologies to fossil fuels. A recent report from the International Energy Agency IEA [4] predicts that by 2035, consumption of biomass (for power generation) and biofuels will grow four-fold, and one of the main forms of conversion of the energy stored in fossil fuels, biomass and biofuels is through combustion. An important line of research related to sustainable energy generation is, therefore, related to the better understanding of combustion systems and fuels, identifying alternative fuels, and exploring more efficient ways to burn the fuels, and

make use of their stored chemical energy. In the United States, it is foreseen that the internal combustion engine will remain the primary driver of transportation systems for the next 30-50 years [5], even taking into account the increasing presence of hydrogen-fueled and electric vehicles. There is therefore a need for the careful examination of optimally efficient and clean combustion systems for the 21^{st} century.

Additionally it is noted that, in spite of its relatively long history, combustion is considered to be among the most complex technologies, and, consequently, one of the least developed of modern engineering systems. With a correct sense of opportunity, this statement indicates that, while there remain significant challenges, there are also many opportunities for improvement and innovation in the field of combustion science.

1.1.2 Environmental Impact of Combustion

Every form of energy transformation has some level of impact on the surrounding environment. This fact is a direct consequence of the first and second laws of thermodynamics. Depending on the type of system used to transform energy, most of this impact may be confined to the immediate surroundings, but in other cases the impact may be traced to global scales. It is part of an engineer's task to evaluate and manage these impacts having in mind the social, economical and environmental aspects of the problem. Combustion based energy conversion systems are no different and the recent efforts towards sustainable development necessarily involve a better understanding and reduction of the impacts related to these systems. Particularly, in fossil fuel based combustion systems, the most direct environmental impact is that of the products and undesirable emissions of the reactions.

Combustion of fossil fuels and biofuels is based on the oxidation of the fuel's carbon and hydrogen contents into mostly carbon dioxide and water. Despite not being directly harmful to human health or the environment, the increase in human produced carbon dioxide concentration in the atmosphere has been shown to be correlated with an increase in the global temperature of the Earth [6]. Incomplete oxidation may also lead to the production of carbon monoxide, which has direct harmful effects to the human respiratory system. Nitrogen oxides, NO_x, are also formed during the combustion process and can contribute to the formation of ozone in the troposphere, being also harmful to human health due to their effects on breathing and the respiratory system, damage to lung tissue, including the potential for premature death. There are other forms of impact related to fuel production and/or extraction, transport, storage and even related to the manufacture of the devices that will actually use a particular fuel. Emissions and pollutants are, as said before, a direct consequence of the combustion process and an appropriate modelling of combustion can contribute greatly to a better understanding of their environmental impacts.

1.1.3 Sustainable Aviation and the Use of Alternative Fuels

It is foreseen that the aviation industry will have, in the next 20-40 years, a transition towards the use of more sustainable biofuels in place of petroleum based jet fuels [7]. Sustainable alternative fuels are defined within the context of the International Civil Aircraft Organization (ICAO) as fuels that are consistent with the environmental, social and economic pillars of sustainability and are also fuels that would have a lower life cycle greenhouse gas (GHG) footprint than conventional jet fuel [8]. One important requirement for alternative fuels in the short to medium term is that they should be fully compatible with current aircraft and fuelling infrastructure, *i.e.*, they should be *drop-in* fuels. In recent years, aircraft and engine manufacturers have successfully performed demonstration flights using biofuels, usually in combination with regular jet fuel [7]. For example, Azul Airlines in Brazil used a renewable fuel (Amyris, AMJ 700) on a demonstration flight with an Embraer 195 jet, in June 2012 [9]. There are several challenges involved in the process of making alternative fuels viable as a drop-in option and, among them, are the need to ensure that any alternative fuel delivers the same level of suitability and quality as conventional fuels. A better understanding of the properties of these fuels requires intensive testing and experimentation. These assessments could also strongly benefit from the support of numerical simulations.

1.2 Need for High-Fidelity Analysis Tools

Combustor development is still largely performed by direct testing in experimental rigs, prototypes or even in in-service engines and power plants. According to a recent review by Bilger [10], computer modelling of complete, full geometry combustion systems is still at an initial stage and is only used peripherally in the development of new combustors. The proper (accurate and cost effective) modelling of turbulence chemistry interactions is considered one of the main challenges in numerical combustion modelling.

Computational simulation is the technique of using numerical (computational) algorithms representing mathematical models to simulate physical or other observable phenomenon using a computer, and is a very important tool in modern engineering and science. Being able to simulate a system or phenomenon based on computational modelling has numerous advantages. Simulations can dramatically reduce the number of required experiments, allowing for significant cost savings. Also, simulations may allow the developer to explore the operational envelope of a system without safety concerns, since potentially dangerous situations can be analyzed in a synthetic environment. In many situations, like in turbulence and combustion research, simulations may offer insights into non-measurable phenomena and act as a complementary tool for

the analysis of experimental results.

It is important, however, to take into account the relation between cost and accuracy of any simulation. The benefits may become questionable if the model does not represent the reality properly or if the resulting answer obtainable with a computer model is too costly; either taking too much time or requiring too much computational power that is not compatible with the available resources, particularly in an industrial setting.

Computational Fluid Dynamics (CFD) is the term generally applied to any method of dealing with the solution of fluid dynamics problems with the support of computers. The Navier-Stokes equations are a set of coupled, non-linear partial differential equations (PDE's) which are the usual model for most of industrial and practical flows of interest, where the continuum assumption holds. Other approaches like moment closures [11] or particle collision methods [12] can theoretically be used but are generally more expensive for the flows of practical interest in industry and in this work and are therefore reserved for regimes in which the continuum equation assumption fails and the Navier-Stokes equations breakdown.

When dealing with the numerical solution of the three-dimensional Navier-Stokes equations, three main classes of schemes are generally considered: finite-difference methods, finite-element methods and finite-volume methods. All of these methods rely on a discretization (sub-division) of the problem domain into smaller elements where the conservation equations are solved. This means that the solution is only known at selected discrete locations, associated with the discretization grid. The method of choice for this thesis is the finite-volume approach. Finite-volume methods are the most common methods found in commercial solvers often used by industry and have the advantages of being conservative by construction. They are also very flexible regarding the type of mesh elements that can be used [13].

1.2.1 High-Order Methods

In numerical analysis, the order of accuracy of a method is defined by studying how the truncation error of the method is reduced as a function of the refinement of the discretization variable (in our case, time and space are the discretized variables). A given method is said to be of order K if the solution error, e, is proportional to the size of the discretization unit, h, to the power K, $e \propto h^k$. Mathematically, it can be argued that a method of second order or higher is a high-order method. In practice, it is usually considered to be of high-order a method with an order of accuracy of at least three or greater ($K \geq 3$) [14], measured where the solution is

smooth[1]. The higher the order, the lower the truncation error is for the same discretization of a smooth problem. On the other hand, high-order formulations are generally more expensive on a per element or per cell basis; therefore, a global cost/accuracy assessment has to be performed to understand the overall benefits of such approaches. High-order methods would seem particularly desirable for simulating unsteady flows with complicated solution structures. Examples of these are vortex dominated flows, like helicopter blades simulation, turbomachinery flows, or in swirling flows commonly present in combustion systems, where excessive non-physical (numerical) dissipation of the vortices may be an important source of errors. According to Jameson [15], second-order methods for computational simulations of fluid flow are the most widely used schemes in commercial software, but he suggests there is a need for higher-order methods for more accurate simulations of turbulent and vortex dominated flows.

The mechanics of the calculations and the requirements to develop a high-order finite-volume scheme will be detailed in Chapter 3, but it is convenient to mention here some key concepts that will help justify the objectives of this work. In a finite-volume scheme, like the one adopted in the present work, the conservation equations are written in integral form and a solution is sought for the average value of the solution variables within a cell. In order to be able to evaluate the face fluxes, a *reconstruction* of the solution is performed within the cell and this step requires information from the neighbouring cells defining the *stencil* of the scheme. When performing high-order reconstructions, if the solution is discontinuous or under-resolved in a region, the necessity arises to deal with the appearance of spurious oscillations. A substantial amount of the research efforts in high-order finite-volume has been aimed at treating or avoiding the spurious oscillations problems. The development of high-order finite-volume methods has been an intense area of research since the introduction of the Essentially Non-Oscillatory (ENO) schemes of Harten *et al.* [16]. The ENO schemes perform reconstruction on multiple stencils and then select the "smoothest" of the stencils, aiming at controlling the oscillatory behaviour (enforce monotonicity)[17]. Weighted ENO (WENO) schemes have also been developed, combining the different stencils in a weighted fashion [18, 19, 20]. However, these schemes can be computationally expensive and quite complex, particularly for multi-dimensions and unstructured meshes.

The K-exact reconstruction procedure of Barth [21] and Barth and Fredrickson [22] is more easily extendable to multiple dimensions and is the basis of the Central Essentially Non-Oscillatory (CENO) scheme of Ivan and Groth [23] adopted here. Like the related ENO schemes, the CENO scheme is a shock-capturing Godunov-type finite-volume scheme. However, it relies on a hybrid

[1]Special treatment is required wherever the solution is not smooth, and the particular way this is treated in this thesis will be discussed in more details in Section 3.4.5.

reconstruction strategy, where, based on a smoothness indicator switch, it uses either an unlimited high-order K-exact reconstruction [22] on regions classified as smooth by this indicator or a limited piecewise linear reconstruction, if the cell is deemed non-smooth by the indicator. The CENO scheme uses a fixed central stencil for all variables and provides a practical compromise between accuracy, computational efficiency and robustness [24]. Its straightforward definition and implementation also makes it very attractive for multi-dimensional and unstructured mesh applications.

As mentioned previously, finite-difference and finite-element methods are alternatives to finite-volume schemes. Finite-difference approaches with high-order spatial discretization have also been developed and studied [25, 26] for several applications, including combustion problems [27, 28]. Discontinuous Galerkin (DG) methods have also advanced significantly in the last years, specially after the works of Cockburn and Shu [29], Cockburn *et al.* [30], Bassi and S.Rebay [31] with higher-order formulations being introduced by Yan and Shu [32]. According to Gassner *et al.* [33], in spite of significant advances, discontinuous Galerkin methods are still expensive when compared to more traditional methods such as finite-volume methods, that being specially true for viscous problems. An interesting direct comparison between a WENO finite-differences, WENO finite-volume and discontinuous Galerkin (DG) methods is given in Shu [26], where practical aspects in the implementation of the algorithms, applicability and relative advantages are discussed. Finite-differences and discontinuous Galerkin methods may in general benefit largely from specialized implementations, for particular types of meshes. One of the main benefits of a finite-volume formulation is the inherently conservative nature of the scheme allied to a straightforward capability to be extended to unstructured meshes. The main engine of a structured or unstructured finite-volume scheme is the same. The only change required when moving to unstructured meshes is the bookkeeping of the neighbour cells forming the stencil. This inherent robustness and flexibility of finite-volume schemes have made it the method of choice for this study. It is felt that it is more straightforward to develop a general purpose finite-volume scheme for reactive flows, with the complexity of the associated modelling, capable of handling any type of element, including even hybrid meshes with combined types of elements.

1.2.2 Turbulence Modelling

The majority of the combustion systems of practical interest operate in turbulent flow regimes. Turbulent flows are characterized by strong irregular variations in the value of the flow variables, with increased transport of momentum, energy and mass due to the turbulence effects. One option is to model the flow in a direct fashion (Direct Numerical Simulation – DNS) [34], with the

goal of resolving all the features appearing in the flow. This approach is not practical for most flows of interest because of the computational cost associated to it. Another option is to *model the turbulence*. A more complete discussion on turbulence is provided in Chapter 2, but two of the main ideas related to turbulence modelling are worthy mentioning here which are the time averaging of the solution and the spatial filtering of the solution. The Favre/Reynolds Averaging of the Navier-Stokes (FANS/RANS) equations (so-called time averaging of the equations)[35] can and has been used to simulate combustion problems with relative success. It is, however, recognized that the spatial filtering procedure adopted by large eddy simulation (LES) [36] methods is particularly interesting for combustion flows. In LES, a spatial filtering procedure is applied to the conservation equations, which distinguishes components of the solution that are fully resolved by the available mesh from the components that will require modelling. Large eddy simulation has been applied to combustion with increased frequency in the last 10-15 years, even though all the modelling issues in LES have not yet been completely closed [37]. A well designed LES mesh can fully resolve large-scale phenomenon associated with the flow geometry and boundary conditions, and the information collected at these known scales allow for a better understanding of the subgrid contribution to the turbulence, which tends to be more universal and less dependent on the problem.

It is recognized that the application of LES to turbulent reactive flows provides a number of important advantages compared to RANS [38]. Among these are the fact that LES can directly capture the large scale information in the velocity and scalar fields and the fact that the primary target in LES closure is the subfilter scales, which generally have more universal statistics and therefore are less dependent on the particular flow geometry being considered. Pierce and Moin [39] argue that the inaccurate modelling of the large scales may lead Reynolds-averaged approaches to fail to predict turbulent reacting flows accurately, so that even with a fairly simple model for the chemistry, LES may be able to outperform Reynolds-averaged computations that employ more sophisticated chemistry models, encouraging the option for LES made in this study.

1.2.3 Numerical Combustion Modelling

Spatial restrictions usually due to limited weight or cost requirements are often imposed on the design of gas-turbine combustion devices for aviation applications. These devices, therefore, require rapid mixing and short combustion times and at the same time must ensure a controllable, stable flame. These requirements are challenging to be achieved simultaneously. The simulation of practical, real-geometry combustors, including complete or multiple step chemical reaction mechanisms, is still a very computationally demanding task. Such problems involve complex geometries, complex flows and a more complete, detailed chemistry. Bilger [10] explains that,

additional difficulties related to combustor modelling are due to the fact that it is a multi-scale problem that requires careful and detailed modelling of turbulence, recirculations and swirling flows and at the same time requires modelling of the chemical kinetics involved in the oxidation of the fuels and consequently the formation of the products and possible emissions. These are highly non-linear effects, that are strongly coupled together, particularly turbulence and chemistry. The gains that numerical modelling applied to fields like external aerodynamics, structural design and internal non-reactive flows simulation have demonstrated in industrial scale are certainly extendable to combustion modelling if cost effective, accurate methods are available. Also, the need for complex chemistry simulation rather than simplified mechanisms arises, specially if the role of minor species, such as pollutants, are to be studied. According to Cant [40], approaches based on the flamelet assumption, like the Flamelet Generated Manifolds (FGM) [41] or the Flamelet Prolongation of Intrinsically Low-Dimension Manifold (FPI) [42] offer a good compromise between level of chemical detail and computational cost (i.e., a reasonable level of detail at relatively low cost).

In this work, we are particularly interested in studying the application of a novel high-order finite-volume method to reactive flows and to assess the associated computational benefits. Several notable efforts have been identified in the literature considering the application of high-order methods to combustion problems. A finite-difference code for DNS and LES of turbulent non-premixed jet flames has been developed by van der Hoeven *et al.* [27], based on a high-order compact finite-difference formulation. The subgrid scale (SGS) fluxes were closed with a constant Smagorinsky model and a steady-state flamelet model was used for the turbulence-chemistry interaction. Another example of high-order LES using a finite-differences approach to simulate methane combustion is the work of Yaldizli *et al.* [43], where the filtered mass density function methodology was employed as a Subgrid Scale (SGS) closure for the LES model.

In the work of Albouze *et al.* [44], a full compressible Navier Stokes solver with third-order spatial and temporal accuracy was used to model the premixed CH_4 combustion on a swirled combustor. Two different mechanisms are used in this work: a two-step reduced kinetics and a complex chemistry mechanism. The complex chemistry was modelled using the Presumed Conditional Moment - Flame Prolongation of Intrinsic Low Dimensional Manifold (PCM-FPI) approach. Albouze *et al.* [44] found that PCM and thickened flame models yielded very close results and further studies were proposed using PCM-FPI. Using complex chemistry with PCM-FPI also allowed for better prediction of minor components, as CO mass fractions for example.

Mesh effects on LES in a full annular gas-turbine combustion chamber (including its casing) were also studied by Poinsot [45]. A tetrahedral mesh was used with elevated number of elements in the order of 10^8, 10^9. A fully compressible, multi-species reacting LES model was used in a

third-order of accuracy finite-element solver. A surrogate for the JP-1 fuel was used in a one step chemical reaction simulation. Franzelli *et al.* [46] used a third order finite-element solver to study combustion instabilities on a swirled combustor at different equivalence ratios. They adopted a 2-step reduced chemistry mechanism for methane combined with a dynamically thickened flame model. Vervisch *et al.* [28] considered DNS with a sixth-order finite-difference spatial scheme and also performed LES using a skew-symmetric, fourth-order finite-volume scheme. Additionally, the work of Desjardins *et al.* [47] presents a high-order finite-difference framework capable of simulating variable density, multispecies, turbulent flows in realistic geometries aiming towards reactive flow applications.

In the work of Gerlinger [48], a high-order finite-volume scheme was used with an Unsteady Reynolds Averaged Navier-Stokes (URANS) formulation, combined with finite-rate chemistry for H_2 (using 19 reactions and 11 species) and Sheikhi *et al.* [49] performed the LES of non-premixed flames with transported probability density functions, with a fourth-order compact finite-difference spatial scheme discretization of the compressible flow equation. In a recent presentation by Lv and Ihme [50], current efforts with high-order Discontinuous Galerkin methods were shown, applied to combustion problems, recognizing the benefits of high-order approaches to such problems. Additionally, moving towards a potential application in reactive flows, the recent work of Owen *et al.* [51] presents a finite-volume high-order adaptive algorithm for multispecies gaseous flows on mapped Cartesian meshes.

These recent efforts with high-order described in the previous paragraphs have shown a focus either on high-order finite-difference approaches or on an intermediate third-order finite-volume methods, and often with simplified chemistry. While high-order methods are routinely used for DNS on simpler structured grids, practical LES methods are still generally second-order accurate. It is our understanding that, despite the notable efforts listed above, it can be said that the application of a high-order, finite-volume scheme and LES coupled with complex chemistry has received relatively little attention. Moreover, the CENO scheme of interest here has not yet been applied in conjunction with a tabulated chemistry formulation.

1.3 Thesis Objectives

The Computational Combustion and Propulsion research group at the University of Toronto Institute for Aerospace Studies, to which the author is affiliated, has conducted a systematic research effort aimed at improving the accuracy and efficiency of numerical methods for a range of fluid flow problems. Among these we mention the efficient time-marching schemes developed by Groth and Northrup [52], Northrup and Groth [53, 54, 55] and Northrup [56], the paral-

lelization and adaptive mesh refinement (AMR) methods of Gao and Groth [57, 58, 59], Gao [60], the two-dimensional (2D) high-order CENO scheme of Ivan and Groth [23, 61, 62] and its three-dimensional structured extension by Ivan *et al.* [2]. The CENO scheme was also studied recently in a unstructured implementation by Charest *et al.* [63]. Complex chemistry using PCM-FPI has been considered for second-order LES by Hernández-Pérez *et al.* [64], Hernández-Pérez *et al.* [65, 66], Salehi *et al.* [67], Shahbazian *et al.* [68], Hernàndez-Pérez [69], and for RANS by Jha and Groth [70] and Jha [71]. This thesis combines some aspects of the previous research efforts at the Computational Combustion and Propulsion Group with the goal of developing a scheme capable of dealing with the challenges related to combustion flow simulations: complex geometry, complex turbulence and complex or detailed chemistry.

From the material presented in Section 1.1, the motivation to study combustion becomes clear. Numerical modelling has been shown to be an important tool for studying combustion systems and particularly the use of a high-order finite-volume formulation will be investigated here by extending the CENO scheme to three-dimensional reactive flows. In order to deal with complex geometries a structured mesh based on generic hexahedral elements, allowing non-planar faces is considered. To be able to simulate complex turbulent features, a LES approach is selected, combined with the PCM-FPI chemistry model, allowing to introduce elements of complex chemistry into the simulation. The object of study here is a laboratory turbulent premixed flame. These premixed flames present relatively simple flow while retaining many aspects of complex physics and beyond their own importance to some applications, such as in stationary energy generation turbines, the numerical developments made to model premixed flames can potentially be extended to other types of flames as well. In conclusion, this thesis will consider the development of a new three-dimensional high-order finite-volume scheme using the PCM-FPI turbulence-chemistry interaction strategy and its application to the LES of a laboratory-scale premixed flame.

1.3.1 Organization of Thesis

Following this introductory chapter, where the motivation and the objectives of this work have been presented, the remaining of the document is divided in four other chapters. In Chapter 2, background information about the mathematical modelling of the physical problem is provided, namely, the governing equations and modelling of turbulent premixed flames. A brief theoretical basis is provided presenting the Navier-Stokes equations, describing some basic concepts in turbulence and combustion and some of the existing alternatives for the modelling of these phenomenon. The chapter ends with a presentation of the specific turbulence-chemistry interaction model selected for this work (the PCM-FPI model) and is finally closed with the

set of partial differential equations that will require numerical solution. The presentation of the set of equations provides a connection and lead into Chapter 3, where the numerical method used to solve the conservation equations is presented, emphasizing the description of a general finite-volume schemes, the treatment of the generic hexahedral mesh elements using a trilinear mapping and a detailed description of the high-order framework, the CENO scheme, that will be applied to the set of conservation equations of interest. Some preliminary numerical tests performed to check the implementation of the high-order method are also presented, closing Chapter 3.

In Chapter 4, the results of the application of the CENO scheme to simulate a laboratory turbulent flame are presented. In this chapter the numerical studies with different meshes and orders of accuracy of the scheme are shown. Second-, third- and fourth-order spatial discretizations are considered and some parametric studies are performed varying the numerical setup of the high-order formulation. Finally, in Chapter 5, the conclusions and closing comments are presented and suggestions for future follow-up works are also given.

Chapter 2

Mathematical and Physical Modelling

In the introductory chapter, the motivations for studying combustion were discussed. In particular the attractiveness of having the support of numerical methods to simulate reactive flows was highlighted. In this chapter, the choices that were made in this work for the physical and mathematical modelling of a turbulent premixed flame will be discussed. Starting from first principles, the conservation equations used in reactive flow modelling are presented. Some background information is given related to turbulence modelling, with particular attention given to the current LES subgrid modelling. The spatially filtered equations are first presented and the modelling options made for the unclosed terms are explained, with a brief description of various alternatives available for the turbulent reaction rate closure. This leads to the final portion of the chapter where the PCM-FPI combustion model is explained. Finally, a summary of the set of governing equations used to perform the LES of premixed turbulent reactive flows is given.

2.1 The Conservation Equations

For most practical applications of reactive flows in engineering, the Navier-Stokes equations are the mathematical model of choice to represent the physical principle of conservation of momentum. Additionally, one continuity equation (based on the physical principal of mass conservation) and one energy conservation equation (based on the first law of thermodynamics) are also required for compressible flow treatments. To provide a relation between the thermodynamic variables of the flow, an equation of state must be introduced. For the reacting mixtures flow of interest in this work, a set of species mass fractions conservation equations must also be considered, representing the consumption/formation of each individual species and how the mixture composition evolves and varies throughout the domain of interest. Depending on the

problem and the modelling for the problem of interest, additional scalar transport equations may be used. For the particular case considered here, choices for the scalar field related to the turbulence and chemistry modelling used here will be discussed in Sections 2.3 and 2.5.

The conservation equations for mass, momentum, energy, and species mass fractions governing the flow of thermally perfect, reactive, multi-species mixtures can be summarized, using tensor notation, as

$$\frac{\partial \rho}{\partial t} + \frac{\partial (\rho u_j)}{\partial x_j} = 0\,, \tag{2.1}$$

$$\frac{\partial (\rho u_i)}{\partial t} + \frac{\partial (\rho u_i u_j + \delta_{ij} p)}{\partial x_j} - \frac{\partial \tau_{ij}}{\partial x_j} = \rho g_i\,, \tag{2.2}$$

$$\frac{\partial (\rho E)}{\partial t} + \frac{\partial [(\rho E + p) u_j]}{\partial x_j} - \frac{\partial (\tau_{ij} u_i)}{\partial x_j} + \frac{\partial q_j}{\partial x_j} = \rho g_i u_i\,, \tag{2.3}$$

$$\frac{\partial (\rho Y_\alpha)}{\partial t} + \frac{\partial (\rho Y_\alpha u_j)}{\partial x_j} + \frac{\partial \mathcal{J}_{j,\alpha}}{\partial x_j} = \dot{\omega}_\alpha\,. \tag{2.4}$$

The above equations also presented by Poinsot and Veynante [72], represent the evolution in time, t, and space, $\mathbf{x}$, of a thermally perfect reactive mixture of N chemical species. In these equations, expressions for the species molecular fluxes and viscous fluxes are required and take the following form:

$$\tau_{ij} = \mu \left(\frac{\partial u_i}{\partial x_j} + \frac{\partial u_j}{\partial x_i} \right) - \frac{2}{3} \mu \delta_{ij} \frac{\partial u_l}{\partial x_l}\,, \tag{2.5}$$

$$q_j = -\lambda \frac{\partial T}{\partial x_j} - \rho \sum_{\alpha=1}^{N} h_\alpha \mathcal{D}_\alpha \frac{\partial Y_\alpha}{\partial x_j}\,, \tag{2.6}$$

$$\mathcal{J}_{j,\alpha} = -\rho \mathcal{D}_\alpha \frac{\partial Y_\alpha}{\partial x_j}\,. \tag{2.7}$$

In the present work, a Newtonian fluid with negligible bulk viscosity is assumed, and the viscous stress tensor takes the form given in Equation (2.5). More complex expressions may be used to describe multi-species molecular diffusion [73], but here the Fick's law of diffusion, Equation (2.7), is assumed. The heat flux is given by Equation (2.6), where the Soret effect (species diffusion under temperature gradients) as well as the Dufour effect (enthalpy diffusion under mass fraction gradients) are neglected [73]. Radiation effects are also deemed negligible for the reactive flow cases considered in the present work.

In Equations (2.1)-(2.4), the tensor indices in three-dimensions are $i, j, l = 1, 2, 3$ and the species mass fractions are labelled $\alpha = 1, \ldots, N$. The summation convention for repeated indices applies to i, j, and l. It is useful to summarize here the variables found in these expressions. The density

of the mixture is ρ, u_i is the i^{th} component of the velocity vector of the mixture, p is the mixture pressure, T is the mixture temperature, E is the total energy of the mixture including heat of formation, Y_α is the mass fraction of species α, $\dot{\omega}_\alpha$ is the net reaction rate of species α, g_i is the acceleration due to gravity, τ_{ij} is the viscous stress tensor, q_j is the total heat flux (energy flux due to thermal conduction and energy flux due to the diffusion of species), and $\mathcal{J}_{j,\alpha}$ is the mass diffusive flux of species α. The coefficients μ, λ, h_α, and $\mathcal{D}_\alpha$ are the mixture viscosity, mixture thermal conductivity, enthalpy of species α, and molecular diffusivity of species α, respectively. Additionally, δ_{ij} is the Kronecker delta. The mixture is assumed to obey the ideal gas equation of state, which has the form

$$p = \rho\mathcal{R}T/\mathcal{M} = \rho RT\,, \tag{2.8}$$

where $\mathcal{R}$ is the universal gas constant ($8.314\ \mathrm{J\cdot mol^{-1}\cdot K^{-1}}$) and R is the mixture gas constant given by $R = \mathcal{R}\sum_{\alpha=1}^{N} Y_\alpha/\mathcal{M}_\alpha = \sum_{\alpha=1}^{N} Y_\alpha R_\alpha$. Some important definitions for the case of reactive flows of gaseous mixtures, are the mass fraction and molar fraction. For a given species α, the mass fractions, Y_α, and the mole fractions, X_α, are defined as

$$Y_\alpha = \frac{m_\alpha}{\sum_{\beta=1}^{N} m_\beta}\,, \tag{2.9}$$

$$X_\alpha = \frac{n_\alpha}{\sum_{\beta=1}^{N} n_\beta}\,, \tag{2.10}$$

where m_α is the mass of species α and n_α is the mole number of species α. It is important to notice that $\sum_{\alpha=1}^{N} Y_\alpha = 1$ and $\sum_{\alpha=1}^{N} X_\alpha = 1$.

The total energy of the mixture is given by the expression

$$E = e + \frac{1}{2}u_i u_i = h - \frac{p}{\rho} + \frac{1}{2}u_i u_i\,, \tag{2.11}$$

where e is the mixture absolute internal energy and h is the mixture absolute enthalpy. Energy and enthalpy are related by $e = h - p/\rho$. The mixture absolute internal energy and enthalpy can be determined as functions of the individual species absolute internal energy, e_α, and absolute enthalpy, h_α, using the following expressions for a perfect mixture.

$$e = \sum_{\alpha=1}^{N} Y_\alpha e_\alpha\,, \tag{2.12}$$

$$h = \sum_{\alpha=1}^{N} Y_\alpha h_\alpha\,. \tag{2.13}$$

For each species, e_α and h_α are taken to be functions of temperature only. For a given temper-

ature T^*, species, energy and enthalpy are assumed to have the form

$$e_\alpha = \int_0^{T^*} C_{\mathrm{v}_\alpha}(T)\,\mathrm{d}T\,, \tag{2.14}$$

$$h_\alpha = \int_0^{T^*} C_{\mathrm{p}_\alpha}(T)\,\mathrm{d}T\,, \tag{2.15}$$

where C_{p_α} and C_{v_α} are the species heat capacities at constant pressure and volume, respectively. These expressions for species, α, are re-written as [72]

$$e_\alpha = \int_{T_0}^{T^*} C_{\mathrm{v}_\alpha}(T)\,\mathrm{d}T - R_\alpha T_0 + \Delta h^0_{\mathrm{f}_\alpha} = e_{\mathrm{s}_\alpha} + \Delta h^0_{\mathrm{f}_\alpha}\,, \tag{2.16}$$

$$h_\alpha = \int_{T_0}^{T^*} C_{\mathrm{p}_\alpha}(T)\,\mathrm{d}T + \Delta h^0_{\mathrm{f}_\alpha} = h_{\mathrm{s}_\alpha} + \Delta h^0_{\mathrm{f}_\alpha}\,, \tag{2.17}$$

where e_{s_α} is the species sensible internal energy, h_{s_α} is the species sensible enthalpy, and $\Delta h^0_{\mathrm{f}_\alpha}$ is the species heat of formation (chemical energy) at a reference temperature T_0 (usually 298 K).

In the case of combustion, the concept of equivalence ratio, ϕ, can be defined to characterize the fuel-oxidizer mixture. The equivalence ratio is a quantitative measure defining whether or not a fuel-oxidizer mixture is stoichiometric, rich (higher fuel-oxidizer ratio than stoichiometric) or lean (lower fuel-oxidizer ratio than stoichiometric) [74]. This parameter is defined as

$$\phi = \frac{(F/O)}{(F/O)_{\mathrm{st}}}\,, \tag{2.18}$$

where the fuel-oxidizer ratio is the ratio between the mass of fuel and mass of oxidizer, $(F/O) = m_{\mathrm{F}}/m_{\mathrm{O}}$, in the premixed mixture. A stoichiometric fuel-oxidizer mixture (ϕ=1) results in the complete oxidation of the fuel and the combustion products are in their most stable form.

2.1.1 Thermodynamic Properties

The thermodynamic properties of the mixtures are calculated based on the individual thermodynamic properties for each species. In the present work, the species properties enthalpy, thermal conductivity, molecular viscosity, constant-pressure heat capacity, molecular mass, heat of formation and entropy are stored in databases as a function of temperature as developed by Gordon and McBride [75] and McBride and Gordon [76]. For example, for enthalpy and heat

capacity at constant-pressure, the following polynomials are used:

$$\begin{aligned} h_\alpha &= R_\alpha T \left[-a_{1,\alpha} T^{-2} + a_{2,\alpha} T^{-1} \ln T + a_{3,\alpha} + \frac{a_{4,\alpha} T}{2} + \frac{a_{5,\alpha} T^2}{3} \right. \\ &\quad \left. + \frac{a_{6,\alpha} T^3}{4} + \frac{a_{7,\alpha} T^4}{5} + b_1 T^{-1} \right] + \Delta h^0_{\mathrm{f}_\alpha} , \qquad (2.19) \\ C_{\mathrm{p}_\alpha} &= R_\alpha \left[a_{1,\alpha} T^{-2} + a_{2,\alpha} T^{-1} + a_{3,\alpha} + a_{4,\alpha} T + a_{5,\alpha} T^2 + a_{6,\alpha} T^3 + a_{7,\alpha} T^4 \right] , \qquad (2.20) \end{aligned}$$

where $a_{m,\alpha}$ and $b_{m,\alpha}$ are the coefficients to be fit for each species α, and $\Delta h^0_{\mathrm{f}_\alpha}$ is the heat of formation of species α. Similar expressions are used for both the species thermal conductivity, λ_α, and molecular viscosity, μ_α, and can be written as (with Υ representing either μ or λ)

$$\Upsilon_\alpha = \exp\left(A_{\Upsilon,\alpha} \ln T + B_{\Upsilon,\alpha} T^{-1} + C_{\Upsilon,\alpha} T^{-2} + D_{\Upsilon,\alpha} \right) , \qquad (2.21)$$

where $A_{\Upsilon,\alpha}$, $B_{\Upsilon,\alpha}$, $C_{\Upsilon,\alpha}$, and $D_{\Upsilon,\alpha}$ are the corresponding empirical coefficients for μ or λ.

In order to calculate the mixture properties, the mixture rule of Wilke [77] is used for the mixture viscosity and the Mason and Saxena's mixture rule [78] is used for the thermal conductivity, both of which can be summarized by

$$\mu = \sum_{\alpha=1}^{N} \frac{\mu_\alpha Y_\alpha}{\mathcal{M}_\alpha \varphi_\alpha} , \qquad (2.22)$$

$$\lambda = \sum_{\alpha=1}^{N} \frac{\lambda_\alpha Y_\alpha}{Y_\alpha + 1.065 \mathcal{M}_\alpha (\varphi_\alpha - 1)} , \qquad (2.23)$$

where φ_α is a function of $\mathcal{M}_\beta / \mathcal{M}_\alpha$ and μ_α / μ_β.

The relations between species, momentum and heat diffusivities is represented by the non-dimensional Lewis number for species α (heat and mass diffusivity relation), the mixture Prandtl number (heat and momentum diffusivity relation), and Schmidt number for species α (momentum and species diffusivity relation). They are respectively defined by the following relations:

$$\begin{aligned} Le_\alpha &= \frac{\lambda}{\rho \mathcal{D}_\alpha C_{\mathrm{p}}} , \qquad (2.24) \\ Pr &= \frac{\mu C_{\mathrm{p}}}{\lambda} , \qquad (2.25) \\ Sc_\alpha &= \frac{\mu}{\rho \mathcal{D}_\alpha} . \qquad (2.26) \end{aligned}$$

The mixture heat capacity C_{p} is given by the mass fraction weighted average of the species heat capacity. For the combustion problems studied here, the mixture Prandtl number is of the order

unity (≈ 0.7 for many gases) and the Lewis and Schmidt numbers in many cases are also of order unity [79, 74], except for lighter gases such as hydrogen.

2.1.2 Law of Mass Action - Finite Rate Chemical Kinetics

The direct approach to the solution of reactive systems is the evaluation of the species source terms provided direct by the the chemical kinetics. Considering a chemical system composed of N species reacting according to a particular mechanism composed of N_{R} reactions, the N_{R} forward and backward reactions can be summarized as

$$\sum_{\alpha=1}^{N} \nu'_{\alpha,r} \mathrm{M}_\alpha \rightleftharpoons \sum_{\alpha=1}^{N} \nu''_{\alpha,r} \mathrm{M}_\alpha \,. \qquad r = 1, 2, \ldots, N_{\mathrm{R}} \,. \tag{2.27}$$

In Equation (2.27) above for each species α and for each reaction r, the symbols $\nu'_{\alpha,r}$ (products) and $\nu''_{\alpha,r}$ (reactants) indicate the molar stoichiometric coefficients. Generically representing any species, the symbol M is used above as the chemical symbol of species α. From the preceding chemical kinetics, it is possible to use the law of mass action to evaluate the time rate of change of the species α concentration, $\dot{\omega}_\alpha$, which can be written as

$$\dot{\omega}_\alpha = \frac{d\left[\frac{\rho Y_\alpha}{\mathcal{M}_\alpha}\right]}{dt} = \frac{\mathcal{M}_\alpha}{\rho} \sum_{r=1}^{N_{\mathrm{R}}} \left(\nu''_{\alpha,r} - \nu'_{\alpha,r}\right) \left\{ k_r^{\mathrm{f}} \prod_{\beta=1}^{N} \left[\frac{\rho Y_\beta}{\mathcal{M}_\beta}\right]^{\nu'_{\beta,r}} - k_r^{\mathrm{b}} \prod_{\beta=1}^{N} \left[\frac{\rho Y_\beta}{\mathcal{M}_\beta}\right]^{\nu''_{\beta,r}} \right\} . \tag{2.28}$$

A very important step in the evaluation of the equation above is the calculation of the forward and backward reaction rates for reaction r, k_r^{f} and k_r^{b}. The usual assumption is that the reaction rate constants are temperature dependent and can then be determined using the Arrhenius law and written

$$k_r = A_r T^{B_r} \exp\left(\frac{E_{\mathrm{a}_r}}{\mathcal{R}T}\right) . \tag{2.29}$$

The values for the pre-exponential factor, A_r, the temperature exponent, B_r and the activation energy E_{a_r} are usually generated experimentally and tabulated.

As will be discussed later in this chapter, in Section 2.4, the preceding direct approach for the chemical kinetics is of very little and restricted practical use in the case of turbulent flames. Specific modelling strategies and how to deal with the modelling of the chemical source terms when there is a strong interaction with turbulence will be discussed towards the end of the chapter. Before that, some basic theoretical concepts in combustion and turbulence are introduced.

2.2 Brief Review of Turbulent Combustion Modelling

In this section, some important concepts used in the theoretical modelling of turbulent premixed flames are discussed. It will be seen that, in order to be able to describe what happens in a turbulent flame, it is common to rely on the so-called flamelet assumption [1]. The flamelet approach is based on the description of a turbulent flame as a collection of laminar flame elements embedded in a turbulent flow and interacting with it. The local structure of the flame at each point in the flame front is taken to be similar to a laminar flamelet, while the flame interaction with the turbulence is treated by taking the flame to be an evolving front that is distorted and wrinkled by the turbulence. In this sense, some important concepts in modelling laminar flames are presented, followed by a discussion of turbulence and some of the key parameters used in its definition. This is followed by definitions of important non-dimensional numbers relevant to turbulent premixed combustion. A short discussion on the different regimes in which premixed combustion systems may operate is also presented.

2.2.1 One-Dimensional Laminar Premixed Flame

A premixed flame, as described by Turns [74], is the self-sustaining propagation of a localized combustion zone. The flame, by definition, occupies only a small portion of the combustible mixture at any one time. A subsonic combustion wave is called a deflagration wave, and a supersonic combustion wave is called detonation. The present study is limited to deflagration waves.

The one-dimensional (1D) laminar premixed flame is the simplest premixed flame model available and many of the concepts devised for the study of this type of flame are extended or extrapolated to help understand the behaviour of turbulent flames. As will be seen in more detail in Section 2.4, different models have been proposed for LES of premixed turbulent combustion, where the validity of a laminar flamelet concept is usually assumed for these models [36]. A typical one-dimensional laminar premixed flame has a structure that can be divided into three main regions: 1) the preheat layer, which is the thickest region, where mostly convection and diffusion occur, with very limited heat release; 2) the inner layer, where most of the fuel is consumed and most of the heat release occurs (this layer is approximately 0.1 mm thick for stoichiometric methane flames [73]); and 3) the oxidation layer that contains mostly the burned gases (products). A schematic representation of a laminar premixed flame is given in Figure 2.1, showing the distribution of mass fractions evolution with respect to x, through a one-dimensional (1D) methane flame at stoichiometric equivalence ratio. It can be seen that a sharp variation in the composition of the mixture takes place in a very thin region (the inner

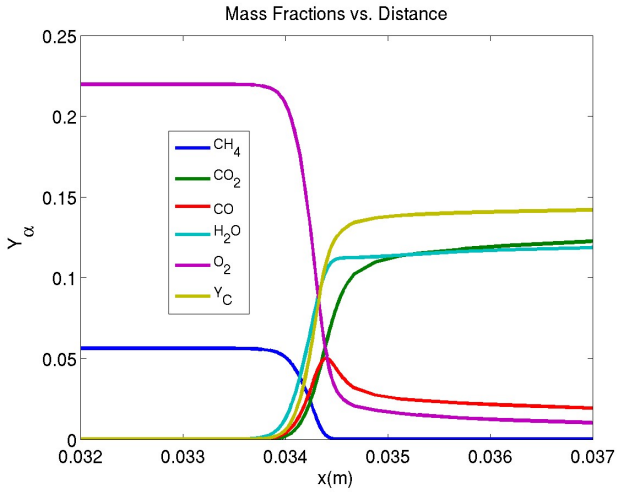

Figure 2.1: Mass fractions as function of distance in premixed 1D laminar flame (CH_4, ϕ=1.0)

layer).

One very important concept in the study of 1D laminar flames is the laminar flame speed or laminar burning velocity, S_L. With a reference frame fixed to the flame front, a stationary flame with respect to the laboratory would see the unburnt reactants approaching at the laminar flame speed.

2.2.2 Turbulent Flow Theory

Most flows of practical interest are turbulent flows. Despite its ubiquitous nature, a unique, exact definition of what constitutes a turbulent flow is not readily available. Instead of trying to define what is turbulence it is more useful to try to recognize what are the common elements present in all turbulent flows [80] and how to extract useful information from these features. Turbulent flows are characterized by the irregularity or randomness of the motions, with a wide range of scales, but even the smallest length scales involved in turbulent flows are far larger than molecular length scales, so turbulent flows are continuum flows. Another important element in turbulence is high diffusivity, since these random motions promote rapid heat, momentum and mass transfers. The rapid motions also make turbulent flows dissipative, so that the kinetic energy of these motions is gradually dissipated by viscous effects. Therefore, turbulence requires a continuous supply of forcing energy in order to be sustained. Turbulent flows are characterized by large Reynolds numbers, where the non-linear inertia terms in the equations of motion become larger than the viscous terms. Turbulence is also intrinsically three-dimensional, being characterized by a high-level of fluctuating vorticity. The description of turbulent flows conveniently makes use of the concept of eddies, which are turbulent motions, in different sizes and

relatively coherent within certain regions [81].

A quantitative description of turbulent flows usually relies on the idea of fluctuating quantities, so that a flow variable ψ can be described as a mean value, $\langle\psi\rangle$, superposed by combining a fluctuating component, ψ'. These fluctuations can be defined based on time averages or spatial averages, and the instantaneous quantity for a turbulent flow, ψ, can be expressed as

$$\psi = \langle\psi\rangle + \psi' \,, \tag{2.30}$$

The decomposition of a velocity component, u_i, using the above definition yields the component u_i', the fluctuating velocity component. The variable u', often referred to as turbulent intensity can also be defined. This variable then appears in the definition the turbulent kinetic energy, k, as

$$k = \frac{\langle u_i' u_i' \rangle}{2} \,. \tag{2.31}$$

The concept of integral length scale, L_t, is also of great importance and is a measure of the size of the biggest eddies appearing in the flow. A useful definition for the turbulent Reynolds number can be defined using the turbulent intensity, u', and the integral length scale, L_t, as

$$Re_\mathrm{t} = \frac{u' L_\mathrm{t}}{\nu} \,. \tag{2.32}$$

Kolmogorov [82] originally developed the concept of a turbulent kinetic energy cascade. The turbulent kinetic energy occurring in large scale eddies is continuously transferred to smaller eddies until it is dissipated by viscous forces. The properties of the smallest scales are, according to his theory, governed by the rate of energy dissipation of kinetic energy, ϵ, and by the kinematic viscosity of the fluid, ν. By performing dimensional analysis, the Kolmogorov length, velocity and time scales can be respectively defined as

$$\eta = \left(\frac{\nu^3}{\epsilon}\right)^{1/4} \,, \qquad u_\mathrm{K}' = (\nu\epsilon)^{1/4} \,, \qquad \tau_\mathrm{K} = \left(\frac{\nu}{\epsilon}\right)^{1/2} \,. \tag{2.33}$$

With this definition of η, we arrive at the relation between the Kolmogorov and integral length scales given by

$$\frac{L_\mathrm{t}}{\eta} \approx Re_\mathrm{t}^{3/4} \,, \tag{2.34}$$

which scales with the Reynolds number and illustrates the possibility for a wide range of turbulent scales with increasing Reynolds number.

2.2.3 Theory of Turbulent Premixed Combustion

The idea of representing a turbulent quantity by an average and a fluctuating component will be of great utility in solving the conservation equations of interest here but this decomposition will introduce some unclosed terms that will require modelling, as detailed in Section 2.3.3. Additionally, the filtered reaction rates can not be found by simple averaging of the generally non-linear Arrhenius reaction rates without strong restrictions, which are generally not applicable for most combusting flows of practical interest [73]. A physical analysis is required to derive models for turbulent combustion and of particular interest is the analysis of the length scales involved in the processes.

Combustion problems are usually classified as premixed, non-premixed or partially-premixed, depending on when the reactants are mixed in relation to when the reaction starts. In premixed combustion, fuels and oxidizers are assumed perfectly mixed at a molecular level before entering the reactor. In non-premixed combustion devices, the fuel and oxidizer are injected separately into the combustion chamber. Before reacting, fuel and oxidizer must first mix inside the reactor. In a third scenario, the reactants may not necessarily be perfectly mixed before undergoing reactions, representing an intermediate regime between premixed and non-premixed combustion named partially premixed combustion. The premixed regime is of interest in this thesis.

The first basic parameter in the analysis of turbulent combustion flows is the turbulent Reynolds number, Re_{t}, as described in Section 2.2.2. The chemical time scale, τ_{c}, is related to how fast reactants are converted into products. For premixed laminar flames, it is defined as the ratio of laminar flame thickness, δ_{L}, to the laminar flame speed, S_{L}, and given by

$$\tau_{\mathrm{c}} \approx \frac{\delta_{\mathrm{L}}}{S_{\mathrm{L}}}. \tag{2.35}$$

One very important non-dimensional number used in analysing the relation between the different scales in premixed turbulent combustion is the Damkhöler number, Da, which representes the ratio of the turbulent integral time scale to the chemical time scale and can be written as

$$Da = \frac{L_{\mathrm{t}}/u'}{\delta_{\mathrm{L}}/S_{\mathrm{L}}}\,. \tag{2.36}$$

From this definition, it can be seen, for example, that for high Damköhler number (turbulent time scale is larger than the chemical time scale) the flame structure will locally exhibit similarities to laminar flame, whereas globally, the flame will be wrinkled due to the turbulence.

Another important non-dimensional number is the Karlovitz number, Ka, which compares the

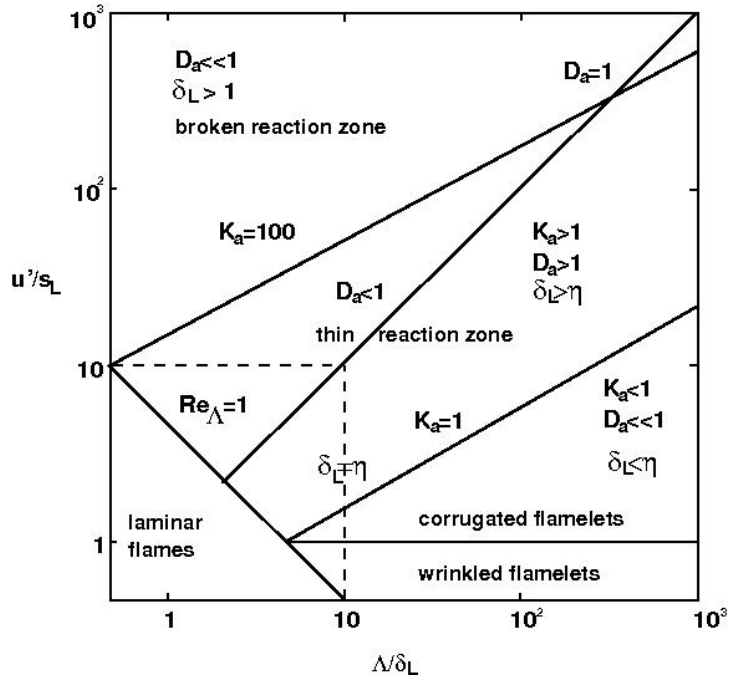

Figure 2.2: Premixed turbulent combustion regime diagram, as appearing in Peters [1]

chemical time scale to the smallest time scales, the Kolmogorov time scale and is given by

$$Ka = \frac{\delta_L/S_L}{\eta/u'_K}\,. \tag{2.37}$$

For very low Karlovitz numbers, the flame is thinner than the smallest scale of turbulence, meaning that the turbulent fluctuations do not penetrate the inner flame structure.

In order to visualize the relation between the different non-dimensional parameters involved in turbulent premixed combustion, it is useful to introduce a premixed combustion regime diagram. The regime diagram is defined by the turbulence and flame ratios of length, Λ/δ_L, and velocity, u'/S_L. Different versions of the regime diagram have been proposed in the literature and one version is shown here, in Figure 2.2, where the regime diagram of Peters [1] is depicted.

By considering the range of possible values for each of the two non-dimensional parameters of interest, different premixed regions can be identified as shown in Figure 2.2. There is a *Laminar flames zone* characterized by $Re_t < 1$. The laminar and turbulent combustion regimes are separated by the $Re_t = 1$ line. As noted previously, this regime is of little interest for the analysis of practical combustion systems, since these systems usually operate in the turbulent regime $Re_t > 1$. One region that can be identified within the turbulent flame zone is the so called *Wrinkled flamelets regime*. This is a particular turbulent regime where $u' < S_L$. Because of the low turbulence levels associated with this regime the effect of large turbulent

eddies on the wrinkling of the flame front is limited. The laminar propagation of the flame dominates. The regime of *Corrugated flamelets* is a turbulent flamelet regime where Ka < 1 and higher turbulence intensity is observed ($u' > S_{\mathrm{L}}$). The flame-front interactions may lead to the formation of isolated pockets of burnt products and fresh gas that can produce topology changes in the flame. Another turbulent region in the diagram is the *Thin reaction zones* regimes where $1 <$ Ka < 100. The thin reaction zones regime is characterized by Kolmogorov scales smaller than the flame-thickness, so that the smallest eddies can now enter the flame and distort the local laminar structure; however the reaction zones generally remain intact. The *Broken reaction zones* regimes is a highly turbulent regime for which Ka > 100, meaning that the turbulent motions are very fast (shorter times than the chemical reaction time) and now the eddies can actually penetrate the inner structure of the flame. While reviews of recent experimental studies of high-turbulent premixed flames have proposed new boundaries to the regime diagram, particularly for the thin reaction zone and extent of the broken reaction zones regimes [83], the preceding description is still relevant.

Progress Variable Concept

For a simple non-reversible reaction, the transition through a laminar flame front can be described by a progress variable, c, which has a value c=0 in the reactants and a value of c=1 in the products, and intermediate values characterize the evolution (progress) of the reaction from reactants to product. In premixed combustion, the particular case of interest here, for flows with low Mach number and Lewis number close to unity, one progress variable is usually sufficient to describe the complete thermochemical state of the system [40]. This progress variable may be defined in different ways [73]. It is usually derived by non-dimensionalizing field variables that can characterize the beginning and the end of the reaction zone such as the temperature, the mass fraction of fuel, or even some other mass fraction whose particular amount at a given time and location can identify the progress of the reaction. This normalization procedure is done in such a way that the progress variable would take intermediate values between 0 and 1, indicating how the reaction progresses from the reactants to the fully burned products. In terms of either the temperature of fuel mass fraction, the progress variable can be written as

$$c = \frac{T - T_{\mathrm{u}}}{T_{\mathrm{b}} - T_{\mathrm{u}}}\,, \tag{2.38}$$

$$c = \frac{Y_{\mathrm{F}} - Y_{\mathrm{F}}^{\mathrm{u}}}{Y_{\mathrm{F}}^{\mathrm{b}} - Y_{\mathrm{F}}^{\mathrm{u}}}\,, \tag{2.39}$$

where T, T_{u}, and T_{b} are respectively the local, the unburned, and burned gas temperatures. Similarly, Y_{F}, $Y_{\mathrm{F}}^{\mathrm{u}}$, and $Y_{\mathrm{F}}^{\mathrm{u}}$ are the local, the unburned, and burned gas fuel mass fractions. By

making use of the fuel transport equation, a transport equation for the progress variable can be derived and written as given by Cant [40] as

$$\frac{\partial(\rho c)}{\partial t} + \frac{\partial(\rho u_i c)}{\partial x_i} = \frac{\partial}{\partial x_i}\left(\rho \mathcal{D}_c \frac{\partial c}{\partial x_i}\right) + \dot{\omega}_c \,. \tag{2.40}$$

2.3 Turbulence Modelling

For large Reynolds number flows, when inertia forces become larger than the viscous forces, the otherwise laminar flow becomes unstable leading to large variations in time and space of the flow properties, like velocity and pressure. These are the characteristics of turbulent flows, which are naturally unsteady and three-dimensional. Complete and recommended readings on the basic principles of turbulent flows are the works of Tennekes and Lumley [80] and Pope [81].

As pointed out by Wilcox [35], an ideal model for turbulence should introduce the minimum amount of complexity while capturing the essence of the relevant physics. A great variety of modelling options exists for turbulent flows, including simple algebraic models, usually more appropriate under very simplified and specific conditions and not so common for reactive flows. Among the most traditional and widely used for combustion flows are the modelling based on RANS/FANS equations, LES and DNS.

2.3.1 Direct Numerical Simulation and Reynolds Averaging Methods

In DNS all the scales of turbulence are resolved directly. No filtering, therefore no special closure for turbulence is required. In this sense, DNS is regarded as the most accurate approach to deal with turbulent flows and no modelling is required. However, due to the need of resolving all the scales, a very fine time and spatial discretizations are required and the resolution needed is an inverse function of the Reynolds number. The larger the Reynolds number, the smaller the time steps and finer the mesh required and therefore, the computational costs for the simulation increase, particularly in reactive flow cases. Due to the resulting large number of degrees of freedom involved in turbulent simulations, specially in turbulent combustion, a full DNS of a practical systems becomes prohibitively expensive [73]. In practice, DNS has been used as a research tool to investigate individual phenomenon in smaller scale problems and therefore support other modelling strategies with these findings. Turbulent flames are analyzed with DNS in simple configurations, allowing the extraction of data that are sometimes impossible to measure in experiments.

The RANS-based methods are the most popular alternative for general turbulence modelling of

industrial, practical devices. The RANS approach relies on the application of a time filter (time averaging), over a period that is much longer than the turbulent correlation times. This means that all of the turbulence is modelled and only the mean flow is resolved. The relative low cost associated with a good ability to reproduce steady time averaged quantities makes this option very popular for many applications. However, RANS-based methods have their limitations as was discussed in the introduction to this thesis.

2.3.2 Large Eddy Simulation (LES)

As mentioned in the introductory chapter of the thesis, the choice is made here for the LES in the modelling of the reactive flows of interest, since the LES approaches provide a number of important advantages compared to RANS-based models [38], in particular, LES can directly capture the large scale information dictated by the flow geometry and modelling is only applied to the smallest, more universal scales of turbulence.

In LES, a spatial filtering operator is employed in order to remove flow features that are smaller than a specified filter size, Δ. The large scales are the ones that contain most of the energy and are directly affected by the boundary conditions [35]. The small scales are generally more universal in character, and serve mainly as a source for dissipation. Hence, it can be argued that a better understanding of turbulent flows could be achieved if just the small scales are modelled while the large scales are calculated directly. The separation of scales is provided by means of a spatial filtering, where a high-pass in length (low-pass in frequency) filter is used. Mathematically, the filtering operation is represented by a convolution product. Given a variable, φ, dependent on time and space, its resolved component $\bar{\varphi}$ is given by

$$\bar{\varphi}(\mathbf{x},t) = \int_{\mathrm{D}} \mathfrak{G}\left(\mathbf{x}-\mathbf{x}';\boldsymbol{\Delta}(\mathbf{x})\right)\varphi(\mathbf{x}',t)\,\mathrm{d}\mathbf{x}'\,. \tag{2.41}$$

Here, the resolved component of a filtered variable will be denoted by an overbar. The convolution kernel of the filter is represented by the symbol $\mathfrak{G}$, and $\boldsymbol{\Delta}$ is the filter width, which defines the cutoff length scale associated with the size of the smallest scale retained by the filtering operation. The three classical types of filters are most commonly used for the spatial filtering in LES, the box or top hat filter, the Gaussian filter, and the spectral or sharp cutoff filter. For further details of these filter definitions, the reader may refer to Garnier *et al.* [84].

In this work, as in most LES approaches, an implicit filtering procedure is selected, so the shape of the filter is not formally defined. The filter width is taken to be a direct function of the mesh, with the filter width Δ being proportional to the local cell size h. In the general case, for anisotropic meshes the filter width is calculated as a function of the geometric average of the

mesh element dimensions in the three directions, $h=(h_x h_y h_z)^{1/3}$ [85].

2.3.3 Filtered Governing Equations

Having defined the concept of LES, the filtering operation applied to Equations (2.1)–(2.4) will yield the following filtered form of the conservation equations:

$$\frac{\partial \bar{\rho}}{\partial t} + \frac{\partial(\bar{\rho}\tilde{u}_j)}{\partial x_j} = 0\,, \tag{2.42}$$

$$\frac{\partial(\bar{\rho}\tilde{u}_i)}{\partial t} + \frac{\partial(\bar{\rho}\tilde{u}_i\tilde{u}_j + \delta_{ij}\bar{p})}{\partial x_j} - \frac{\partial \check{\tau}_{ij}}{\partial x_j} = \bar{\rho} g_i + \underbrace{\frac{\partial \sigma_{ij}}{\partial x_j}}_{\mathbf{I}} + \underbrace{\frac{\partial(\bar{\tau}_{ij} - \check{\tau}_{ij})}{\partial x_j}}_{\mathbf{II}}\,, \tag{2.43}$$

$$\begin{aligned}\frac{\partial(\bar{\rho}\tilde{E})}{\partial t} + \frac{\partial[(\bar{\rho}\tilde{E}+\bar{p})\tilde{u}_j]}{\partial x_j} - \frac{\partial(\check{\tau}_{ij}\tilde{u}_i)}{\partial x_j} + \frac{\partial \check{q}_j}{\partial x_j} \;=\; & \bar{\rho}\tilde{u}_i g_i - \underbrace{\frac{\partial[\bar{\rho}(\widetilde{h_{\mathrm{s}}u_j} - \check{h}_{\mathrm{s}}\tilde{u}_j)]}{\partial x_j}}_{\mathbf{III}} \\ & + \underbrace{\frac{\partial(\overline{\tau_{ij}u_i} - \check{\tau}_{ij}\tilde{u}_i)}{\partial x_j}}_{\mathbf{IV}} - \underbrace{\frac{\partial(\bar{q}_j - \check{q}_j)}{\partial x_j}}_{\mathbf{V}} \\ & - \underbrace{\frac{1}{2}\frac{\partial[\bar{\rho}(\widetilde{u_j u_i u_i} - \tilde{u}_j\widetilde{u_i u_i})]}{\partial x_j}}_{\mathbf{VI}} \\ & - \underbrace{\frac{\partial[\sum_{\alpha=1}^{N}\Delta h^0_{\mathrm{f}_\alpha}\bar{\rho}(\widetilde{Y_\alpha u_j} - \tilde{Y}_\alpha\tilde{u}_j)]}{\partial x_j}}_{\mathbf{VII}}\,,\end{aligned} \tag{2.44}$$

$$\frac{\partial(\bar{\rho}\tilde{Y}_\alpha)}{\partial t} + \frac{\partial(\bar{\rho}\tilde{Y}_\alpha\tilde{u}_j)}{\partial x_j} + \frac{\partial \check{\mathcal{J}}_{j,\alpha}}{\partial x_j} = - \underbrace{\frac{\partial[\bar{\rho}(\widetilde{Y_\alpha u_j} - \tilde{Y}_\alpha\tilde{u}_j)]}{\partial x_j}}_{\mathbf{VIII}} - \underbrace{\frac{\partial(\bar{\mathcal{J}}_{j,\alpha} - \check{\mathcal{J}}_{j,\alpha})}{\partial x_j}}_{\mathbf{IX}} + \underbrace{\bar{\dot{\omega}}_\alpha}_{\mathbf{X}}\,, \tag{2.45}$$

where the filtered equation of state becomes

$$\bar{p} = \bar{\rho}\check{R}\tilde{T} + \underbrace{\sum_{\alpha=1}^{N} R_\alpha\bar{\rho}(\widetilde{Y_\alpha T} - \tilde{Y}_\alpha\tilde{T})}_{\mathbf{XI}}\,. \tag{2.46}$$

The SFS stress tensor appearing above is given by

$$\sigma_{ij} = -\bar{\rho}\,(\widetilde{u_i u_j} - \tilde{u}_i\tilde{u}_j)\,, \tag{2.47}$$

An expression for the Favre-filtered total energy takes the form

$$\tilde{E} = \check{h}_\mathrm{s} - \frac{\bar{p}}{\bar{\rho}} + \sum_{\alpha=1}^{N} \Delta h^0_{\mathrm{f}_\alpha} \tilde{Y}_\alpha + \frac{1}{2}\tilde{u}_i\tilde{u}_i + k_\Delta \,, \tag{2.48}$$

where the SFS turbulent kinetic energy can be defined by

$$k_\Delta = \frac{1}{2}\left(\widetilde{u_i u_i} - \tilde{u}_i\tilde{u}_i\right) \,, \tag{2.49}$$

Note that some terms appearing in Equations (2.42) – (2.46) are marked using Roman symbols (terms **I**,...,**XI**) denoting terms where the influence of subfilter scales on the resolved scales appear and where additional modelling is required.

It is convenient to use the check symbol, $\check{}$, to emphasize terms that are calculated based on filtered variables as, for example, the gas constant $\check{R} = R(\tilde{Y}_\alpha)$ and the sensible enthalpy $\check{h}_\mathrm{s} = h_\mathrm{s}(\tilde{Y}_\alpha, \tilde{T})$. Following this idea, the fluxes $\check{\tau}_{ij}$, $\check{q}_j$, and $\check{\mathcal{J}}_{j,\alpha}$ can therefore be written as

$$\check{\tau}_{ij} = 2\check{\mu}\left(\check{S}_{ij} - \frac{1}{3}\delta_{ij}\check{S}_{ll}\right) \,, \tag{2.50}$$

$$\check{q}_j = -\check{\lambda}\frac{\partial\tilde{T}}{\partial x_j} - \bar{\rho}\sum_{\alpha=1}^{N}\check{h}_\alpha\check{D}_\alpha\frac{\partial\tilde{Y}_\alpha}{\partial x_j} \,, \tag{2.51}$$

$$\check{\mathcal{J}}_{j,\alpha} = -\bar{\rho}\check{D}_\alpha\frac{\partial\tilde{Y}_\alpha}{\partial x_j} \,, \tag{2.52}$$

In the above equations, the molecular transport coefficients $\check{\mu}$, $\check{\lambda}$, and $\check{D}_\alpha$ are all evaluated at the filtered temperature $\tilde{T}$. Also, the strain rate tensor $\check{S}_{ij}$ is evaluated in terms of the Favre-filtered velocity with $\check{S}_{ij} = \frac{1}{2}\left(\partial\tilde{u}_i/\partial x_j + \partial\tilde{u}_j/\partial x_i\right)$. Finally and for completeness, the spatially filtered version of the conservation equation for the progress variable becomes [69]

$$\frac{\partial(\rho\tilde{c})}{\partial t} + \frac{\partial(\rho\tilde{u}_i\tilde{c})}{\partial x_i} + \frac{\partial}{\partial x_i}[\rho\left(\widetilde{u_i c} - \tilde{u}_i\tilde{c}\right)] = \frac{\partial}{\partial x_i}\left(\overline{\rho\mathcal{D}_\mathrm{c}\frac{\partial c}{\partial x_i}}\right) + \bar{\dot{\omega}}_\mathrm{c} \,. \tag{2.53}$$

2.4 Turbulent Combustion Modelling for Premixed Flames

As explained by Cant [40] and Veynante and Vervisch [73], as RANS and LES both have averaging/filtering lengths and time scales that are related to the nature of turbulence, similar modelling strategies can be used to account for the contribution of the non-resolved scales in either of these two modelling techniques. The basic tools and formalism are shared by RANS and LES combustion modelling, so that RANS models are frequently extended to LES frameworks.

It is important to emphasize that despite the approaches being similar, the meaning of time averaged and filtered quantities are different and distinct, requiring a careful interpretation of the meaning in each case [73].

As noted above, The filtered Navier-Stokes equations of Equations (2.42)–(2.45) given in Section 2.3.3 contain a number of unclosed terms which are marked using roman symbols (terms **I**,...,**XI**) and will require proper modelling. The following is a summary of the modelling options used for each of these terms:

- Term **I** — the modelling of the subfilter scale (SFS) stresses are discussed in a dedicated Section 2.4.2.
- Term **II** — total momentum diffusion flux is neglected following the assumption that the filtered viscous stresses, $\bar{\tau}_{ij}$, and the viscous stresses evaluated in terms of the Favre-filtered velocity, $\check{\tau}_{ij}$ are similar.
- Term **III** — the modelling of the SFS heat flux is discussed in Section 2.4.1;
- Term **IV** — the subfilter scale viscous diffusion is neglected as this term is taken to be much smaller than the other terms requiring modelling [86];
- Term **V** — the total heat diffusion flux is neglected by analogous reasoning to term **II**, by assuming that the filtered heat flux and the heat flux evaluated in terms of the Favre filtered temperature are similar;
- Term **VI** — the subfilter scale turbulent diffusion is modelled in terms of the SFS stresses and the resolved velocity as [87]

$$-\frac{\bar{\rho}\left(\widetilde{u_j u_i u_i} - \tilde{u}_j \widetilde{u_i u_i}\right)}{2} = \sigma_{ij}\tilde{u}_i\,. \tag{2.54}$$

- Term **VII** — This term is closed with the SFS species fluxes (term **VIII**);
- Term **VIII** — The SFS species flux is discussed in Section 2.4.1;
- Term **IX** — The total species diffusion flux is neglected by analogous reasoning to terms **II** and **V**, the filtered species flux and species flux evaluated in terms of Favre filtered species mass fractions are similar;
- Term **X** — The filtered reaction rates, $\bar{\dot{\omega}}_\alpha$, are discussed in dedicated Section 2.4.3.
- Term **XI** — The subfilter scale temperature-species correlation is assumed to be small and is neglected.

2.4.1 Subfilter Scale Fluxes

Turbulent transport in premixed flames is related to both mixing due to turbulence and acceleration due to heat release. To account for the turbulent transport due to turbulent mixing the gradient hypothesis has been widely utilized to model SFS fluxes. Heat release effects are the main source of counter-gradient transport. Heat release causes a thermal expansion that promotes the counter-gradient pressure-driven transport. It has been shown that counter-gradient transport may occur in premixed flames, and it is also acknowledged that accounting for its effect makes the modelling of turbulent transport significantly harder [40]. Nevertheless, a commonly used gradient approximation is selected here, as is also the practice in previous studies [36]. This option was successfully adopted in previous research efforts sharing the same particular implementation used here [88, 68]. It has also been argued [89] that in the particular case of LES, the modelled counter-gradient transport is not so relevant as in RANS, since the flame structure is partially resolved in LES.

The subfilter heat flux (Term **III**) and the subfilter species flux (Term **VIII**), as well as the subfilter flux $\left(\widetilde{\psi u_j} - \tilde{\psi}\tilde{u}_j\right)$, for any given transported scalar ψ, can be described using a generalized gradient transport assumption, as follows:

$$\left(\widetilde{\psi u_j} - \tilde{\psi}\tilde{u}_j\right) = -\zeta_{\mathrm{t}} \frac{\partial \tilde{\psi}}{\partial x_j} \,. \tag{2.55}$$

The subfilter turbulent diffusivity ζ_{t} can be defined for the scalar ψ, which relates the diffusivity of scalar ψ with the eddy-viscosity (momentum diffusivity). For the energy equation, the coefficient ζ_{t} is modelled as $\zeta_{\mathrm{t}} = \nu_{\mathrm{t}}/Pr_{\mathrm{t}}$. For the case of the heat flux, the subfilter turbulent diffusivity becomes $\zeta_{\mathrm{t}} = \nu_{\mathrm{t}}/Pr_{\mathrm{t}}$ and for the case of the subfilter species diffusivity it becomes $\zeta_{\mathrm{t}} = \nu_{\mathrm{t}}/Sc_{\mathrm{t}}$. Analogous relations can be also defined for other scalars commonly used in turbulent combustion, such as the progress variable and the mixture fraction.

2.4.2 Subfilter Scale Stress

The SFS stresses represent the transfer of energy from the resolved flow to the small scales, where it is dissipated. A *separation of scale hypothesis* (the subgrid and resolved scales are totally separated) and a *local equilibrium hypothesis* (there is no accumulation of energy at any frequency, the energy spectrum is invariant with time) are assumed [84]. Following also a Boussinesq-like hypothesis, the deviatoric part of the SFS stress tensor, for a compressible flow,

is given by

$$\sigma_{ij} - \frac{1}{3}\delta_{ij}\sigma_{ll} = 2\bar{\rho}\nu_{\mathrm{t}}\left(\check{S}_{ij} - \frac{1}{3}\delta_{ij}\check{S}_{ll}\right), \tag{2.56}$$

In the present work, two approaches are considered for modelling the SFS stress. The first is the Smagorinsky model, where the turbulent viscosity is modelled directly as a function of the filter size, Δ as

$$\nu_{\mathrm{t}} = (C_{\mathrm{s}}\Delta)^2|\check{S}|\,, \tag{2.57}$$

and

$$|\check{S}| = \sqrt{2\check{S}_{ij}\check{S}_{ij}}\,. \tag{2.58}$$

The filter width, Δ, is a characteristic length scale of the flow (related to the mesh size for the implicit implementation considered here).

Alternatively, a one-equation eddy-viscosity model is also available, which is based on a transport equation for the SFS turbulent kinetic energy, k_Δ [90, 91]. In this approach, the SFS stresses are modelled as

$$\sigma_{ij} = 2\bar{\rho}\nu_{\mathrm{t}}\left(\check{S}_{ij} - \frac{1}{3}\delta_{ij}\check{S}_{ll}\right) - \bar{\rho}\frac{2}{3}\delta_{ij}k_\Delta\,, \tag{2.59}$$

where

$$\nu_{\mathrm{t}} = C_\nu k_\Delta^{1/2}\Delta\,, \tag{2.60}$$

and the value of k_Δ is obtained from the solution of an additional transport equation given by

$$\frac{\partial(\bar{\rho}k_\Delta)}{\partial t} + \frac{\partial(\bar{\rho}k_\Delta\tilde{u}_i)}{\partial x_i} = \sigma_{ij}\check{S}_{ij} - \frac{C_\epsilon\bar{\rho}k_\Delta^{3/2}}{\Delta} + \frac{\partial}{\partial x_i}\left[\bar{\rho}\left(\check{\nu} + \frac{\nu_{\mathrm{t}}}{\zeta^*}\right)\frac{\partial k_\Delta}{\partial x_i}\right]. \tag{2.61}$$

2.4.3 Filtered Reaction Rates

The modelling of Term **X**, the filtered reaction rate, is of special importance in combustion modelling since this is the term that accounts for the destruction and production of the species involved in the chemical reactions. The reaction rates are non-linear functions of temperatures and species mass fractions. Additionally, as described previously, the typical length scales where the reactions occur are usually thinner than LES grids and therefore almost all of the turbulence-chemistry interaction needs to be modelled.

Several reaction rate models have been developed to close the filtered equations, from simpler algebraic expressions to more complex models like the Conditional Moment Closure (CMC) [92, 93] or Transported Probability Density Functions (PDF) methods [94]. One important thing to consider, as typically is the case in numerical modelling, is the balance between accuracy and

computational cost. Depending on the level of detail required and depending on the acceptable compromises, the available models will be more or less attractive to a particular application. In this section, a brief presentation of some of these alternatives is given for premixed flames, followed by a more detailed description of the particular modelling strategy selected in this thesis, the PCM-FPI model.

Arrhenius Law Based on Filtered Quantities

The simplest approach to modelling of the reaction rate is to use an Arrhenius-type formulation in which the reaction rates are based entirely on filtered quantities [95]. This assumes that the LES grid is able to resolve all the reaction zone. This is usually not true for combustion applications, although variations of the Arrhenius law have been derived aiming to account for subgrid contribution, with limited practical use [96].

Algebraic Models

One important type of closure model for the reaction rates are the algebraic models based on the Eddy-Break-Up (EBU) concept, first presented by Spalding [97]. These models are very simple and have low computational cost. Assuming that chemistry is fast, turbulent mixing is the factor that controls the reaction rate. Expressions are devised relating the rate of mixing to be function of the particular turbulence model time scales (ϵ/k in two-equation RANS or filter width, Δ/u' in LES). Despite being very useful, particularly because the model is computationally inexpensive, one important limitation of EBU models is that it is difficult to incorporate the effects of complex chemistry.

Thickened Flame Models

Another flame modelling option is the Thickened Flame (TF) approach. This model was first derived based on laminar flames concepts by Butler and O'Rourke [98]. The interesting idea behind this model is that the flame is artificially thickened by a factor, F, so that it becomes resolvable by the available LES grid. The thickening of the flame is based on the fact that the laminar flame speed, S_L, is given as a function of the geometric mean of the molecular diffusivity, $\mathcal{D}$, and the mean reaction rate, $\mathcal{W}$, ($S_\mathrm{L} \propto \sqrt{\mathcal{D}\mathcal{W}}$) and that the laminar flame thickness is related to the flame speed as $\delta_\mathrm{L} \propto \mathcal{D}/S_\mathrm{L}$. To obtain the thickened flame thickness, $\delta_\mathrm{L,thick} = F\delta_\mathrm{L}$, the thermal and molecular diffusivities are substituted by $\mathcal{D}_\mathrm{th,thick} = F\mathcal{D}_\mathrm{th}$ and $\mathcal{D}_\mathrm{thick} = F\mathcal{D}$, respectively. Also, the mean reaction rate, $\mathcal{W}$, is modified by being divided by the factor, F, so that $\mathcal{W}_\mathrm{thick} = \mathcal{W}/F$. This results in a thickening of the flame, preserving the laminar flame speed such that

$$s_{\mathrm{L,thick}} \propto \sqrt{\mathcal{D}_{\mathrm{thick}}\mathcal{W}_{\mathrm{thick}}} = \sqrt{F\mathcal{D}\frac{\mathcal{W}}{F}} = \sqrt{\mathcal{D}\mathcal{W}} = S_{\mathrm{L}}\,,$$

$$\delta_{\mathrm{L,thick}} \propto \frac{\mathcal{D}_{\mathrm{thick}}}{s_{\mathrm{L,thick}}} = \frac{F\mathcal{D}}{S_{\mathrm{L}}} = F\delta_{\mathrm{L}}\,.$$

The thickening factor, F, is usually in the range from 5 to 30 allowing the flame front to be resolved on the LES computational mesh. An efficiency factor, E_{F}, is defined to compensate for the decrease in Damköhler number resulting from the introduction of the factor, F. Using Arrhenius relations to estimate $\bar{\dot{\omega}}_\alpha$, the species mass fraction conservation equation can then be written, in an artificially thickened flame context, as

$$\frac{\partial(\bar{\rho}\tilde{Y}_\alpha)}{\partial t} + \frac{\partial(\bar{\rho}\tilde{Y}_\alpha\tilde{u}_j)}{\partial x_j} = \frac{\partial}{\partial x_j}\left(E_{\mathrm{F}}F\check{\mathcal{D}}_\alpha\frac{\partial\tilde{Y}_\alpha}{\partial x_j}\right) + \frac{E_{\mathrm{F}}}{F}\bar{\dot{\omega}}_\alpha\,. \tag{2.62}$$

The thickened flame model has the advantage of being extendable to complex chemistry by including as many modified species conservation equations (Equation (2.62)) as desired, although the proper choice of the thickening factor will have a large impact in the results, what may require some *ad-hoc* adjustments depending on the case. Also, according to Pitsch [36], the effect of heat release on the flow field cannot be properly resolved. It is also suggested that a possible way, although not straightforward, to make this model more accurate would be to couple the model with adaptive mesh refinement so that better flame resolution is achieved locally, where needed. Dynamically thickened flames, where the flame is thickened in an adaptive way based on the local resolution of flame scales have also gained in popularity recently [99, 100].

Flame Surface Density Models

Flame surface density (FSD) models introduce a variable related to the flame surface area that is contained within one unit volume at each location inside the flame brush. The flame surface density is a measure of the amount of wrinkling a turbulent flame achieves at a given location. Within a LES framework, the progress variable equations can be written as shown in Equation (2.53) and a FSD model can be used to provide the filtered reaction rate. The idea behind it being that the flame surface density, Σ, can be combined with a local flame propagation speed in order to calculate the volumetric rate of consumption of the unburned gases.

There are several different models to calculate the flame surface density including simpler algebraic expressions and models based on transport equations for the conservation of flame surface

density. Among the algebraic models used in conjunction with LES is the work of Boger *et al.* [89]. The development of transport equations for surfaces describing flames goes back to the works of Pope [101] and Candel and Poinsot [102]. Transport equations for FSD in LES have then been used by Boger *et al.* [89] and later Hawkes and Cant [103] developed a FSD formulation that models the subfilter scales and also includes the resolved scales of the flame. Finally, Lin [104] used a FSD modelling to numerically predict premixed turbulent flames.

G-Equation Model

The level set approach was originally developed for geometry description by Osher and Sethian [105]. In the G-Equation model for premixed combustion, based on the level set approach, the flame front is tracked by a signed G function which is calculated at each location of the domain. Conventionally, a value $G = 0$ indicates the position of the flame front and, typically, $G < 0$ would indicate the unburnt mixture, and $G > 0$ would be the burnt gases region.

The G function is determined by solving the following transport equation:

$$\frac{\partial G}{\partial t} + \mathbf{u} \cdot \nabla G = w|\nabla G| \,. \tag{2.63}$$

The G-equation approach is not a particular combustion model, rather a numerical strategy devised to deal with the flame resolution problem [36]. A closure model is still required to prescribe the speed of the flame front. In Equation (2.63), w is a relative propagation speed of the flame front, and this term requires modelling [1].

Probability Density Function Methods

One important category of closure strategies for the turbulent chemistry source terms is the method of transported PDFs, as first introduced by Pope [106]. The use of a statistical approach to evaluate turbulent quantities in reactive flows has been quite widely explored [107] and tested for different flow regimes and applications. For the case of variable density flows, the density-weighted PDF can be used and the filtered reaction term can be written using

$$\bar{\dot{\omega}}(\mathbf{x}, t) = \int \dot{\omega}(\boldsymbol{\psi}) P(\boldsymbol{\psi}; \mathbf{x}, t) \, \mathrm{d}\boldsymbol{\psi} \,, \tag{2.64}$$

where $\dot{\omega}(\mathbf{x}, t) = \dot{\omega}\left(\boldsymbol{\varphi}(\mathbf{x}, t)\right)$, is the reaction rate, $\boldsymbol{\varphi} = [\varphi_1, \varphi_2, \ldots, \varphi_{N_\mathrm{s}}]$ is an array of N_s scalars (species mass fractions and temperature), and $\boldsymbol{\psi}$ is the array of statistical random variables associated with $\boldsymbol{\varphi}$. The PDF value can be defined by solving a specific transport equation for the PDF shape often using particle-based methods, which can be of very high computational

cost, or can be defined by assuming the PDF shape *a priori*. Some more details on assumed PDFs are given in Section 2.5.1.

Conditional Moment Closure

The conditional moment closure (CMC) model is a relatively recent model. The original CMC equations first were derived by Klimenko [92] and first was developed for non-premixed combustion but it can and has been extended to partially premixed and premixed flames [108]. The main idea behind this method is to use the fluctuations of a conditioning variable to calculate the fluctuation in a conditioned variable. The assumption is that the fluctuations of the conditioned variables are strongly related to the fluctuations of the conditioning variable. In other words, scalar quantities of interest (as reactive scalar species mass fractions, for example) are conditioned to another variable (the conditioning variable, like the mixture fraction, for example). For premixed systems, fluctuations in species mass fractions and in temperature can be related to the fluctuations in the reaction progress variable. Transport equations are derived for the conditional moments of the scalars. The CMC model has been successfully applied to a wide variety of flows but the cost associated with this method in three-dimensional case is very high and has been compared to that of DNS simulations [108]. A classic review of this method is given in the work of Klimenko and Bilger [109] and complemented by Kronenburg and Mastorakos [108]. Nevertheless, the CMC method is not well established yet for premixed flames.

Conditional Source Estimation

The conditional source estimation (CSE) model of Bushe and Steiner [110] was developed having as inspiration some of the concepts of the CMC model. In this method, transport equations are solved for the unconditional values of the scalars and the CMC idea is applied to determine the conditioned filtered scalars. The conditionally averaged scalar values are then combined with a PDF to provide the source terms. This method has also been successfully applied to the LES of premixed flames by Shahbazian *et al.* [111] and Shahbazian [112].

2.4.4 Reduced Chemical Kinetics via Tabulation

Complex chemical mechanisms with multiple steps, multiple components are typically found in combustion systems. This is particularly true for complex fuels, but even for a simple fuel like methane, combustion mechanisms may require hundreds of reactions and tens of species [113]. In order to keep computational costs down, several strategies have been proposed to simplify the description of the chemical kinetics. The simplest approach to achieving this goal is to

reduce the number of reactions steps by adopting single-step or few-step reaction mechanisms that are representative of the overall global behaviour, thus also allowing the number of species participating in the description to be greatly reduced. These approaches are usually less accurate and only useful for less detailed studies, or for comparative purposes if capturing the intermediate chemistry and pollutants properly is not the goal.

Other types of reduction techniques rely on the observation that combustion systems usually involve many steps with a much smaller time scale in comparison to the flow time scales. According to Ren *et al.* [114], the reaction trajectories rapidly approach a hierarchy of attracting manifolds of decreasing dimension in the full composition space, or, in other words, the dynamics of the initially very complex system (large number of reactions and large number of species) are quickly dominated by a smaller number of variables that can represent the behaviour of the full detailed system. This allows for the development of low dimension tabulations of these mechanisms, where only a few dominant equations for the reduced set of variables are solved. Different strategies are available to develop these tables and some of these tabulation techniques include the Flame Generated Manifolds (FGM) [41], the Reaction-Diffusion Manifolds (REDIM) [115], the Invariant Constrained-Equilibrium edge manifold using Pre-Image Curve (ICE-PIC) [114], the Intrinsically Low Dimension Manifolds (ILDM) [116] and the FPI [42]. In the present work, the look-up tables have been generated following the previous work of Hernàndez-Pérez *et al.* [88] and Shahbazian *et al.* [68], where a FPI [42] type of table for the chemical kinetics is used.

2.5 Presumed Conditional Moments and FPI

Having presented some of the available strategies to achieve the turbulence-chemistry closure in LES for reactive flows, this section is dedicated to a more detailed description of the method of choice for the present thesis: the PCM combined with FPI chemistry tabulation. Having in mind that the main goal of this work is to implement and apply a high-order, finite-volume scheme to the LES of premixed flames, allowing some performance comparisons with a legacy second-order spatial discretization scheme, it is convenient to use a model that has been the subject of previous research work within the research group at the University of Toronto [69, 68, 117, 70, 71]. The particular model selected here provides the ability to represent complex chemistry at a relatively low cost with reasonable accuracy.

FPI Tabulation

As discussed above, solving transport equations for each of the species in a complex mechanism can be a prohibitive task from the point of view of computational cost in practical LES. Having a system that is extremely simplistic, considering for example only one- or two-step mechanisms may be beneficial from a cost point of view but may overlook the description of minor species. If one is interested in the ability to predict pollutants, then there is the need to take into account the behaviour of some intermediate radical species. In this sense, chemistry tabulation approaches become very attractive, offering the opportunity to retain the accuracy of complex chemistry by building databases of relevant quantities based on detailed simulations of simple representative flames.

The tabulation approach used in the present work is an extension of the ILDM idea of Maas and Pope [116]. The model used here is the FPI technique, originally developed by Gicquel *et al.* [42] based on one-dimensional premixed laminar flamelets. It can be used in both premixed or non-premixed cases, consequently being also suitable to the partially premixed regime. The first step in this method is the solution of one-dimensional (1D) laminar flames for the equivalence ratios of interest: one flame at the equivalence ratio of the fuel-oxidant mixture in the case of tabulation for premixed combustion or an appropriate range of equivalence ratios covering the possible situations for a non-premixed combustion [117]. The results from the one-dimensional laminar flames calculations are then stored as a function of a single progress of reaction variable, Y_c. Since the progress variable provides, by definition, a bijective mapping of the 1D flame, it is directly related to the position of the flame front, x. In this sense, any property, φ_α (species mass fractions or reaction rates), of the steady-state laminar flame at a selected equivalence ratio, ϕ_0, can be mapped as function of the position, x, $\varphi_\alpha = \varphi_\alpha(\phi_0, x)$, or mapped directly to a progress of reaction variable, Y_c-space, eliminating x.

The FPI table may then be written as

$$\varphi_\alpha^{\mathrm{FPI}}(\phi_0, Y_c) = \varphi_\alpha(\phi_0, x)\,. \tag{2.65}$$

For methane flames, it was shown by Fiorina *et al.* [118] that the choice for the progress variable $Y_c = Y_{CO_2}$ alone is not appropriate because the mapped variables would present non-monotonic behaviour as function of Y_{CO_2} only. An important requirement of the look-up table approach is that the dependent variables are uniquely mapped by the progress variables, without ambiguity. Fiorina *et al.* [118] showed that a linear combination of the form

$$Y_c = Y_{CO_2} + Y_{CO} \tag{2.66}$$

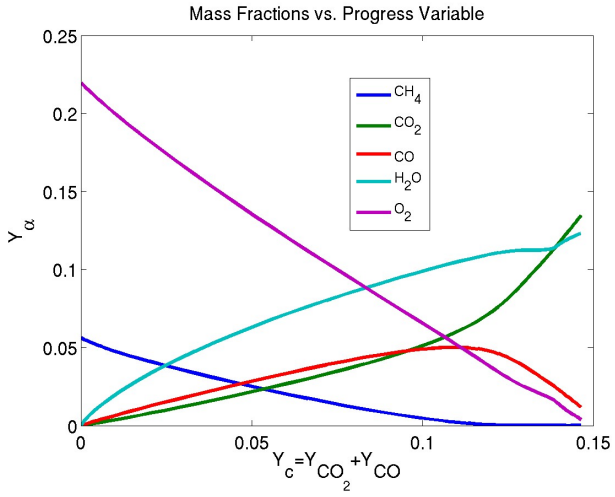

Figure 2.3: Mass fractions as function of $Y_c = Y_{CO_2} + Y_{CO}$ for premixed 1D laminar flame(CH_4, ϕ=1.0)

is an appropriate choice of progress variable, providing a good monotonically varying basis for prediction of major species in methane-air flames using tabulations [118]. For the case of the one-dimensional flame solution illustrated in Figure 2.1, the variation of species mass-fractions as a function of the progress variable $Y_c = Y_{CO_2} + Y_{CO}$ is well represented as depicted in Figure 2.3.

In this work, one-dimensional, premixed, methane-air flames are pre-computed using the Cantera software package [119] with the GRI-Mech 3.0 mechanism [113]. According to the studies performed by Hernàndez-Pérez *et al.* [88], Hernàndez-Pérez [69], Hernàndez-Pérez *et al.* [120], 10 species are selected as the most representatives, accounting for about 99% of the total mass, energy and heat release. The selected species are: CH_4, O_2, N_2, H_2O, CO_2,CO, H_2, H, OH, and C_2H_2. These species also match those used in previous works by Galpin *et al.* [121]. Also, the combustion processes studied here will not involve heat losses, recirculation zones of burned gas and do not present significant pressure variations so the tabulation used here is for adiabatic flame at a single pressure value (atmospheric). If non-adiabatic processes or significant pressure variations are present, the tabulations would have to be modified to include a larger range of these variables, increasing the table dimensions.

For the turbulent flames of interest here, the PCM [28, 122] method is used in combination with the FPI chemistry reduction technique for the closure of the chemistry-turbulence coupling and is discussed in the next subsection.

2.5.1 Presumed Conditional Moments

In the present work, the FPI tabulation technique [42] is coupled with PCM [28, 122] and probability density functions to account for detailed chemistry in the turbulent-chemistry interactions. In this sense, the PCM approach can be regarded as a simplified version of the CMC method, where the conditional moments are presumed rather than solved by dedicated transport equations. The PCM method uses a statistical treatment and a flamelet assumption to model the Favre-filtered reaction rate for a species α, $\tilde{\dot{\omega}}_\alpha$. The filtered reaction rate can be evaluated by combining a laminar reaction rate, $\dot{\omega}_\alpha$, and introducing a joint subfilter PDF, $\tilde{P}$, as

$$\tilde{\dot{\omega}}_\alpha = \int_{T^*}\int_{Y_1^*}\dots\int_{Y_N^*} \dot{\omega}_\alpha(T^*, Y_1^*, \dots, Y_N^*)\tilde{P}(T^*, Y_1^*, \dots, Y_N^*)\,\mathrm{d}Y_N^*\dots\mathrm{d}Y_1^*\mathrm{d}T^*\,. \tag{2.67}$$

In the more general case of non-premixed combustion, this description can be simplified assuming that the laminar reaction rate is characterized by only two parameters: a mixture fraction, Z, and a progress variable, c. Both variables range from zero to unity, being the mixture fraction related to the fuel-oxidizer mixing and the progress variable incorporates the effect of the reaction evolution. The filtered reaction rate can then be re-written as

$$\tilde{\dot{\omega}}_\alpha = \int_0^1\int_0^1 \dot{\omega}_\alpha(c^*, Z^*)\tilde{P}(c^*, Z^*)\,\mathrm{d}c^*\mathrm{d}Z^*\,. \tag{2.68}$$

where the filtered conditional moment $\overline{(\dot{\omega}|Z^*)}$ is given by

$$\overline{(\dot{\omega}|Z^*)} = \int_0^1 \dot{\omega}_\alpha(c^*, Z^*)\tilde{P}(c^*)\mathrm{d}c^*\,. \tag{2.69}$$

In the particular case of an adiabatic premixed flame at a specific mixture fraction, a chemical quantity, $\tilde{\varphi}_\alpha$, can be described as functions of the progress variable only. Therefore, using a 1D-FPI chemistry tabulation and assuming a shape for the PDF, $\tilde{P}(c^*)$, based on first, $\tilde{c}$, and second, c_v, moments of c, one can write

$$\tilde{\varphi}_\alpha = \int_0^1 \overline{\varphi_\alpha|c^*}\tilde{P}(c^*;\tilde{c},c_\mathrm{v})\mathrm{d}c^* = \int_0^1 \varphi_\alpha(c^*;\phi_0)^{\mathrm{1D-FPI}}\tilde{P}(c^*;\tilde{c},c_\mathrm{v})\,\mathrm{d}c^*\,, \tag{2.70}$$

where $\overline{\varphi_\alpha|c^*}$ is the conditionally-filtered value of φ_α for a given value $c = c^*$ of the reaction progress variable. In the PCM-FPI approach, the conditionally-filtered values are assumed to be equal to those provided by the laminar flamelet and are extracted from the 1D-FPI chemistry database as a function of the reaction progress variable, c^*.

A β-PDF is very commonly used as the presumed probability density function for the progress variable in both premixed and non-premixed flames [123, 121, 124, 125]. Besides the β-PDF, the laminar flame-based PDF of Bray *et al.* [126] and the modified laminar flame based PDF (MLPDF) of Jin *et al.* [127] are available in the present computational framework. Analysis of DNS data [127] and RANS simulation of a laboratory Bunsen burner [128] have shown that the MLPDF is a better choice for PDF of progress variable compared to the β-PDF. The MLPDF has been shown to be able to correctly maintain the filtered laminar flame speed in LES of Bunsen-type flames [67], while the β-PDF over-predicts the burning rate as observed in other previous studies [127, 128, 67]. Therefore, the MLPDF is considered to be a more appropriate choice for turbulent flames lying within the thin reaction zone regime and will be the choice for the laboratory flame studies presented in Chapter 4 of the thesis.

2.5.2 Conservation Equations for the PCM-FPI Model

Within a PCM-FPI framework for premixed combustion, the expression for a filtered quantity, $\tilde{\varphi}_\alpha$, from Equation (2.70) can be re-written as

$$\tilde{\varphi}_\alpha = \int_0^1 \varphi_\alpha^{\mathrm{FPI}} \tilde{P}(c^*)\,\mathrm{d}c^*\,, \tag{2.71}$$

meaning that the filtered value, $\tilde{\varphi}_\alpha$, results from the convolution of a probability density function, $\tilde{P}(c^*)$, with a function describing the variation of φ_α, a tabulation in this case. As described in Section 2.5.1, different forms of the PDF are available in the current computational framework. The actual value of the filtered PDF, $\tilde{P}(c^*)$, is calculated as function of the progress variable, $\tilde{c}$, and its variance, $c_{\mathrm{v}} = \widetilde{cc} - \tilde{c}\tilde{c}$. These two variables, $\tilde{c}$ and c_{v}, are related to the progress of reaction, $\tilde{Y}_{\mathrm{c}}$, and its SFS variance, $Y_{\mathrm{c_v}}$. In order to determine the values of Y_{c} and $Y_{\mathrm{c_v}}$, two extra conservation equations are used [122, 124, 121]. Details concerning the derivation and modelling of these equations and the relations between Y_{c} and $Y_{\mathrm{c_v}}$ with $\tilde{c}$ and c_{v} can be found in the work of Hernàndez-Pérez [69] and Shahbazian [112].

For premixed flames, only two additional transport equations are solved, used to characterize the shape of the PDF: one equation for the progress of reaction variable, Y_{c}, and another for the variance of the progress variable, $Y_{\mathrm{c_v}}$ [122, 124, 121]. The transport equation for $\tilde{Y}_{\mathrm{c}}$ used here is given by

$$\frac{\partial(\bar{\rho}\tilde{Y}_{\mathrm{c}})}{\partial t} + \frac{\partial(\bar{\rho}\tilde{u}_i\tilde{Y}_{\mathrm{c}})}{\partial x_i} = \frac{\partial}{\partial x_i}\left[\bar{\rho}(\check{\mathcal{D}}_{Y_{\mathrm{c}}} + \mathcal{D}_{\mathrm{t}})\frac{\partial \tilde{Y}_{\mathrm{c}}}{\partial x_i}\right] + \overline{\dot{\omega}}_{Y_{\mathrm{c}}}\,, \tag{2.72}$$

where $\overline{\dot{\omega}}_{Y_{\mathrm{c}}}$ is the progress variable source term based on the chemistry and the progress variable definition. The laminar and turbulent diffusivities are obtained by analogy with the mass

diffusion by prescribing an appropriate Schmidt number.

The variance, Y_{c_v}, has a transport equation as summarized by Domingo *et al.* [124], and which can be expressed as

$$\frac{\partial\left(\bar{\rho}Y_{c_v}\right)}{\partial t}+\frac{\partial\left(\bar{\rho}\tilde{u}_iY_{c_v}\right)}{\partial x_i}=\frac{\partial}{\partial x_i}\left[\bar{\rho}(\check{\mathcal{D}}_{Y_c}+\mathcal{D}_t)\frac{\partial Y_{c_v}}{\partial x_i}\right]+2\bar{\rho}(\check{\mathcal{D}}_{Y_c}+\mathcal{D}_t)\frac{\partial\tilde{Y}_c}{\partial x_i}\frac{\partial\tilde{Y}_c}{\partial x_i}$$
$$-2\overline{\rho\mathcal{D}_{Y_c}\frac{\partial Y_c}{\partial x_i}\frac{\partial Y_c}{\partial x_i}}+2(\overline{Y_c\dot{\omega}_{Y_c}}-\tilde{Y}_c\bar{\dot{\omega}}_{Y_c})\,. \tag{2.73}$$

Details of the modelling of the non-closed terms in Equation (2.73) are given in Hernàndez-Pérez [69] and Shahbazian [112]. The reaction rate can be written as $\dot{\omega}=\rho\dot{\omega}^*$, yielding $\bar{\dot{\omega}}=\bar{\rho}\tilde{\dot{\omega}}^*$, $\overline{Y_c\dot{\omega}_{Y_c}}=\bar{\rho}\widetilde{Y_c\dot{\omega}^*_{Y_c}}$, and $\overline{Y_c^{\mathrm{Eq}}\dot{\omega}_{Y_c}}=\bar{\rho}\widetilde{Y_c^{\mathrm{Eq}}\dot{\omega}^*_{Y_c}}$. The terms $\tilde{\dot{\omega}}^*_{Y_c}$ and $\widetilde{Y_c\dot{\omega}^*_{Y_c}}$ are saved in the tabulations, whereas the term $\widetilde{Y_c^{\mathrm{Eq}}\dot{\omega}^*_{Y_c}}$ is computed using $\widetilde{Y_c^{\mathrm{Eq}}\dot{\omega}^*_{Y_c}}=Y_c^{\mathrm{Eq}}\tilde{\dot{\omega}}^*_{Y_c}$, since Y_c^{Eq} is constant for a premixed regime. With the introduction of a segregation factor, S_c, which is a function of the variance [69], the PDF of c can be parametrized in terms of $\tilde{c}$ and S_c. Thus, the approach used here is to pre-generate a look-up table of filtered quantities $\tilde{\varphi}_\alpha^{\mathrm{PCM}}(\phi_0,\tilde{c},S_c)$, and use it directly in subsequent LES calculations.

2.6 Summary of Conservation Equations for LES of Premixed Flames

Having presented the conservation equations of interest for this work and explained the LES combustion modelling strategy adopted to deal with turbulence and chemistry interactions, we arrive at the set of partial differential equations that are solved when performing LES simulations considered herein. The general system of conservation equations of interest here can be written using matrix-vector notation as

$$\frac{\partial\mathbf{U}}{\partial t}+\nabla\cdot\vec{\mathbf{F}}=\mathbf{S}\,, \tag{2.74}$$

The bold symbols represent vectors whose sizes are the number of variables being used in the solution: $\mathbf{U}$ is the vector of conserved variables, $\vec{\mathbf{F}}$ is the total flux dyad, and $\mathbf{S}$ is the source term vector. The total flux dyad, $\vec{\mathbf{F}}$, is composed of an inviscid (hyperbolic) component, $\vec{\mathbf{F}}^{\mathbf{I}}$, and a viscous (elliptic) component, $\vec{\mathbf{F}}^{\mathbf{V}}$. The flux dyad can be written in terms of its vector

components as

$$\begin{aligned}\vec{\mathbf{F}} &= (\mathbf{F}_{\mathrm{x}}, \mathbf{F}_{\mathrm{y}}, \mathbf{F}_{\mathrm{z}}) \\ &= (\mathbf{F}_{\mathrm{x}}^{\mathbf{I}} - \mathbf{F}_{\mathrm{x}}^{\mathbf{V}}, \mathbf{F}_{\mathrm{y}}^{\mathbf{I}} - \mathbf{F}_{\mathrm{y}}^{\mathbf{V}}, \mathbf{F}_{\mathrm{z}}^{\mathbf{I}} - \mathbf{F}_{\mathrm{z}}^{\mathbf{V}}),\end{aligned} \tag{2.75}$$

where $\mathbf{F}_{\mathrm{x}}^{\mathbf{I}}$, $\mathbf{F}_{\mathrm{x}}^{\mathbf{V}}$, $\mathbf{F}_{\mathrm{y}}^{\mathbf{I}}$, $\mathbf{F}_{\mathrm{y}}^{\mathbf{V}}$, $\mathbf{F}_{\mathrm{z}}^{\mathbf{I}}$, and $\mathbf{F}_{\mathrm{z}}^{\mathbf{V}}$ are the components of inviscid and viscous flux vectors in the x-, y-, and z-coordinate directions, respectively.

In the particular case of the set of equations being considered in this thesis, the LES of reactive flows using PCM-FPI turbulent chemistry modelling transporting N species, the vectors described above ($\mathbf{U}$, $\mathbf{F}_{\mathrm{x}}^{\mathbf{I}}$, $\mathbf{F}_{\mathrm{x}}^{\mathbf{V}}$, $\mathbf{F}_{\mathrm{y}}^{\mathbf{I}}$, $\mathbf{F}_{\mathrm{y}}^{\mathbf{V}}$, $\mathbf{F}_{\mathrm{z}}^{\mathbf{I}}$, $\mathbf{F}_{\mathrm{z}}^{\mathbf{I}}$, and $\mathbf{S}$) can be written as

$$\mathbf{U} = \begin{bmatrix} \bar{\rho} \\ \bar{\rho}\tilde{u} \\ \bar{\rho}\tilde{v} \\ \bar{\rho}\tilde{w} \\ \bar{\rho}\tilde{E} \\ \bar{\rho}k_{\Delta} \\ \bar{\rho}\tilde{Y}_{\mathrm{c}} \\ \bar{\rho}Y_{\mathrm{c_v}} \\ \bar{\rho}\tilde{Y}_1 \\ \vdots \\ \bar{\rho}\tilde{Y}_N \end{bmatrix}, \tag{2.76}$$

and

$$\mathbf{F}_{\mathrm{x}}^{\mathbf{I}} = \begin{bmatrix} \bar{\rho}\tilde{u} \\ \bar{\rho}\tilde{u}\tilde{u} + \bar{p} + \bar{\rho}k_{\Delta} \\ \bar{\rho}\tilde{u}\tilde{v} \\ \bar{\rho}\tilde{u}\tilde{w} \\ (\bar{\rho}\tilde{E} + \bar{p})\tilde{u} \\ \bar{\rho}k_{\Delta}\tilde{u} \\ \bar{\rho}\tilde{Y}_{\mathrm{c}}\tilde{u} \\ \bar{\rho}Y_{\mathrm{c_v}}\tilde{u} \\ \bar{\rho}\tilde{Y}_1\tilde{u} \\ \vdots \\ \bar{\rho}\tilde{Y}_N\tilde{u} \end{bmatrix}, \quad \mathbf{F}_{\mathrm{y}}^{\mathbf{I}} = \begin{bmatrix} \bar{\rho}\tilde{v} \\ \bar{\rho}\tilde{u}\tilde{v} \\ \bar{\rho}\tilde{v}\tilde{v} + \bar{p} + \bar{\rho}k_{\Delta} \\ \bar{\rho}\tilde{v}\tilde{w} \\ (\bar{\rho}\tilde{E} + \bar{p})\tilde{v} \\ \bar{\rho}k_{\Delta}\tilde{v} \\ \bar{\rho}\tilde{Y}_{\mathrm{c}}\tilde{v} \\ \bar{\rho}Y_{\mathrm{c_v}}\tilde{v} \\ \bar{\rho}\tilde{Y}_1\tilde{v} \\ \vdots \\ \bar{\rho}\tilde{Y}_N\tilde{v} \end{bmatrix}, \quad \mathbf{F}_{\mathrm{z}}^{\mathbf{I}} = \begin{bmatrix} \bar{\rho}\tilde{w} \\ \bar{\rho}\tilde{u}\tilde{w} \\ \bar{\rho}\tilde{v}\tilde{w} \\ \bar{\rho}\tilde{w}\tilde{w} + \bar{p} + \bar{\rho}k_{\Delta} \\ (\bar{\rho}\tilde{E} + \bar{p})\tilde{w} \\ \bar{\rho}k_{\Delta}\tilde{w} \\ \bar{\rho}\tilde{Y}_{\mathrm{c}}\tilde{w} \\ \bar{\rho}Y_{\mathrm{c_v}}\tilde{w} \\ \bar{\rho}\tilde{Y}_1\tilde{w} \\ \vdots \\ \bar{\rho}\tilde{Y}_N\tilde{w} \end{bmatrix}, \tag{2.77}$$

$$\mathbf{F}_{\mathrm{x}}^{\mathbf{V}} = \begin{bmatrix} 0 \\ \check{\tau}_{\mathrm{xx}} + \sigma_{\mathrm{xx}} \\ \check{\tau}_{\mathrm{xy}} + \sigma_{\mathrm{xy}} \\ \check{\tau}_{\mathrm{xz}} + \sigma_{\mathrm{xz}} \\ \tilde{u}(\check{\tau}_{\mathrm{xx}} + \sigma_{\mathrm{xx}}) + \tilde{v}(\check{\tau}_{\mathrm{xy}} + \sigma_{\mathrm{xy}}) + \tilde{w}(\check{\tau}_{\mathrm{xz}} + \sigma_{\mathrm{xz}}) - (\check{q}_{\mathrm{x}} + \theta_{\mathrm{x}}) \\ \bar{\rho}(\frac{\nu_{\mathrm{t}}}{\zeta^*} + \check{\nu})\frac{\partial k_{\Delta}}{\partial x} \\ \bar{\rho}(\check{\mathcal{D}}_{Y_{\mathrm{c}}} + \mathcal{D}_{\mathrm{t}})\frac{\partial \tilde{Y}_{\mathrm{c}}}{\partial x} \\ \bar{\rho}(\check{\mathcal{D}}_{Y_{\mathrm{c}}} + \mathcal{D}_{\mathrm{t}})\frac{\partial Y_{\mathrm{c_V}}}{\partial x} \\ \bar{\rho}(\check{\mathcal{D}}_{1} + \mathcal{D}_{\mathrm{t}})\frac{\partial \tilde{Y}_{1}}{\partial x} \\ \vdots \\ \bar{\rho}(\check{\mathcal{D}}_{N} + \mathcal{D}_{\mathrm{t}})\frac{\partial \tilde{Y}_{N}}{\partial x} \end{bmatrix}, \tag{2.78}$$

$$\mathbf{F}_{\mathrm{y}}^{\mathbf{V}} = \begin{bmatrix} 0 \\ \check{\tau}_{\mathrm{xy}} + \sigma_{\mathrm{xy}} \\ \check{\tau}_{\mathrm{yy}} + \sigma_{\mathrm{yy}} \\ \check{\tau}_{\mathrm{yz}} + \sigma_{\mathrm{yz}} \\ \tilde{u}(\check{\tau}_{\mathrm{xy}} + \sigma_{\mathrm{xy}}) + \tilde{v}(\check{\tau}_{\mathrm{yy}} + \sigma_{\mathrm{yy}}) + \tilde{w}(\check{\tau}_{\mathrm{yz}} + \sigma_{\mathrm{yz}}) - (\check{q}_{\mathrm{y}} + \theta_{\mathrm{y}}) \\ 1\bar{\rho}(\frac{\nu_{\mathrm{t}}}{\zeta^*} + \check{\nu})\frac{\partial k_{\Delta}}{\partial y} \\ \bar{\rho}(\check{\mathcal{D}}_{Y_{\mathrm{c}}} + \mathcal{D}_{\mathrm{t}})\frac{\partial \tilde{Y}_{\mathrm{c}}}{\partial y} \\ \bar{\rho}(\check{\mathcal{D}}_{Y_{\mathrm{c}}} + \mathcal{D}_{\mathrm{t}})\frac{\partial Y_{\mathrm{c_V}}}{\partial y} \\ \bar{\rho}(\check{\mathcal{D}}_{1} + \mathcal{D}_{\mathrm{t}})\frac{\partial \tilde{Y}_{1}}{\partial y} \\ \vdots \\ \bar{\rho}(\check{\mathcal{D}}_{N} + \mathcal{D}_{\mathrm{t}})\frac{\partial \tilde{Y}_{N}}{\partial y} \end{bmatrix}, \tag{2.79}$$

$$\mathbf{F}_{\mathrm{z}}^{\mathbf{V}} = \begin{bmatrix} 0 \\ \check{\tau}_{\mathrm{xz}} + \sigma_{\mathrm{xz}} \\ \check{\tau}_{\mathrm{yz}} + \sigma_{\mathrm{yz}} \\ \check{\tau}_{\mathrm{zz}} + \sigma_{\mathrm{zz}} \\ \tilde{u}(\check{\tau}_{\mathrm{xz}} + \sigma_{\mathrm{xz}}) + \tilde{v}(\check{\tau}_{\mathrm{yz}} + \sigma_{\mathrm{yz}}) + \tilde{w}(\check{\tau}_{\mathrm{zz}} + \sigma_{\mathrm{zz}}) - (\check{q}_{\mathrm{z}} + \theta_{\mathrm{z}}) \\ \bar{\rho}(\frac{\nu_{\mathrm{t}}}{\zeta^*} + \check{\nu})\frac{\partial k_{\Delta}}{\partial z} \\ \bar{\rho}(\check{\mathcal{D}}_{Y_{\mathrm{c}}} + \mathcal{D}_{\mathrm{t}})\frac{\partial \tilde{Y}_{\mathrm{c}}}{\partial z} \\ \bar{\rho}(\check{\mathcal{D}}_{Y_{\mathrm{c}}} + \mathcal{D}_{\mathrm{t}})\frac{\partial Y_{\mathrm{c_V}}}{\partial z} \\ \bar{\rho}(\check{\mathcal{D}}_{1} + \mathcal{D}_{\mathrm{t}})\frac{\partial \tilde{Y}_{1}}{\partial z} \\ \vdots \\ \bar{\rho}(\check{\mathcal{D}}_{N} + \mathcal{D}_{\mathrm{t}})\frac{\partial \tilde{Y}_{N}}{\partial z} \end{bmatrix}, \tag{2.80}$$

with

$$\mathbf{S} = \begin{bmatrix} 0 \\ \bar{\rho} g_{\mathrm{x}} \\ \bar{\rho} g_{\mathrm{y}} \\ \bar{\rho} g_{\mathrm{z}} \\ \bar{\rho}(\tilde{u} g_{\mathrm{x}} + \tilde{v} g_{\mathrm{y}} + \tilde{w} g_{\mathrm{z}}) \\ (\sigma_{\mathrm{xx}} \check{S}_{\mathrm{xx}} + \sigma_{\mathrm{yy}} \check{S}_{\mathrm{yy}} + \sigma_{\mathrm{zz}} \check{S}_{\mathrm{zz}} + 2\sigma_{\mathrm{xy}} \check{S}_{\mathrm{xy}} + 2\sigma_{\mathrm{xz}} \check{S}_{\mathrm{xz}} + 2\sigma_{\mathrm{yz}} \check{S}_{\mathrm{yz}}) - \frac{C_\epsilon \bar{\rho} k_\Delta^{3/2}}{\Delta} \\ \bar{\dot{\omega}}_{Y_{\mathrm{c}}} \\ 2\bar{\rho}\mathcal{D}_{\mathrm{t}} |\nabla \tilde{Y}_{\mathrm{c}}|^2 - 2\bar{s}_{\chi_{Y_{\mathrm{c}}}} + 2(\overline{Y_{\mathrm{c}} \dot{\omega}_{Y_{\mathrm{c}}}} - \tilde{Y}_{\mathrm{c}} \bar{\dot{\omega}}_{Y_{\mathrm{c}}}) \\ \bar{\dot{\omega}}_1 \\ \vdots \\ \bar{\dot{\omega}}_N \end{bmatrix} . \tag{2.81}$$

In addition, the corresponding vector of primitive variables, $\mathbf{W}$, has the form

$$\mathbf{W} = \left[\bar{\rho}, \tilde{u}, \tilde{v}, \tilde{w}, \bar{p}, k_\Delta, \tilde{Y}_{\mathrm{c}}, Y_{\mathrm{c_v}}, \tilde{Y}_1, \ldots, \tilde{Y}_N\right]^{\mathrm{T}} . \tag{2.82}$$

In the above equation, θ_i represents the SFS heat flux, $\check{S}$ is the strain rate evaluated in terms of the Favre-filtered velocity, and $\tilde{u}, \tilde{v}$, and $\tilde{w}$ are the Favre-filtered velocity components in the x-, y-, and z-coordinate directions, respectively.

The number of species actually used in the PCM-FPI LES modelling discussed here is flexible and can vary depending on how one decides to model a particular problem. For the premixed methane-air flames as studied here, the complete GRI 3.0 mechanism uses 53 species and 325 reactions[113]. As commented previously in Section 2.5, the actual FPI tabulation shall focus only on the most relevant species, the ones that account for the most part of the mass, energy and heat release effects in the flame. For the methane-air flames, N =10 species are sufficient to account for 99% of these effects[88, 69, 121, 120].

Not considering the species conservation equations, the number of conservation equations being solved is eight (8): mass conservation, 3 momentum conservation (in x,y and z), energy conservation, subfilter k conservation, filtered progress variable and variance of progress variable conservation equations. The PCM-FPI model utilized in the present work can be used to provide either tabulated reaction rates or the tabulated mass fractions directly. Reading the mass fractions directly allows for substantial savings in computational cost, since in this case there is no need to solve the species conservation equations, being the system size reduced to $N_{eqns} = 8$.

If an option is made to actually solve the species conservation equations by reading the reaction rates from the tables, the total number of species conservation equations being solved would be $N_{eqns} = 8 + (N - 1)$, which would add to $N_{eqns} = 8 + 9 = 17$ in the present case. This happens because it can be argued that the number of species conservation equation is actually $N - 1$, since the N^{th} species mass fraction could be calculated by acknowledging that, from Equation (2.9), Y_N is by definition given by

$$Y_N = 1 - \sum_{\alpha=1}^{N-1} Y_\alpha \tag{2.83}$$

It has been previously shown, that reading the mass fractions from the tabulation does not compromise the accuracy of the results [69] and, in the present work, the option for retrieving the species mass fractions directly from the FPI tables is used for the majority of the studies, unless otherwise specified.

Chapter 3

Finite-Volume Formulation and High-Order CENO Scheme

The previous chapter describes the set of partial differential equations that are adopted here to provide a mathematical description of turbulent premixed flames. In this chapter, we explain the numerical methodology selected to solve these conservation equations for LES purposes, with the main goal of describing the proposed high-order finite-volume scheme. The first section of the chapter presents the motivation for using a finite-volume scheme. This is followed by a brief description of the main elements of finite-volume schemes. A description of mesh element types is then given, with particular attention to a generic hexahedral element and trilinear transformation which are of prime interest in the present work. This is followed by a detailed explanation of the proposed high-order, CENO, spatial discretization scheme used here for the numerical solution of the conservation equations. The chapter is closed with some verification tests for the proposed scheme in order to verify some aspects of the implementation of the high-order method.

3.1 Motivation for Finite-Volume Schemes

Several approaches are available for the numerical solution of systems of PDEs. Usually some type of discretization of the domain is a common requirement for all the methods. Among the most commonly used types of discretization methods are the finite-difference, finite-element and finite-volume. In order to solve the set of equations of interest, the strategy adopted here is to use a finite-volume formulation. In particular, a high-order form of this spatial discretization is investigated. According to Lomax *et al.* [13], finite-volume methods have gained in popularity because of their two general advantages:

1. the finite-volume method is conservative by construction, meaning that mass, momentum and energy are naturally conserved in a discrete sense when using a finite-volume method applied to the Navier-Stokes equations. The interface fluxes used in the computations ensure that quantities leaving/entering one control volume will necessarily be added to/subtracted from the neighbouring cell sharing that face; and

2. the fluxes can be computed directly at the point of evaluation, with respect to the surface normal at that point without the need of any type of coordinate transformation, even for irregular meshes. This flexibility has facilitated the use of unstructured grids, consisting of arbitrary polyhedra in three dimensions or arbitrary polygons in two dimensions. This is a very desirable property when considering real-life or practical applications, with complex geometries.

In industrial, practical CFD applications, the flexibility to deal with complex geometries is, in general, a strong requirement. This ability to conform to the geometry, no matter how complex its shape, is usually achieved by using unstructured meshes, where more flexible types of elements can be employed. Structured meshes require quadrilateral elements for two-dimensional domains or hexahedral elements in three-dimensional domains, and this may limit the ability to proper represent the geometry or may require a meshing process that is too complex. Not surprisingly, finite-volume formulations are today the most common methods found in commercial CFD software [129, 130], also because of the general ability of these methods to handle unstructured meshes. Despite not being treated specifically in this work, the ability to easily deal with unstructured meshes is a very important feature of any CFD method and is anticipated to be the object of future applications of the high-order methods examined herein. The present work focus on multi-block structured meshes, but due to the generality of the finite-volume implementation, the work can be seen as a stepping stone towards a future capability of dealing with fully unstructured grids [63]. Whenever it is pertinent, mention will be made in this thesis about the properties of the present scheme that make it attractive for unstructured meshes, but for now it suffices to have the ability of *easily transitioning to unstructured meshes in the future* as another motivation for using a finite-volume method.

The conservation equations for both non-reactive and reactive flow can typically be written in differential or integral form. Some of the advantages of considering the integral form of the conservation laws include the fact that the derivation of the governing equations from first principles is based on these conservation properties, which are naturally represented by the integral relations. Also an integral approach poses less stringent requirements regarding the smoothness of the solution, and that is a particularly useful property when dealing with discontinuous

solutions and shocks, as well as the possibly sharp flame fronts of interest here.

The conservation equations, as presented in Section 2.6, in differential form, can be integrated and combined with the divergence theorem to arrive at the following integral form:

$$\frac{d}{dt}\int_{V(t)} \mathbf{U}\,\mathrm{d}V + \oint_{\Omega(t)} \vec{n}\cdot\vec{\mathbf{F}}\,\mathrm{d}\Omega = \int_{V(t)} \mathbf{S}\,dV\,, \tag{3.1}$$

where Ω is the closed surface of the control volume, and $\vec{n}$ is the unit outward vector normal to the closed surface. The averaged values of $\overline{\mathbf{U}}$ and $\overline{\mathbf{S}}$ for the control volume of interest can be defined using

$$\overline{\mathbf{U}} = \frac{1}{V}\int_{V(t)} \mathbf{U}\,dV\,, \tag{3.2}$$

$$\overline{\mathbf{S}} = \frac{1}{V}\int_{V(t)} \mathbf{S}\,dV\,. \tag{3.3}$$

Using these two definitions, Equation (3.1) can then be rewritten, leading to the system of coupled integral equations of the form

$$\frac{d\overline{\mathbf{U}}}{dt} = -\frac{1}{V}\oint_{\Omega(t)} \vec{n}\cdot\vec{\mathbf{F}}\,d\Omega \;+\; \overline{\mathbf{S}}\,. \tag{3.4}$$

For a three-dimensional discrete domain and a computational cell (i,j,k) with N_f faces, contained within structured, multi-block, body-fitted mesh, the above equation can be re-written as

$$\frac{d\overline{\mathbf{U}}_{i,j,k}}{dt} = -\frac{1}{V_{i,j,k}}\sum_{l=1}^{N_\mathrm{f}}\Big[\vec{n}_l\cdot\vec{\mathbf{F}}_l A_l\Big]_{i,j,k} + \overline{\mathbf{S}}_{i,j,k}(\mathbf{U}) = \mathbf{R}_{i,j,k}(\mathbf{U})\,, \tag{3.5}$$

where A_l is the surface area of face l, and $\mathbf{R}$ is the residual vector. This semi-discrete form as given in Equation (3.5) above represents a set of coupled non-linear ordinary differential equations for the time evolution of the cell-averaged quantities, $\overline{\mathbf{U}}_{i,j,k}$. Since this is a set of ordinary differential equations it can be solved by an appropriate choice of a time marching (temporal integration) procedure.

3.2 Upwind-Based Finite-Volume Methods

The type of finite-volume scheme used in the present work is inspired by the classic work of Godunov [131], which introduced the finite-volume method for non-linear systems of hyperbolic conservation laws. In this method, the solution domain is discretized into control volumes (computational cells) as described above in which the integral form of the conservation laws are

going to be applied. The conservation laws are written for the cell-averaged values of the solution variables, $\overline{\mathbf{U}}$. The four basic elements constituting a Godunov-type finite-volume scheme [21] are the solution reconstruction within the cell, the flux evaluation at the cell boundaries, the averaging of the source vector within the cell volume and finally the time marching that will allow the evolution of the solution in time. Each of these four components will be discussed in turn in more detail in this chapter.

3.2.1 Reconstruction

As said previously, in the finite-volume scheme the conservation equations are solved for the cell averaged values of the conserved variables, $\overline{\mathbf{U}}$. The actual spatial distributions of variables defining $\mathbf{U}(x, y, z)$ within the cell are not known and some form of spatial representation must be assumed. Usually, a set of basis functions is adopted (exponential, sinusoidal, polynomial as is the case here) and the actual coefficients of the functions are retrieved by a function fitting procedure, which can be exactly determined or overdetermined. The accuracy of the reconstruction is crucial, because it directly impacts the spatial order of accuracy of the finite-volume scheme. Having a reconstructed representation of the solution allows for the evaluation of the solution at any point in space within a given cell. This step is an important part of the evaluation of fluxes at the interface between two cells, and a detailed description of the proposed high-order CENO reconstruction technique used here is given in Section 3.4.3, since it is a core element of the present thesis.

3.2.2 Evaluation of Fluxes at Cell Interface

By adopting standard Gaussian quadrature rules for the numerical integration at the face fluxes and volume sources associated with each computational cell, the semi-discrete form of Equation (3.5) for cell (i, j, k) can be re-expressed as

$$\frac{\mathrm{d}\overline{\mathbf{U}}_{i,j,k}}{\mathrm{d}t} = -\frac{1}{V_{i,j,k}} \sum_{l=1}^{N_f} \sum_{m=1}^{N_{GF}} \left(\omega_m \left(\vec{\mathbf{F}}^{\mathrm{I}} - \vec{\mathbf{F}}^{\mathrm{V}} \right) \cdot \overrightarrow{n} A_l \right)_{i,j,k,l,m} + \sum_{n=1}^{N_{GV}} \left(\omega_n \mathbf{S} \right)_{i,j,k,n} = \mathbf{R}_{i,j,k} \left(\overline{\mathbf{U}} \right), \quad (3.6)$$

where ω_m are the face quadrature weighting coefficients, ω_n are the volumetric quadrature weighting coefficients, A_l denotes the surface area of face l, and $\mathbf{R}_{i,j,k}$ is the residual operator. The normal unit vector $\overrightarrow{n}$ points outward a given face and is the direction where the flux is projected. In the most general case of non-planar element faces, the normals at each quadrature point are not necessarily parallel and therefore not the same. Each face of a given cell is shared with a neighbouring cell. As the reconstructions are derived for each cell independently, the two

cells sharing an interface may therefore not necessarily have matching values of the reconstructed solution. In the most general case, discontinuities are expected at the interface and appropriate methods to evaluate the inviscid and viscous fluxes at a quadrature point based on the possibly discontinuous left and right reconstructed values are required.

For the inviscid for hyperbolic fluxes, a similarity variable, $\eta = x/t$ can be defined where x is the distance in the direction normal to the face and t is the time, so that $\eta = 0$ represents a position located at the interface. The inviscid flux is a function of η and the left and right[1] state at the interface, so that the solution of the inviscid fluxes based on the solution of a Riemann problem can be written as

$$\vec{\mathbf{F}}^{\mathrm{I}} \cdot \overrightarrow{n} = \vec{\mathbf{F}}^{\mathrm{I}}(\mathbf{U}_{left}, \mathbf{U}_{right}, \overrightarrow{n}, \eta = 0) . \tag{3.7}$$

The evaluation of the inviscid fluxes is then based on the solution of a Riemann problem, which will be discussed in more detail in the following subsection.

For the viscous elliptic fluxes, there is the additional dependency on the gradient of the solution at the quadrature points

$$\vec{\mathbf{F}}^{\mathrm{V}} \cdot \overrightarrow{n} = \vec{\mathbf{F}}^{\mathrm{V}}(\mathbf{U}_{left}, \nabla\mathbf{U}_{left}, \mathbf{U}_{right}, \nabla\mathbf{U}_{right}, \overrightarrow{n}, \eta = 0) . \tag{3.8}$$

It is worth highlighting that the fluxes on a given surface have to be calculated at each quadrature point in the direction $\overrightarrow{n}$, normal to the face at that point.

A Brief Discussion on the Riemann Problem

The Riemann problem appears naturally in the finite-volume discretization and constitutes an important building block in the solution process described here. The Riemann problem deals with the solution of hyperbolic conservation laws in the presence of discontinuous piecewise constant data. The understanding and solution of the Riemann problem is very useful in the solution of the hyperbolic fluxes appearing in partial differential equations. Without loss of generality, assuming a one-dimensional non-stationary flow, the Riemann initial value problem can be characterized by the following initial data:

$$\mathbf{U}_{\circ}(x) = \mathbf{U}(x, t = 0) = \begin{cases} \mathbf{U}_{left} & \text{if } x \leq 0, \\ \mathbf{U}_{right} & \text{if } x > 0. \end{cases} \qquad \text{for } -\infty \leq x \leq \infty \tag{3.9}$$

[1] For simplicity of notation and without loss of generality, we may refer to any two cells sharing any given face as the **left** and **right** cells despite their actual relative positioning in the geometry (*e.g.* top/bottom, north/south, *etc.*)

Equation (3.9) indicates that, at the initial time, the data consists of two solution values separated by a discontinuity at x=0. As time progresses, the discontinuity between these two states will evolve into moving waves (rarefaction or shock) separated by a contact surface. As summarized by Gottlieb and Groth [132] for a polytropic gas, the solution of the Riemann problem involves determining the type of waves, their strengths, and the flow properties in each region between the waves and the contact surface, all dependent on the initial values of $\mathbf{U}_{left}$, $\mathbf{U}_{right}$, the position x and the time, t.

Approximate Riemann Solvers

For the Euler equations of an ideal polytropic gas, the solution of the Riemann problem can be determined exactly via an iterative numerical procedure like the one devised and discussed by Gottlieb and Groth [132]. In general, in finite-volume applications, approximate Riemann solvers are used, mostly because they provide sufficient accuracy allied to the ability of being easily extendable to more complex systems of partial differential equations, such as the filtered LES equations with tabulated chemistry of interest here. Several different approximate Riemann solvers have been developed since the pioneering work of Roe [133]. Among some of the more popular options are the HLL [134] and its later modifications, the HLLE flux function [135] and the Linde flux function[136]. In the present work, the approximate solver of Liou [137] is used. This approximate Riemann solver has been recognized to work well for a wide range of Mach numbers, making it attractive for reactive flows, such as those of interest here.

AUSM$^+$-up Flux Function

In this section, a brief description of the Advection Upstream Splitting Method (AUSM) modification of Liou [137], or so called AUSM$^+$-up approximate Riemann solver, is provided, as this approximate Riemann solver is applied in this particular work. For the LES of reactive flows using PCM-FPI the one-dimensional inviscid fluxes in the x-direction normal to the face can be written as being composed by a convective contribution and a pressure contribution and written

as [69]

$$\mathbf{F} = \mathbf{F}_{\mathrm{c}} + \mathbf{P} = \dot{m}\boldsymbol{\psi} + \mathbf{P} = \bar{\rho}\tilde{u} \begin{bmatrix} 1 \\ \tilde{u} \\ \tilde{v} \\ \tilde{w} \\ \tilde{H} \\ k_{\Delta} \\ \tilde{Y}_{\mathrm{c}} \\ \tilde{Y}_{\mathrm{c_v}} \\ \tilde{Y}_1 \\ \vdots \\ \tilde{Y}_N \end{bmatrix} + \begin{bmatrix} 0 \\ \breve{p} \\ 0 \\ 0 \\ 0 \\ 0 \\ 0 \\ 0 \\ 0 \\ \vdots \\ 0 \end{bmatrix}, \tag{3.10}$$

where $\tilde{H}$ is the total Favre-filtered enthalpy ($\tilde{H} = \tilde{E} + \bar{p}/\bar{\rho}$) and $\breve{p}$ is a modified pressure given by $\breve{p} = \bar{p} + \bar{\rho}k_{\Delta}$. At the cell interface, the flux, $\mathbf{F}_{1/2}$, can be expressed in terms of the mass flux $\dot{m} = \bar{\rho}\tilde{u}$ and the vector of convected quantities, $\boldsymbol{\psi} = [1, \tilde{u}, \tilde{v}, \tilde{w}, \tilde{H}, k_{\Delta}, \tilde{Y}_{\mathrm{c}}, \tilde{Y}_{\mathrm{c_v}}, \tilde{Y}_1, \ldots, \tilde{Y}_N]^{\mathrm{T}}$, as

$$\mathbf{F}_{1/2} = \dot{m}_{1/2}\boldsymbol{\psi}_{\mathrm{L/R}} + \mathbf{P}_{1/2}\,, \tag{3.11}$$

where $\boldsymbol{\psi}_{\mathrm{L}}$ and $\boldsymbol{\psi}_{\mathrm{R}}$ are the left or right vector of convected quantities, calculated in an upwind fashion as

$$\boldsymbol{\psi}_{\mathrm{L/R}} = \begin{cases} \boldsymbol{\psi}_{\mathrm{L}}, & \text{if } \dot{m}_{1/2} > 0\,, \\ \boldsymbol{\psi}_{\mathrm{R}}, & \text{otherwise}\,. \end{cases} \tag{3.12}$$

A crucial step for the computation of the convective interface flux is the determination of the mass fluxes, $\dot{m}$, at each cell interface as given by

$$\dot{m}_{1/2} = u_{1/2}\rho_{\mathrm{L/R}} = a_{1/2}M_{1/2} \begin{cases} \rho_{\mathrm{L}}, & \text{if } u_{1/2} > 0\,, \\ \rho_{\mathrm{R}}, & \text{otherwise}\,, \end{cases} \tag{3.13}$$

where the index $1/2$ refers to the variables evaluated at the interface and $\rho_{\mathrm{L/R}}$ is the left or right density convected by $u_{1/2}$. In order to calculate the interface flux, an interface Mach number is required. The interface Mach number is given in terms of the flow Mach number in the left and right neighbour cells, M_{L} and M_{R}. The details of these computations will be avoided here for brevity and the interested reader can refer to the original work of Liou [137] for a complete description.

To complete the numerical flux prescription, the pressure contribution to the interface inviscid

flux is given by

$$p_{1/2} = \mathfrak{P}^{+}_{(n)}(M_{\mathrm{L}})p_{\mathrm{L}} + \mathfrak{P}^{-}_{(n)}(M_{\mathrm{R}})p_{\mathrm{R}} + p_{\mathrm{u}}\,, \tag{3.14}$$

where $\mathfrak{P}^{\pm}$ are polynomial expansions and p_{u} is a velocity diffusion term, for which the computation details are also given in Liou [137].

Monotonicity and Godunov's Theorem

When developing a numerical scheme aiming at high-order accuracy for hyperbolic PDFs, one unavoidable side effect is the need to deal with the appearance of unphysical oscillations. The attempt to use a high-order description in regions in the vicinity of large gradients creates such oscillations. The large gradient regions are difficult to resolve and can lead to under-resolved solution or are a consequence of physical discontinuities, like shocks. The magnitude of the oscillations are typically a function of the size of the solution jump [138] and is also dependent on the actual order of the approximation. These oscillations are also referred to as *Gibbs phenomenon*, after the early studies by the mathematician Willard Gibbs pertaining to Fourier series [139]. The oscillations are undesirable because they can lead to robustness issues if unphysical solution values are generated, as, for example, negative densities, pressures or species mass fractions for reactive flows.

The original first-order Godunov scheme relies on a piecewise constant reconstruction within a given cell. A natural step towards a second-order scheme is to change the reconstruction function to a piecewise-linear, so that variables within a cell are represented by a linear polynomial. Godunov investigated the issue of monotonocity in schemes with orders higher than first for hyperbolic equations. His key finding is actually a theorem, named after him, the Godunov theorem, which states that there are no schemes which are both second-order accurate and monotonicity preserving for the class of constant coefficient schemes applied to hyperbolic equations [131]. An immediate consequence of this is that linear monotonicity preserving schemes based on constant coefficients are at most first order accurate [140]. A discussion of the implications of this theorem to high-order schemes is given in Section 3.4, where the high-order CENO scheme considered here is fully described.

Monotonicity Enforcement

The way around Godunov's theorem is the adoption of non-linear schemes to enforce monotonicity. Slope limiters, along with flux limiters are the usual strategy adopted in finite-volume schemes in order to preserve solution monotonicity in schemes with order higher than first. Several different types of limiters have been developed and the reader interested in a more formal,

theoretical review may refer to Toro [140]. Originally developed for regular grids the use of slope limiters on irregular grids has also been widely considered and is reviewed by Berger *et al.* [141].

In the case of piecewise linear reconstruction polynomials, the slope can be directly limited by a factor ψ_i, the *slope limiter*. Assuming a linear reconstruction polynomial in the one-dimensional case, for cell i, and a vector of solution variables $\mathbf{U}$, a vector $\boldsymbol{\psi_i}$ containing the slope limiters ψ_i for each solution variable can be defined, acting in the reconstruction of each respective solution variable as

$$\mathbf{U}_i(x) = \overline{\mathbf{U}}_i + \boldsymbol{\psi_i} : \frac{\partial \mathbf{U}}{\partial x}\Big|_i (x - x_i) \,, \tag{3.15}$$

where, if $\psi_i = 0$, the reconstruction polynomial reverts to the piecewise constant reconstruction and if $\psi_i = 1$, the reconstruction corresponds to the unlimited piecewise linear reconstruction for a given solution variable. The symbol : represents a term by term multiplication of two vectors. Different limiters work in a similar fashion in that they act comparing the reconstructed values at the quadrature points of a given cell with the average values in neighbouring cells. In the present work, the popular Barth-Jespersen limiter [142] was selected.

Barth-Jespersen Limiter The value of the limiter, ψ_i, for the Barth-Jespersen limiter is defined as follows:

$$\psi_i = \min(\psi_{i,m}) \,, \tag{3.16}$$

where

$$\psi_{i,m}(r_m) = \begin{cases} 1 & \text{for } (u_m - \overline{u}) = 0 \,, \\ \\ \min(1, r_m) & \text{for } (u_m - \overline{u}) \neq 0 \,. \end{cases} \tag{3.17}$$

The index m is used here to denote the quadrature points where the function is evaluated. Also, as seen in the above equation, the limiter is a function of the solution change ratio, r_m, defined for this particular limiter as

$$r_m = \begin{cases} \dfrac{u_{max} - \overline{u}}{u_m - \overline{u}} & \text{for } (u_m - \overline{u}) > 0 \,, \\ \\ \dfrac{u_{min} - \overline{u}}{u_m - \overline{u}} & \text{for } (u_m - \overline{u}) < 0 \,. \end{cases} \tag{3.18}$$

where u is the primitive solution variable of interest and $\overline{u}$ is its average value for the cell, i, being reconstructed. The variables u_{max} and u_{min} are respectively the maximum and minimum values of u found amongst all cells used in the reconstruction of cell i, and u_m is the unlimited reconstructed value at the m^{th} quadrature point.

One drawback of slope limiters is that, because they usually preform well in preserving the monotonicity of the solution in sharp gradients regions, they can not distinguish between a sharp discontinuity and local smooth extrema. This leads to the problem of clipping of smooth extrema. In the particular high-order scheme applied here, smooth extrema are detected before the application of the limiters and this problem is therefore avoided. More details about this feature of the proposed CENO scheme are given in Section 3.4

3.3 Spatial Meshes - Types of Elements

Although the finite-volume method does not restrict the shape of the element, the appropriate choice of a particular element type should take note of the ability to perform some required operations on the chosen element, and the cost related to these operations. Some of these required operations include the unambiguous location of a point on the element surface and the calculation of the face normal at that point, the integral of a function over a cell face and the calculation of the integral of a function over the cell volume. Derived from these basic operations are the calculation of faces areas, of the cell volume, location of the cell centroid, and the location of flux calculation points on the surface. These basic operations at the cell level are the building blocks of the integration procedure for the conservation equations in any finite-volume method.

Mesh generation is the process of subdividing the flow domain in cells (small control volume units). The mesh generation is a tessellation using nodes properly distributed inside the problem domain which are grouped to form the elementary units, cells, usually with a predefined shape. Polyhedral elements are, in general, a very usual option for the cell shape in finite-volume methods.

In any type of spatial discretization it is necessary to identify the neighbours of a given cell. In structured cells the identification of the neighbours of a cell is directly given by knowing that particular cell's index (i,j,k) in the three directions (x,y,z). For example, a given cell, C_{ijk}, in a structured mesh has the neighbours, $C_{i-1,j,k}$ and $C_{i+1,j,k}$ in the $x-$direction. By analogy the neighbours in $y-$ and $z-$directions can also be identified. In the case of unstructured meshes, an indexing system based on the three-dimensional axis is not generally possible. In order to be able to map the neighbours of a given cell in an unstructured mesh, it is necessary to generate a *connectivity matrix*, identifying the elements sharing a face with that cell.

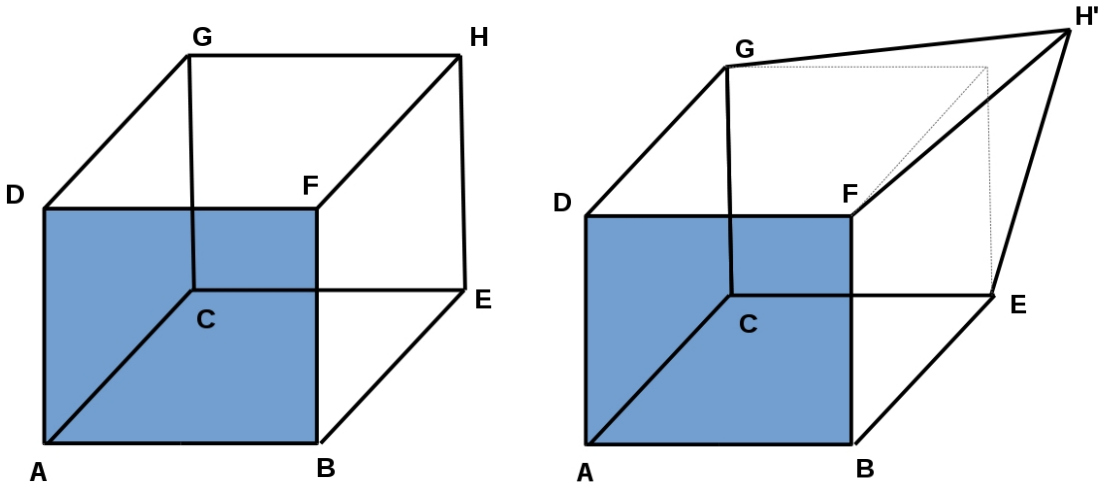

(a) Regular Hexahedron (b) Generic Hexahedron

Figure 3.1: Regular hexahedron (planar faces) and generic hexahedron (node H' is moved out of BEF plane)

3.3.1 Multiblock Body-Fitted Hexahedral Mesh

In the present work, a generalization of the term *hexahedron* will be used to describe the elements of interest here, which also have 6 external faces, although these faces may not necessarily be planar (as is formally expected in the mathematical definition of hexahedron). Each hexahedral element is actually described by specifying 8 nodes (A,B,C,D,E,F,G and H) in physical space. These 8 nodes can be grouped in groups of 4 (four) composing an external face (a surface that does not contain any interior point). The nodes defining each face surface may or may not be co-planar as the case may be.

Having some flexibility on where to place the nodes used in the tessellation process is desired in order to be able to deal with more complex geometries and flow topologies. In the case of a body-fitted mesh, like the ones considered here, the boundary nodes placement is restricted to the geometry. This constraint suggests that a description consisting of only regular elements (cubes) may not be sufficient to describe the geometry properly. This is one reason why the generic hexahedron considered here became attractive, as they do not require all the nodes on a face to be co-planar. A schematic diagram illustrating a generic hexahedron is given in Figure 3.1(b), emphasizing the presence of non-planar faces. In the multiblock approach adopted here, the solution domain is partitioned into several smaller blocks, each of them containing the same total number of hexahedral elements. These blocks can be distributed out to multiple processors making parallelization and load balance relatively straightforward, as will be described later in the chapter. In the next sections, different strategies to operate on the hexahedral elements in

the context of the finite-volume scheme considered here are described, with particular emphasis given to the trilinear transformation approach, which was the method of choice in this work.

3.3.2 Cartesian Hexahedron

A Cartesian hexahedron will be defined here as the hexahedron where all 6 faces are planar and rectangular. This category includes the particular case of the cube element, which has all 6 faces as perfect squares forming a cube. The Cartesian hexahedron is the most trivial case to deal with and due to its regularity, many of the mathematical operations mentioned above become greatly simplified in this case. Areas and volume can be computed explicitly from simple geometric relations. Simple one-point quadrature rules provide second-order accuracy by using the face centroid or volume centroid as quadrature point. These points can be straightforwardly calculated as the face diagonal and rectangle diagonal midpoints. For a higher-order discretization the placement of the quadrature points is easily found for each edge by scaling the canonical distribution of quadrature points found in an unitary cube (a cube where all edge lengths are unity). Face normals are directly given by the direction of the edge orthogonal to the face. However, one obvious problem with Cartesian elements is that they significantly limit the complexity of the geometries that can be properly represented in a simulation. Either the geometries have to be simplified, or strategies like cut-cell methods [143] and immersed boundaries must be used. Despite some notable benefits regarding the ability to mesh complex shapes, one important disadvantage of the immersed boundary methods is that imposing the boundary conditions is not straightforward and, the effects of the boundary treatment on the accuracy and conservation properties of the numerical scheme are not obvious [144].

3.3.3 Triangulation Approach

One of the simplest approaches to operating with generic hexahedral elements, which may have non-planar surfaces, is the subdivision of the cell faces into triangles and the cell volume into tetrahedral elements [2]. One possible triangulation requires that each of the 6 faces of the hexahedral would be subdivided in 4 triangles, each triangle on a face would then be associated with 4 tetrahedra, totaling 24 tetrahedra. All the tetrahedra share a common vertex, the cell centroid. Alternatively, a hexahedron can also be divided into 6 tetrahedra by subdividing each face into 2 triangles. The triangulation approach has the advantage of providing an easy way to compute the volume and face areas but, in the case of non-planar faces it leads to a discontinuity in the face description (faceted surface). This discontinuity may pose extra difficulties in the application of adaptive mesh refinement (AMR). Also, in the case of the face integrations, the integral has to be evaluated by parts for each triangle, requiring a minimum

number of quadrature points per triangle in order to guarantee the proper accuracy. For high-order discretizations, assuming 3 points are required per triangular face of a tetrahedron for fourth-order accuracy, and if we use only 2 triangles per face (6 tetrahedra per hexahedron), the total number of quadrature points required for one hexahedron face would be 6. This is more than what is needed for the approach adopted herein, the trilinear transformation method, where a continuous description of the faces of the hexahedron allows for the use of just 4 quadrature points to achieve fourth-order accuracy.

3.3.4 Trilinear Transformation

The trilinear transformation method [145] maps a hexahedron from physical space into a reference unitary cube in canonical space. From a numerical implementation perspective the discretization of the domain in hexahedra is made by defining the eight vertices of each hexahedron. Each face of the hexahedron has 4 vertices which are connected by 4 straight edges. These 4 edges define a bounded surface in $\mathcal{R}^3$ space which may or may not be planar. Therefore, some rule (function) to describe the position in space of the internal points pertaining to a face is required. It is important to note that, for interior cells, the shape of this function is actually not relevant, the only requirement being that the same shape can be determined from the information contained in each of the neighbouring cells sharing that face. In the present work, a trilinear function is adopted to describe a (x,y,z) point in the hexahedron volume or on its surface.

The trilinear function is a trivariate polynomial, linear in each of its three variable (p,q,r). Having such an algebraic description of the hexahedron volume and its surfaces allows for an easy and robust way of deriving important geometric properties of the cell. Considering two neighbouring cells, C_i and C_{i+1}, sharing a face, $F_{i+1/2}$, one of the main advantages of this approach is the ability to provide a robust and consistent way of defining the proper placement of flux evaluation points and direction of the unit normal vectors over the face $F_{i+1/2}$, without any ambiguity, for both cells (C_i and C_{i+1}).

Considering a hexahedral cell, C, in the physical space of the problem (x,y,z), a trilinear mapping, $\vec{r}$, exists such that the hexahedral cell C is the image of a regular reference hexahedron, $\hat{C}$, in a reference domain. The reference cell, $\hat{C}$, consists of a unit cube with unitary length edges and fixed vertices (p,q,r) = (0, 0, 0), (1, 0, 0), (0, 1, 0), (0, 0, 1), (1, 1, 0), (1, 0, 1), (0, 1, 1) and (1, 1, 1). The trilinear mapping can then be written as

$$\vec{r}(p,q,r) = \vec{A} + \vec{B}p + \vec{C}q + \vec{D}r + \vec{E}pq + \vec{F}pr + \vec{G}qr + \vec{H}pqr\,, \tag{3.19}$$

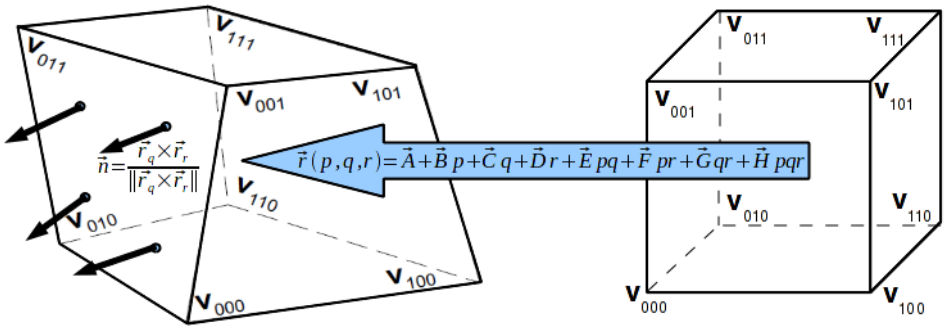

Figure 3.2: A general hexahedral cell in physical space mapped into a reference cube by applying a trilinear transformation $(x, y, z) = \vec{r}(p, q, r)$, as appearing in [2]

where p, q and r are the regular Cartesian coordinates in the canonical space of the reference cube and $\vec{A}$, $\vec{B}$, $\vec{C}$, $\vec{D}$, $\vec{E}$, $\vec{F}$, $\vec{G}$ and $\vec{H}$ are the transformation vector coefficients that are computed by imposing the one-to-one correspondence between the vertices of the hexahedron and those of the reference cube. These transformation vectors are defined based on the nodes in physical space and are given by [145]

$$\vec{A} = v_{000};$$

$$\vec{B} = v_{100} - \vec{A};$$

$$\vec{C} = v_{010} - \vec{A};$$

$$\vec{D} = v_{001} - \vec{A};$$

$$\vec{E} = v_{110} - \vec{A} - \vec{B} - \vec{C};$$

$$\vec{F} = v_{101} - \vec{A} - \vec{B} - \vec{D};$$

$$\vec{G} = v_{011} - \vec{A} - \vec{C} - \vec{D};$$

$$\vec{H} = v_{111} - \vec{A} - \vec{B} - \vec{C} - \vec{D} - \vec{E} - \vec{F} - \vec{G}\,,$$

where v_{ijk} are the vertices of the reference cube.

Face and Volume Integrations using the Trilinear Transformation

Covariant vectors can be defined for the preceding trilinear transformation as

$$\vec{r}_p = \frac{\partial \vec{r}}{\partial p}, \vec{r}_q = \frac{\partial \vec{r}}{\partial q}, \vec{r}_r = \frac{\partial \vec{r}}{\partial r}$$

so that the determinant of the volumetric Jacobian, $\det \mathbf{J}$, for the transformation from $\hat{C}$ to C is then given by

$$\det \mathbf{J} \equiv \left| \frac{\partial \vec{r}}{\partial (p,q,r)} \right| = \vec{r}_p(q,r) \cdot (\vec{r}_q(p,r) \times \vec{r}_q(p,q)) \,. \tag{3.20}$$

It is interesting to note that the transformation derivatives with respect to each direction are only a function of the other two directions, a direct consequence of the linear character of the assumed transformation.

For a face whose normal is parallel to any one of the three reference directions (p,q or r), a surface Jacobian, $\mathrm{J_F}$, can be defined as the cross product between the other two directions, the directions that actually map that particular surface:

$$\mathrm{J_{F}}_p = |(\vec{r}_q(p,r) \times \vec{r}_r(p,q))| \tag{3.21}$$

$$\mathrm{J_{F}}_q = |(\vec{r}_r(p,q) \times \vec{r}_p(q,r))| \tag{3.22}$$

$$\mathrm{J_{F}}_r = |(\vec{r}_p(q,r) \times \vec{r}_q(p,r))| \tag{3.23}$$

Once the transformation coefficients are determined, any local or integrated quantities involving the geometry of the hexahedron (e.g., centroid, volume, face normals, volumetric or face integrals of arbitrary functions, etc.) can be computed by carrying out the required evaluations within the reference cube [146, 147]. For example, to evaluate a volumetric integral of a continuous smooth function, $g(\vec{X})$, over a control volume $\mathcal{V}_{ijk}$, $\mathcal{I} = \iiint_{\mathcal{V}_{ijk}} g(\vec{X}) \mathrm{dv}$, the variables and integration domain are changed to those of the reference unit cube by the trilinear transformation, $\vec{X} = \vec{r}(p,q,r)$, and the determinant of the Jacobian of the transformation, $\det \mathbf{J} \equiv \left| \frac{\partial (x,y,z)}{\partial (p,q,r)} \right|$. Thus, the volumetric integral, $\mathcal{I}$, in the physical space (x,y,z), is calculated as function of the coordinates in the canonical space (p,q,r) and can be written as

$$\mathcal{I} = \int_0^1 \int_0^1 \int_0^1 g(\vec{r}(p,q,r)) \det \mathbf{J} \, \mathrm{d}p \, \mathrm{d}q \, \mathrm{d}r \tag{3.24}$$

where the Jacobian, $\det \mathbf{J}$, is clearly a function of the location (p,q,r).

The triple integral of Equation (3.24) is evaluated numerically by applying Gauss-Legendre quadrature integration rules for the specified level of accuracy. For a quadrature rule with N_{GV}

volumetric Gauss points, $\mathcal{I}$ in Equation (3.24) is approximated as

$$\mathcal{I} \simeq \sum_{n=1}^{N_{GV}} g\left(\vec{r}(p,q,r)\right)\,(\det \mathbf{J})_n\,\omega_n = \sum_{n=1}^{N_{GV}} g(\vec{X}_n)\,\tilde{\omega}_n \tag{3.25}$$

where $\vec{X}_n = \vec{r}(p_n, q_n, r_n)$ and $\tilde{\omega}_n = (\det \mathbf{J})_n\,\omega_n$ represent the Gauss-Legendre abscissa and weight in the physical space. Note that the abscissa $\vec{X}_n$ is the trilinear transformation image of the abscissa (p_n, q_n, r_n) in the reference unit cube and the weight $\tilde{\omega}_n$ is determined as the product between the local Jacobian and the corresponding Gaussian weight coefficient ω_n. The volumetric weights ω_n at a given point (p, q, r) in Cartesian coordinates are given by the tensor product of the one-dimensional Gauss-Legendre weights in each direction. Note also that $\left(\vec{X}_n, \tilde{\omega}_n\right)$ depend only on the hexahedral cell geometry. In this work, we opt to store and reuse $\left(\vec{X}_n, \tilde{\omega}_n\right)$ for a given cell for volumetric integrations involving different $g(\vec{X})$ functions (e.g., calculation of volume, centroid, geometric moments etc.).

An analogous approach is followed for the integration of variables over a hexahedron face. The surface integral of a given function $g(\vec{X})$ over a surface, $\mathcal{S}_{ijk}$, $\mathcal{I}_S = \iint_{\mathcal{S}_{ijk}} g(\vec{X})\mathrm{dA}$. The variables and integration domain are again changed to those of the reference unit cube by the trilinear transformation, $\vec{X} = \vec{r}(p, q, r)$. Now, for a given face, one of the coordinates p,q, or r will be held constant. Let us assume, for example, that the face being considered is the face $r = 1$. In order to take into account the effect of the transformation, the face-Jacobian of the transformation at the given face is considered. Thus, the surface integral, $\mathcal{I}_S$, in the physical space (x, y, z), is calculated as function of the coordinates in the canonical space $(p, q, 1)$ as

$$\mathcal{I}_S = \int_0^1 \int_0^1 g(\vec{r}(p,q,1))\mathrm{J}_{\mathrm{F}r}\,\mathrm{d}p\,\mathrm{d}q\,, \tag{3.26}$$

where the Jacobian, $\mathrm{J}_{\mathrm{F}r}$, is clearly a function of the location $(p, q, 1)$.

The double integral of Equation (3.26) is evaluated numerically by applying the Gauss-Legendre quadrature integration rules for the specified level of accuracy. For a quadrature rule with N_{GF} surface Gauss points, $\mathcal{I}_S$ in Equation (3.26) is approximated as

$$\mathcal{I}_S \simeq \sum_{m=1}^{N_{GF}} g\left(\vec{r}(p,q,1)\right)\,(\mathrm{J}_{\mathrm{F}r})_m\,\omega_m = \sum_{m=1}^{N_{GF}} g(\vec{X}_m)\,\tilde{\omega}_m \tag{3.27}$$

where $\vec{X}_m = \vec{r}(p_m, q_m, r_m)$ and $\tilde{\omega}_m = (\det \mathbf{J})_m\,\omega_m$ represent the Gauss-Legendre abscissa and weight in the physical space. Note that the abscissa, $\vec{X}_m$, is the trilinear transformation image

of the abscissa $(p_m, q_m, 1)$ in the reference unit cube and the weight, $\tilde{\omega}_m$, is determined as the product between the local face Jacobian and the corresponding Gaussian weight coefficient, ω_m. Similarly to what was done for the volumetric weights, the Gauss face weights, ω_m, at a given point, (p, q, r), in Cartesian coordinates are given by the tensor product of the one-dimensional Gauss-Legendre weights in each direction.

One important aspect to be considered in many numerical applications is the trade-off between quantities that can be stored and re-used (higher memory requirements, lower computational cost), and variables that should be calculated during the run (lower memory requirements, higher computational cost). In the particular case of the trilinear transformation, the choice was made here to store the transformation coefficients for each cell independent. The face quadrature points, the modified face quadrature weights, $\tilde{\omega}_m$, and face normals as well as the volumetric quadrature points locations and modified volumetric weights, $\tilde{\omega}_n$, are also stored. Face information is stored only for three faces (South, East and Bottom faces) for each cell, since their counterparts (North, West and Top faces) can be obtained from the stored values in the respective neighbouring cells.

3.4 High-Order CENO Scheme

In this section, details are given on how the basic elements of the finite-volume scheme, as presented in Section 3.2, are specialized for the high-order CENO scheme used in the present study. The high-order CENO spatial discretization considered in this work was originally developed by Ivan and Groth [148, 149, 17] for two-dimensional applications. It is a central scheme, since the stencils are built symmetrically around a fixed central cell of interest for all variables. It also attempts to achieve the properties of ENO schemes proposed by Harten *et al.* [16], hence the name "CENO" for Central-ENO.

The potential for the appearance of oscillatory behaviour is considered to be one of the major problems for higher-order schemes [140]. Oscillations associated with high-error discretizations are not only undesirable but can potentially lead to non-physical values for certain variables. This particular risk of generating non-physical values is easily seen when variables involved have a clear upper or lower limit, like density or turbulent kinetic energy, which by definition can not be negative. In reactive flow simulations, like in the present study, the normalized progress of reaction variable c, is bounded between 0 and 1, so any values below 0 or higher than 1 are also not physically acceptable. Solution monotonicity is therefore also a concern in this case

3.4.1 Essentially Non-Oscillatory Schemes

The concept of monotonocity of a numerical scheme was briefly presented in Section 3.2. A hierarchy can actually be identified in the classification of schemes related to how strict they are in the treatment of solution monotonicity . The most strict requirement is for the class of *Monotone schemes*, as first defined by Godunov [131], that have been shown to be at most first order. A monotone scheme is classified as a scheme in which a monotonically increasing solution remains monotonically increasing, or, a monotonically decreasing solution remains monotonically decreasing, for all time. The so called *Total-Variation-Diminishing (TVD)* schemes have a somewhat looser definition in the sense that now the total variation of the function is required to remain monotonic, but not necessarily the local variation [150, 151]. In other words, in monotone schemes the difference between any two adjacent cells always maintains its sign, while in TVD schemes this might not necessarily be the case for two adjacent cells, but has to be the case for the total sum of the differences in the domain (the total variation). All TVD schemes are, however, restricted to be at most second-order accuracy [138]. The next step in the classification is the idea of *Monotonicity Preserving* scheme, which require that the number of solution extrema be preserved in time and the local maximums (minimums) are non-increasing (non-decreasing). When moving to arbitrary high-order schemes more relaxed monotonicity criteria have to be considered and the concept of ENO schemes is established. The idea of the original ENO scheme, as first developed by Harten *et al.* [16], is to perform the reconstruction step using multiple stencils and compare how smooth the solution is for each stencil, selecting the smoothest stencil to enforce monotonicity. A scheme can be classified to be an ENO scheme when:

- the scheme has second or higher order of accuracy in smooth parts of the solution;
- the scheme produces numerical solutions free from spurious oscillations and,
- the scheme produces high-resolution of discontinuities. Actually, in the vicinity of smooth extrema, the ENO criteria allows the existence of spurious oscillations but the magnitude of these oscillations should diminish as the mesh is refined, respecting the order of the polynomial reconstruction used.

The development of Weighted ENO (WENO) schemes followed the ENO approach [18, 19, 20], and instead of choosing only the smoothest stencil, these techniques assign a weight to these multiple reconstruction stencils. These schemes typically become more computationally expensive and complex, particularly in higher dimensions. Following the developers of the CENO scheme, Ivan and Groth [148, 149, 17], the definition of ENO scheme adopted here is the same

used by Harten [138], where the author also explains that it is possible to create a ENO scheme that relies on a *fixed stencil* (instead of multiple stencils) and that uses a *hybrid reconstruction*. The CENO scheme utilized here has these two characteristics. It uses a fixed stencil combined with a hybrid reconstruction approach.

3.4.2 Properties of the CENO Scheme

The CENO scheme of Ivan and Groth [148, 149, 17] was successfully developed and has been previously applied to different sets of conservation equations. Beyond these initial developments, the CENO scheme has also been used for two-dimensional viscous flows [62] and for viscous, three-dimensional flows on Cartesian meshes [24]. It has also been applied to three-dimensional hyperbolic Magneto Hydrodynamics (MHD) problems [152, 153, 154]. The application of the CENO scheme to three-dimensional unstructured meshes using an incompressible formulation was previously considered by Charest *et al.* [63, 155]. In the present work, the scheme is extended for use to three-dimensional generic multi-block hexahedral meshes for the solution of the elliptic system of conservation equations governing the LES of turbulent reactive flows.

As is usually the case in engineering work, advantages and disadvantages of a particular design decision or methodology selection have to be weighed and it is no different when selecting a numerical method to solve partial differential equations. The proposed CENO scheme has some very desirable properties in comparison with other methods, but these advantages and properties can come at a cost, which is also recognized here. In the sections to follow these advantages and disadvantages are briefly discussed.

Advantages of the CENO Scheme

The CENO scheme presents several advantages which are the main motivation for its continued use and development. One of the most important advantages, which is considered one of the main challenges in the application of high-order schemes is the ability of the scheme to eliminate spurious oscillations that may occur near solution discontinuities, either as a consequence of a physically discontinuous solution or as a consequence of a localized under-resolution of the solution. The CENO scheme is able to deal with the spurious oscillations while still being capable of capturing solution extrema in smooth regions with high-order accuracy. The strategy to deal with these two conflicting goals arises from the hybrid nature of the reconstruction and the use of the solution smoothness indicator. The details of the use of the smoothness indicator are discussed later in Section 3.4.5. The use of a robust smoothness indicator that can correctly identify regions that are under-resolved (i.e., too few cells or grid points) as well as discontinuities, provides another strength of the high-order CENO scheme, which is its suitability

for coupling with AMR strategies. The criteria for determining whether or not to apply mesh refinement follows naturally from the solution procedure, without added cost or testing, since the smoothness indicator is calculated anyway for the reconstruction step of the finite-volume method. The two-dimensional application of the CENO scheme with adaptive mesh refinement has been successfully demonstrated by Ivan and Groth [149, 17].

Another very important advantage of the scheme is the use of a fixed central stencil, the same for all cells and for all solution variables. Central stencils are acknowledged as being able to provide the most accurate reconstructions when compared to biased stencils of the same size [156]. Avoiding the requirement for multiple stencils significantly simplifies the reconstruction procedure and thus avoids some of the typical complexities of other ENO [16], and particularly WENO [18] schemes. Depending on what type of boundary conditions are used and the particular treatment of these boundary conditions, it may be required to use specific stencils at the boundary, nevertheless the CENO scheme implementation is flexible enough to support this type of local requirement while keeping most of the general reconstruction procedure universal to all cells. Basically, only a proper neighbour cell flagging procedure is required and the same reconstruction technique can be applied at the boundary, as in all the remaining internal cells.

The versatility of the design of the scheme and particularly the generality of its current implementation are also among its key strengths, allowing straightforward extension to other sets of variables and PDEs and different mesh types, including general unstructured meshes. Note that the versatility of the CENO scheme in fact arises from the use of the K-exact reconstruction of Barth [21], which is directly applicable to multiple dimensions and is also directly applicable to unstructured grids. It should be mentioned that this ability of combining the CENO scheme with unstructured meshes has been recently demonstrated by McDonald *et al.* [157] and by Charest *et al.* [63] using an incompressible flow formulation.

Finally, the CENO scheme also allows a very flexible implementation in the sense that it is very easy to switch orders of accuracy, potentially allowing the future exploration of local order refinement, providing a framework that can efficiently consider a solution method with varying levels of accuracy in a robust way.

Disadvantages of the CENO Scheme

As a consequence of pursuing the previously mentioned advantageous features, the CENO scheme also presents some limitations. In order to determine if the solution in the various regions of the domain will be deemed under-resolved or discontinuous, it is necessary to calculate a smoothness indicator, which by itself has an implicit computational cost. While possibly

not entirely necessary, the need to perform a second reconstruction (the piecewise linear reconstruction if the smoothness indicator flags the solution in a particular region as under-resolved) also adds to the computational cost. Additionally, as a consequence of this hybrid nature of the reconstruction procedure, in which the order of the reconstruction may be forcefully reduced in order to deal with oscillations, uniform solution accuracy is formally not guaranteed, as in the ENO or WENO schemes. In the high-order CENO scheme, limited linear solution reconstruction regions can appear in the solution domain along with high-order solution from smoother regions. Another factor that is a general disadvantage of finite-volume schemes, and not just of the CENO scheme in particular, is that this scheme is not as compact a scheme, as other discretizations such as the DG methods. The idea of compactness is related to the origin of the information used to reconstruct the information in a given cell. If a scheme requires a large stencil, with reconstruction information coming from relatively distant neighbours it is said to be non-compact. In general, the case of parallel implementation of a scheme is directly related to compactness, with more compact schemes tending to lead to more efficient parallel implementation. Depending on the desired order of reconstruction and how the reconstruction stencil is built, the CENO scheme might require information from cells located two neighbours away from the reconstruction cell. DG schemes would typically only require information from nearest neighbours in the flux evaluation. This idea will be explored again later and will be made more clear after the discussion given in Section 3.4.4.

3.4.3 K-Exact Least-Squares Reconstruction

As was described in Section 3.2, where a typical finite-volume scheme was described, the solution values computed in each cell are the cell averaged values of each solution variables and these values are associated to the cell centroid. In a finite-volume framework, the need arises to determine the solution value at specific locations within the cell, usually at the cell faces and also within the cell volume to enable appropriate volumetric quadrature of values of interest. As will be seen in more detail in the sections to follow, for the lowest-order approximations (i.e. 0^{th}-order) the average solution value can be used to approximate solution values at any point in the cell. The smaller the cell, or, the higher the refinement, the more accurate the approximation becomes. However, in general for practical applications, this is not possible, since extremely refined meshes are not always feasible and the solution may therefore vary significantly within a single cell. Since information about the solution is required at different locations within the cell, the need arises to be able to interpolate/approximate (or *reconstruct*) the solution value at any given location within the cell. In a finite-volume setting, this is usually done by using the information available from the cell and its neighbours.

In the proposed CENO scheme, the K-exact least-squares reconstruction of Barth and Fredrickson [21, 22] is the selected strategy to reconstruct solution values within a given cell to high-accuracy. The K-exact reconstruction provides a K^{th}-order Taylor series expansion (polynomial) of a scalar solution variable, U, about the cell, C_{ijk}, center supported by the average value of U in that particular cell (U_{ijk}) as well as the average value of U on the neighbouring cells. The order of the polynomial reconstruction determines the spatial order of accuracy of the scheme [23]. The reconstruction procedure can be applied to either the conserved or the primitive solution variables. The current implementation is flexible enough to allow both alternatives with minimal changes to the original implementation. Nevertheless, here, it is chosen to reconstruct the primitive variables in order to be able to more easily enforce the positivity of solution variables such as pressure and species mass fractions.

The three-dimensional K^{th}-order Taylor series reconstruction polynomial can be expressed in a general, compact form as follows:

$$U_{ijk}^{K}(x,y,z) = \sum_{p_1=0}^{K} \sum_{p_2=0}^{K} \sum_{p_3=0}^{K} (x - x_{ijk})^{p_1} (y - y_{ijk})^{p_2} (z - z_{ijk})^{p_3} D_{p_1 p_2 p_3} + \mathcal{O}\left(\Delta^{K+1}\right) . \quad (3.28)$$

In Equation (3.28) above, U represents the variable (primitive or conserved) being reconstructed and K is the order of the reconstruction. The indices, ijk, are the indices in the x-, y-, and z-coordinate directions, which relate in the above expression to the particular cell, C_{ijk}, being reconstructed. The coordinates of the cell centroid of cell ijk are given by $x_{ijk}, y_{ijk}, z_{ijk}$. The variable, $U_{ijk}^{K}(x,y,z)$, represents the K-exact polynomial reconstruction of the variable, U, within C_{ijk} and the indices xyz emphasize the fact that $U_{ijk}^{K}(x,y,z)$ is a direct function of the spatial coordinates (x,y,z) within C_{ijk}. The additional support information required to determine the polynomial coefficients come from the neighbouring cells of cell C_{ijk}, identified by the indices pqr, which are the indices in the x-, y-, and z-coordinate directions for these neighbouring cells forming the reconstruction stencil of cell C_{ijk}. The different combinations of the summation indices p_1, p_2, p_3 produce each of the monomial terms composing the full polynomial and each of these monomials must always satisfy the condition $(p_1 + p_2 + p_3) \leq K$. This approximation is accurate to within an error of the order $\mathcal{O}\left(\Delta^{K+1}\right)$, where Δ is the size of the discretization element (i.e., computation cell).

In a three-dimensional Taylor series expansion, the spatial derivatives of U of varying order with respect to the spatial directions appear in each term comprising the full polynomial. In the Equation (3.28), these derivatives appear combined in the term, $D_{p_1 p_2 p_3}$, which become the constant coefficients of the Taylor series expansion in three dimensions. It is important to notice

that, when determining the reconstruction polynomial for each variable in each cell, the terms $D_{p_1p_2p_3}$ are the unknowns. These terms are the derivatives evaluated at the cell centroid location of cell ijk and they absorb the multiplier, $(1/n!)$, appearing in the Taylor series expansion.

Since the reconstruction function selected is a polynomial, it is assumed that polynomials of degree $N \leq K$ must be represented by the reconstruction exactly. In order to be able to recover the K-exact reconstruction polynomial coefficients, $D_{p_1p_2p_3}$, two major constraints are also imposed [17]:

1. The average value of U_{ijk}, in cell C_{ijk} must be preserved by the solution reconstruction U_{xyz}.

2. the reconstruction procedure must have compact support. This requirement will constrain the location of the neighbours being used to calculate the reconstruction polynomial.

These two constraints will support the process of building the over-determined linear system of equations whose solution is the unknown derivatives, $D_{p_1p_2p_3}$, as will be seen in the following sections.

3.4.4 Reconstruction Stencils

In the previous section, the reasoning and constraints observed in the process of determining the reconstruction polynomial coefficients, $D_{p_1p_2p_3}$, were presented. Clearly, the total number of unknown derivatives, N, will be a direct function of the order of the reconstruction, K. For three-dimensional meshes, the combinatorial relation between the number of derivatives (unknown coefficients of the reconstruction polynomial) and the order of the polynomial is

$$N = \frac{(K+1)(K+2)(K+3)}{6}\,. \tag{3.29}$$

By direct substitution of orders K from 0 to 4 in the above expression, the number of derivatives N=1, 4, 10, 20 and 35 are obtained for K=0,1,2,3 and 4 respectively. These values of N include the cell-centered value (the zero-derivative).

In order to be able to generate the polynomial description of the solution distribution (reconstruction) inside one cell, C_{ijk}, and calculate the N unknown coefficients, it is necessary to create a system of equations or conditions with at least N relations between those unknown coefficients using available information from the solution. The first constraint listed in Section 3.4.3, states that the cell average value for the cell being reconstructed (cell ijk) must be preserved by the

reconstruction, implying that

$$\overline{U}_{ijk} = \frac{1}{\mathcal{V}_{ijk}} \iiint_{\mathcal{V}_{ijk}} \left[U^K_{ijk}(x,y,z) \right] d\mathcal{V} \,. \tag{3.30}$$

Additional information comes from the application of the second constraint listed in Section 3.4.3. The polynomial reconstruction is a functional in three-dimensional space that represents the solution inside the cell, C_{ijk}. It is reasonable to assume that the smoother the solution the closer such a polynomial representation will be of the physical, exact solution. Therefore it is also assumed that, in such cases, this representation can be extended beyond the cell itself and applied to its neighbours. The neighbouring cells are indexed pqr according to the notation previously described. In this sense the unknown derivatives are then found by extending the representation in cell ijk to its neighbouring cells pqr. It is then taken that the average value obtained by integrating the reconstruction polynomial $U^K_{ijk}(x,y,z)$ of cell C_{ijk}, over a given neighbouring cell domain, C_{pqr}, should equal the known average solution value in that neighbouring cell, $\overline{U}_{pqr}$. By using an appropriate number of neighbours one might gather enough information to create a system of equations capable of providing the N derivatives required. The cells, C_{pqr}, used in the determination of C_{ijk} reconstruction polynomial make up the reconstruction stencil for cell C_{ijk}. Naturally, the minimum number of neighbours in the stencil would be $N-1$, by acknowledging that one extra equation comes from the cell being reconstructed itself. Nevertheless, it has been recognized [17] that it is beneficial to include a larger number of neighbouring cells than the minimum required. One of the advantages of such an overdetermined approach is that, in the case of stretched meshes and/or solution gradients that are not aligned with the mesh, the use of larger stencil should smoothen these potential effects of preferential directions coming from the solution. Using a larger reconstruction stencil leads to an overdetermined system of equations (more constraint equations than unknowns), which requires the use of a least-squares type of strategy to obtain the N solution coefficients, $D_{p_1p_2p_3}$.

Considering the selection of neighbours used in the stencil the third requirement of the K-exact reconstruction procedure comes in place. The requirement of "compact support" means that the neighbouring cells in the stencil should be geometrically near to the cell being reconstructed [158]. For the centered stencils and structured meshes of interest here, the number of neighbours is directly related to the number of layers of neighbouring cells that surround the reconstructed cell, C_{ijk}. The simplest strategy to achieve a desired number of neighbouring cells in a centered, structured strategy is to flag all the cells in the given layer as pertaining to the stencil. In this sense, one-layer of cells is enough for the $K=0-$, $1-$, and $2-$ reconstructions, since a one-layer, structured, centered stencil in three dimensions consists of 27 cells ($27 > N$ for $K=0$, 1, and 2).

This number is achieved by recognizing that in one direction, x for example, adding one layer means adding the right and left neighbours, $C_{i+1,jk}$ and $C_{i-1,jk}$, totalizing 3 cells per-direction, which in three directions equals to 3^3=27. For order $K=3$ one layer should be enough but in order to obtain a higher degree of over-determination of the system, two-layers of cells are used, as well as and for order 4 reconstructions. A full, two-layer, structured, centered stencil in three dimensions consists of 125 cells (5^3).

Besides the so-called full stencils, (27 cells using one layer or 125 cells using two layers), alternative (smaller) stencils can be derived using the one-layer or the two-layer formats. The only requirement here being that the stencil should be symmetric in all three directions so that it does not introduce any preferential direction when collecting the neighbours information to feed the system of equations used to retrieve the polynomial coefficients. For most of the high-order (4^{th} order) results to be presented here, for example, a contracted two-layer, central stencil with 56 neighbours was used. Figure 3.3(a) to Figure 3.3(e) illustrate the stencils that can be used to determine 20 coefficients needed for a K=3 reconstruction. Figure 3.3(c) to Figure 3.3(e) depict similar reduced and full stencils that can be used to determine 35 coefficients needed for a K=4 reconstruction.

Building the Least-Squares Problem

In this section, the formation of the over-determined system of equations required to calculate the reconstruction coefficients is described. A qualitative description of the ideas behind this process was given in the previous section and here the building of the system is formalized mathematically. The idea of pre-computing geometric coefficients and moments is described and the numerical methods used to solve the over-determined system in a least-squares sense are briefly presented, closing this section.

As mentioned in the previous section, the system of equations used to recover the reconstruction polynomial coefficients is over-determined, or, has more equations than unknowns. As such, a unique solution to the problem $\mathbf{Ax}-\mathbf{b}=0$ does not generally exist. Since the problem is over-determined the length of vector, $\mathbf{x}$, the number of unknowns, is less than the number of rows in $\mathbf{A}$ and length of $\mathbf{b}$ (the number of equations, related to the size of the stencil). The problem is more conveniently stated in a least-squares sense, where a vector, $\mathbf{x}$, is sought that minimizes the error vector $\mathbf{c}$ in $\mathbf{Ax}-\mathbf{b}=\mathbf{c}$. Mathematically, the problem becomes one of finding $\mathbf{x}$ that minimizes $||\mathbf{Ax}-\mathbf{b}||_2$, or finding $\mathbf{y}$ satisfying

$$\mathbf{y} = \min_{\mathbf{x}} ||\mathbf{Ax}-\mathbf{b}||_2^2 \tag{3.31}$$

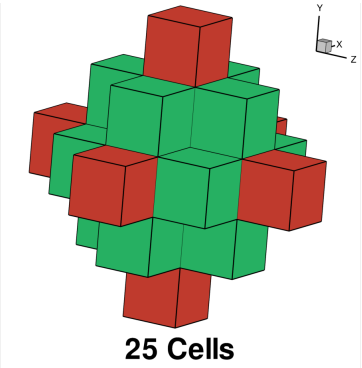

(a) 19 first-ring cells plus 6 extra second-ring cells for a total of 25

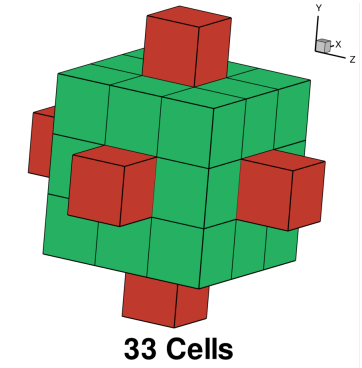

(b) 27 first-ring cells plus 6 extra second-ring cells for a total of 33

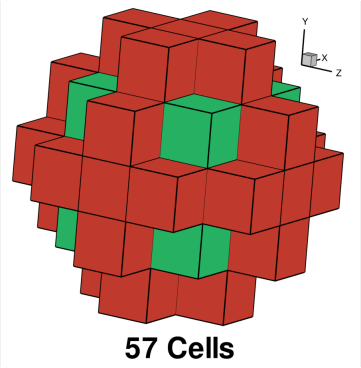

(c) 27 first-ring cells plus 5 extra second-ring cells per face for a total of 57

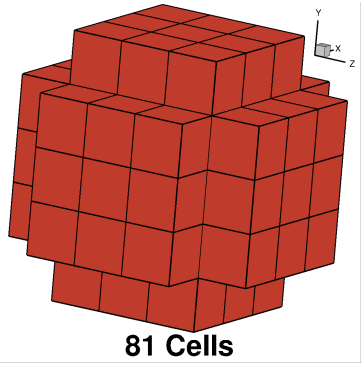

(d) 27 first-ring cells plus 9 extra second-ring cells per face for a total of 81

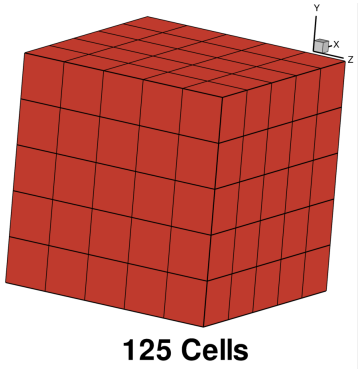

(e) Complete 125 cells stencil

Figure 3.3: Examples of several central reconstruction stencils for a cell (i, j, k) ranging in size from 25 to 125 cells that can be used to determine the polynomial coefficients of the high-order reconstructions ($K = 3$). The first-degree neighbours of the cell (i, j, k) are shown in green whereas dark red is used for the second-degree neighbours [2]

The formation of matrix, $\mathbf{A}$, and vector, $\mathbf{x}$, is then based on the rationale presented in previous Section 3.4.4.

In order to simplify the convoluted indexing that would arise if the notation used in the previous section was kept, it is useful to re-index the cell being reconstructed as cell, i, (previously indexed as ijk) and a neighbouring cell in the stencil of i will be indexed as cell, j (previously indexed pqr). The reconstruction polynomial for a given cell, i,may now be written as

$$U_i^K(x, y, z) = \sum_{p_1=0}^{K} \sum_{p_2=0}^{K} \sum_{p_3=0}^{K} (x - x_i)^{p_1} (y - y_i)^{p_2} (z - z_i)^{p_3} D_{p_1 p_2 p_3} , \tag{3.32}$$

following the definition used in Equation (3.28).

The volumetric averages of reconstruction of variable U, are then given as follows:

$$\overline{U_i} = \frac{1}{\mathcal{V}_i} \iiint_{\mathcal{V}_i} \Big[U_i^K(x,y,z) \Big] d\mathcal{V} \,, \tag{3.33}$$

$$\overline{U_j} = \frac{1}{\mathcal{V}_j} \iiint_{\mathcal{V}_j} \Big[U_i^K(x,y,z) \Big] d\mathcal{V} \,, \tag{3.34}$$

where $\overline{U_i}$ is the average of the reconstruction over the volume of i and $\overline{U_j}$, is the average of the reconstruction polynomial of cell, i,over the volume of a neighbouring cell, j,in the stencil.

Using the definition of the reconstruction polynomial given in Equation (3.32), Equation (3.34) can be re-written as

$$\overline{U_j} = \frac{1}{\mathcal{V}_j} \iiint_{\mathcal{V}_j} \Big[\sum_{p_1=0}^{K} \sum_{p_2=0}^{K} \sum_{p_3=0}^{K} (x-x_i)^{p_1} (y-y_i)^{p_2} (z-z_i)^{p_3} D_{p_1 p_2 p_3} \Big] d\mathcal{V} \,. \tag{3.35}$$

Since the unknown polynomial coefficients, $D_{p_1 p_2 p_3}$, are constants and the integration operation commutes with the summation, Equation (3.35) can be rearranged, yielding

$$\overline{U_j} = \sum_{p_1=0}^{K} \sum_{p_2=0}^{K} \sum_{p_3=0}^{K} \Big[D_{p_1 p_2 p_3} \cdot \frac{1}{\mathcal{V}_j} \iiint_{\mathcal{V}_j} (x-x_i)^{p_1} (y-y_i)^{p_2} (z-z_i)^{p_3} \, d\mathcal{V} \Big] \,. \tag{3.36}$$

It is important to emphasize the notation adopted here by explaining that Equation (3.36) represents the average over the volume of the neighbour cell, j,using the reconstruction function of cell i.

It is interesting to observe from Equation (3.36) that, when $p_1 = p_2 = p_3 = 0$, the first term of the reconstruction polynomial, D_{000}, is a constant, not depending on the location (x, y, z). This term actually represents the value of the reconstruction polynomial evaluated at the cell center, where $(x, y, z) = (x_i, y_i, z_i)$ and all terms but D_{000} are zero. Also, since we are not necessarily using piecewise constant or piecewise linear polynomial reconstructions the cell center value is not, in general, equal to the cell average value anymore: $D_{000} \neq \overline{U_i}$.

Equation (3.33) for the cell average value of the reconstruction in cell, i,can be rewritten with D_{000} extracted from the summation as

$$\overline{U_i} = D_{000} + \sum_{\substack{p_1=0 \\ (p_1+p_2+p_3 \leq K)}}^{K} \sum_{p_2=0}^{K} \sum_{p_3=0}^{K} D_{p_1 p_2 p_3} \cdot \frac{1}{\mathcal{V}_i} \iiint_{\mathcal{V}_i} (x-x_i)^{p_1} (y-y_i)^{p_2} (z-z_i)^{p_3} \, d\mathcal{V} \,. \tag{3.37}$$

The variable terms in Equation (3.37), which are a function of the location (x, y, z) are called the *geometric moments* of cell, i, taken about the cell center and are defined by

$$\left(\overline{x^{p_1} y^{p_2} z^{p_3}}\right)_i \equiv \frac{1}{\mathcal{V}_i} \iiint_{\mathcal{V}_i} (x - x_i)^{p_1} (y - y_i)^{p_2} (z - z_i)^{p_3} \, d\mathcal{V} \,, \tag{3.38}$$

allowing Equation (3.37) to be simplified to

$$\overline{U_i} = D_{000} + \sum_{\substack{p_1=0 \\ (p_1+p_2+p_3 \leq K)}}^{K} \sum_{p_2=0}^{K} \sum_{p_3=0}^{K} D_{p_1 p_2 p_3} \left(\overline{x^{p_1} y^{p_2} z^{p_3}}\right)_i . \tag{3.39}$$

Following an analogous reasoning for the average value in cell, j, one can obtain the expression

$$\overline{U_j} = D_{000} + \sum_{\substack{p_1=0 \\ (p_1+p_2+p_3 \leq K)}}^{K} \sum_{p_2=0}^{K} \sum_{p_3=0}^{K} D_{p_1 p_2 p_3} \left(\widetilde{x^{p_1} y^{p_2} z^{p_3}}\right)_j \,, \tag{3.40}$$

where the term $\left(\widetilde{x^{p_1} y^{p_2} z^{p_3}}\right)_j$ are the geometric moments of cell j with respect to the cell center of cell i, which are, similarly to Equation(3.38), defined as

$$\left(\widetilde{x^{p_1} y^{p_2} z^{p_3}}\right)_j \equiv \frac{1}{\mathcal{V}_j} \iiint_{\mathcal{V}_j} (x - x_i)^{p_1} (y - y_i)^{p_2} (z - z_i)^{p_3} \, d\mathcal{V} \,. \tag{3.41}$$

Rearranging Equation (3.39), an explicit function for D_{000} is obtained

$$D_{000} = \overline{U_i} - \sum_{\substack{p_1=0 \\ (p_1+p_2+p_3 \leq K)}}^{K} \sum_{p_2=0}^{K} \sum_{p_3=0}^{K} D_{p_1 p_2 p_3} \left(\overline{x^{p_1} y^{p_2} z^{p_3}}\right)_i . \tag{3.42}$$

This expression can be substituted into Equation(3.40) providing and expression for $\overline{U_j} - \overline{U_i}$ given by

$$\overline{U_j} - \overline{U_i} = \sum_{\substack{p_1=0 \\ (p_1+p_2+p_3 \leq K)}}^{K} \sum_{p_2=0}^{K} \sum_{p_3=0}^{K} D_{p_1 p_2 p_3} \cdot \left[\left(\widetilde{x^{p_1} y^{p_2} z^{p_3}}\right)_j - \left(\overline{x^{p_1} y^{p_2} z^{p_3}}\right)_i \right] . \tag{3.43}$$

By further manipulation of the geometric moments terms and defining

$$\left(\widehat{x^{p_1} y^{p_2} z^{p_3}}\right)_{ij} \equiv \left(\widetilde{x^{p_1} y^{p_2} z^{p_3}}\right)_j - \left(\overline{x^{p_1} y^{p_2} z^{p_3}}\right)_i \,, \tag{3.44}$$

the system of equations to be solved can be written as

$$\left(\widehat{x^{p_1}y^{p_2}z^{p_3}}\right)_{ij} \cdot \sum_{\substack{p_1=0 \\ (p_1+p_2+p_3\leq K)}}^{K}\sum_{p_2=0}^{K}\sum_{p_3=0}^{K} D_{p_1p_2p_3} = \overline{U_j} - \overline{U_i}\,. \tag{3.45}$$

Equation (3.45) can be re-arranged in matrix form, $\mathbf{A}\mathbf{x}-\mathbf{b}=\mathbf{c}$ and written as

$$\underbrace{\begin{bmatrix} \left(\widehat{x^0y^0z^1}\right)_{i1} & \dots & \left(\widehat{x^{p1}y^{p2}z^{p3}}\right)_{i1} & \dots & \left(\widehat{x^ky^0z^0}\right)_{i1} \\ \vdots & & \vdots & & \vdots \\ \left(\widehat{x^0y^0z^1}\right)_{ij} & \dots & \left(\widehat{x^{p1}y^{p2}z^{p3}}\right)_{ij} & \dots & \left(\widehat{x^ky^0z^0}\right)_{ij} \\ \vdots & & \vdots & & \vdots \\ \left(\widehat{x^0y^0z^1}\right)_{iM} & \dots & \left(\widehat{x^{p1}y^{p2}z^{p3}}\right)_{iM} & \dots & \left(\widehat{x^ky^0z^0}\right)_{iM} \end{bmatrix}}_{M\times N} \underbrace{\begin{pmatrix} D_{001} \\ \vdots \\ D_{p_1p_2p_3} \\ \vdots \\ D_{k00} \end{pmatrix}_i}_{N\times 1} - \underbrace{\begin{pmatrix} (\overline{\mathbf{U}}_1 - \overline{U_i}) \\ \vdots \\ (\overline{\mathbf{U}}_j - \overline{U_i}) \\ \vdots \\ (\overline{\mathbf{U}}_M - \overline{U_i}) \end{pmatrix}}_{M\times 1} = \underbrace{\begin{pmatrix} c_1 \\ \vdots \\ c_j \\ \vdots \\ c_M \end{pmatrix}_i}_{M\times 1},$$

for the matrix defined above, the parameter M represents the total number of neighbouring cells in the reconstruction stencil, or the number of equations, and N represents the total number of unknown derivatives (polynomial coefficients to be found), minus one, since D_{000} is not dependent on (x, y, z) and is explicitly obtained from Equation (3.42). As will be emphasized in the next section, it is interesting to notice that the matrix, $\mathbf{A}$, depends only on the coordinates (x, y, z) of cell, i, centroid and of its neighbours, j, centroids. Therefore, $\mathbf{A}$ is only dependent on the mesh geometry. This will be important for the selection of a convenient strategy to solve the over-determined system by taking advantage of the fact that $\mathbf{A}$ can be pre-computed once the mesh is generated and should not change if the mesh does not change. Also, vector, $\mathbf{b}$, depends only on the known cell average values.

The present implementation of the least-squares problem solutions permits the application of *geometric weighting* to each cell in the reconstruction stencil of cell, i, based on the distance between the cell centers of the neighbours, j, in the reconstruction stencil and the center of cell, i. The weighting is akin to a pre-conditioning of the over-determined system, where cells closer to cell, i, would have higher relevance (weight) in the calculation of the polynomial coefficients than cells in the stencil that are further away from the centroid of cell, i. The geometric weights, w_{ij} of a neighbour, j, with respect to cell, i, are applied by multiplying the lines of matrix, $\mathbf{A}$, and of the vector, $\mathbf{b}$, corresponding to that particular j neighbour. The advantages of the

weighting procedures become more pronounced in unstructured grids or when dealing with high aspect ratio cells near curved boundaries, although none of these options are covered by the present work. Defining $\overrightarrow{r}$ to be the position vector of the centroid of neighbouring cell, j, with respect to the centroid of i the two options available for geometric weighting are the inverse distance and inverse distance squared, given by

$$w_{ij} = \frac{1}{|\overrightarrow{r}_j - \overrightarrow{r}_i|}, \tag{3.46}$$

or

$$w_{ij} = \frac{1}{|\overrightarrow{r}_j - \overrightarrow{r}_i|^2}\,, \tag{3.47}$$

By analysing the definition of the geometric moments, that is the quantity $\left(\overline{x^{p_1} y^{p_2} z^{p_3}}\right)_j$ given by

$$\left(\overline{x^{p_1} y^{p_2} z^{p_3}}\right)_j \equiv \frac{1}{\mathcal{V}_j} \iiint_{\mathcal{V}_j} (x - x_j)^{p_1} (y - y_j)^{p_2} (z - z_j)^{p_3}\, d\mathcal{V}\,, \tag{3.48}$$

it can be seen that the higher geometric moments (higher powers) can be computed based on the lower power geometric moments.

Appropriate algebraic manipulation and binomial expansions of the expressions above will allow for a very efficient computation of the geometric moments by basically reusing lower moments to provide the higher moments in a loop. This is fact done within the current implementation. It is not the goal of the present work to describe these manipulations in detail since they are not an integral part of the methodology, rather a convenience for the efficiency of implementation. The interested reader may refer to the earlier work of Rashad [24] for a complete description of these transformations.

Solution of the Least-Squares Problem

There are two different methods used here for the solution of the least squares problem: the *Householder QR Factorization* and the *Pseudo-Inverse obtained by Singular Value Decomposition (SVD)*. It is not the goal here to describe these methods in complete detail and the interested reader may want to refer to specific literature on linear algebra [159, 160]. Nevertheless, a brief explanation summarizing the main ideas behind each method is provided below for completeness.

The first method, the *Householder QR Factorization*, is based on the principle that one can re-write any rectangular matrix, in this case $\mathbf{A}$, as a product of an orthogonal matrix, $\mathbf{Q}$, and

an upper-triangular matrix, $\mathbf{R}$, such that

$$\mathbf{A} = \mathbf{QR}\,. \tag{3.49}$$

There are different methods available for determining the matrices $\mathbf{Q}$ and $\mathbf{R}$, among them are the Gram-Schmidt process, the Householder transformations, or the Givens rotations [160], for example. In this work, the QR Householder method is selected. Some details, as said before, are omitted for brevity, and we assume that $\mathbf{Q}$ and $\mathbf{R}$ were properly obtained. Matrix, $\mathbf{Q}$, has dimensions $M \times M$, and the matrix, $\mathbf{R}$, is partitioned into an $N \times N$ upper-right triangular matrix and an $(M-N) \times N$ zero block. Here, M and N are defined by the number of equations and unknowns. By pre-multiplying by $\mathbf{Q}^T$, the least-squares problem, $\min ||\mathbf{Ax} - \mathbf{b}||^2$, can be rewritten as

$$\min ||\mathbf{Q}^T\mathbf{Ax} - \mathbf{Q}^T\mathbf{b}||^2\,. \tag{3.50}$$

The least-squares problem of Equation (3.50) can then be re-written using the QR factorization shown in Equation (3.49) as

$$\min ||\mathbf{Q}^T\mathbf{QRx} - \mathbf{Q}^T\mathbf{b}||^2\,. \tag{3.51}$$

Also, $\mathbf{Q}$ is orthogonal by definition, therefore $\mathbf{Q}^T\mathbf{Q} = I$, leading to

$$\min ||\mathbf{Rx} - \mathbf{Q}^T\mathbf{b}||^2\,. \tag{3.52}$$

Since the matrix, $\mathbf{R}$, is upper-triangular the minimization problem can then be solved by solving the following system via back-substitution [161]:

$$\mathbf{Rx} - \mathbf{Q}^T\mathbf{b} = \mathbf{Q}^T\mathbf{c}\,. \tag{3.53}$$

The vector, $\mathbf{x}$, of length N, is then the solution that satisfies $\min ||\mathbf{Ax} - \mathbf{b}||^2$.

The other alternative available for solving the least-squares problem is the *orthogonal Singular Value Decomposition (SVD)* of matrix, $\mathbf{A}$, in order to obtain a so-called *pseudo-inverse* matrix, $\mathbf{A}^+$. The pseudo-inverse matrix, $\mathbf{A}^+$, which has dimensions $N \times M$, allows the least-squares problem to be solved directly as

$$\mathbf{x} = \mathbf{A}^+\mathbf{b}\,. \tag{3.54}$$

According to the SVD method, $\mathbf{A}$ can be decomposed as a product of a matrix, $\mathbf{Q}$, which is an $M \times M$ orthogonal matrix, a matrix $\mathbf{\Sigma}$, which is an $M \times N$ rectangular diagonal matrix with non-negative real values along the diagonal, and a matrix, $\mathbf{V}$, which is an $N \times N$ orthogonal

matrix given by

$$\mathbf{A} = \mathbf{Q}\mathbf{\Sigma}\mathbf{V}^T \,. \tag{3.55}$$

The derivation and detailed explanation of how to obtain the auxiliary matrices, $\mathbf{V}$, $\mathbf{\Sigma}$ and $\mathbf{Q}$ used in this method are omitted here for brevity but can found in standard literature on linear algebra [160]. The inversion of $\mathbf{A}$ comes from the inversion of the right hand side of Equation (3.55). This leads to the following expression for $\mathbf{A}^+$:

$$\mathbf{A}^+ = \mathbf{V}\mathbf{\Sigma}^-\mathbf{Q}^T \,. \tag{3.56}$$

In the above expression, matrices, $\mathbf{Q}$ and $\mathbf{V}$, are orthogonal, therefore their inverses are equal to their transposes. Matrix, $\mathbf{\Sigma}$, is a diagonal matrix, meaning that its inverse is its reciprocal. The values on the diagonal of the matrix, $\mathbf{\Sigma}$, are called "singular values", originating the name of the method.

The benefit of this method for the current application is that, since the pseudo-inverse depends only on the geometry of the mesh, it can be pre-computed and stored, allowing for a very efficient way of calculating the unknown derivatives, $D_{p_1p_2p_3}$. Among the two available alternatives, the SVD method with storing of the pseudo-inverse was found by Ivan and Groth [17] to provide significant computational speed-up for high-order two-dimensional Euler computations in comparison to the situation where the coefficient matrix, $\mathbf{A}$, is formed and a least-squares subroutine is called for each spatial reconstruction at every time step. Unless otherwise noted, the preferred method used in the present work is the method of storing the pseudo-inverse matrix found via SVD.

It was acknowledged by Ivan and Groth [62] that, particularly when considering high-order applications, where the stencil size and consequently the size of the least-squares problem grow with the order of the scheme, there is a potential for issues with the conditioning of the least-squares problem. Also, the conditioning of the least-squares problem is very dependent on mesh features, such as the cell spacing and specially the cell aspect ratio. Meshes typically used in boundary or shear layers, for example, will tend to have very high aspect ratios. In order to improve the conditioning of the least-squares problem a column-scaling procedure is available in the present code. In this procedure a diagonal column-scaling matrix, $\mathbf{D}_\mathrm{C}$, is defined where the diagonal entries are equal to the inverse of the maximum absolute value of the entries of each column of matrix, $\mathbf{A}$. Applying a post-multiplication of $\mathbf{A}$ by $\mathbf{D}_\mathrm{C}$ results in the product, $\mathbf{A}\mathbf{D}_\mathrm{C}$, for which all the entries of are in the range $[-1, 1]$. Therefore, the modified least squares

problem can be expressed as

$$\mathbf{A}\mathbf{D}_{\mathrm{C}}\mathbf{D}_{\mathrm{C}}^{-1}\mathbf{x}-\mathbf{b}=\mathbf{A}\mathbf{D}_{\mathrm{C}}\mathbf{z}-\mathbf{b}=\mathbf{e}\,, \tag{3.57}$$

where $\mathbf{x}=\mathbf{D}_{\mathrm{C}}\mathbf{z}$. Ivan and Groth [62] have shown that this scaling procedure greatly improves the condition number of the least-squares problem, testing it for different meshes with various aspect-ratios and also for different reconstruction orders.

3.4.5 Smoothness Indicator

As explained in Section 3.4.3, the K-exact polynomial reconstruction is based on the Taylor series expansion of the solution and assumes that the solution is smooth and continuously differentiable up to order K. In order to check for the suitability of such a high-order reconstruction for the particular variable being reconstructed within a cell, Ivan and Groth [149, 17] developed the concept of a smoothness indicator. The smoothness indicator, S, is a metric used to indicate quantitatively how smooth the reconstruction polynomial actually is. In a perfectly smooth solution, the reconstruction polynomials used to fit the solution in one cell would be the same as the reconstruction polynomials used to fit the solution in a neighbouring cell. The idea behind the smoothness indicator, S, is to compare how the polynomial reconstruction derived from a given cell, ijk, performs when extrapolated to the neighbouring cells, pqr, in relation to the polynomial reconstruction of the neighbouring cell, pqr.

The main part of the calculation of the smoothness indicator is the evaluation of the solution smoothness parameter, α, for cell ijk and solution variable U, given as follows:

$$\alpha=1-\frac{\sum_{pqr}(U_{pqr}^{K}(x_{pqr},y_{pqr},z_{pqr})-U_{ijk}^{K}(x_{pqr},y_{pqr},z_{pqr}))^{2}}{\sum_{pqr}(U_{pqr}^{K}(x_{pqr},y_{pqr},z_{pqr})-\overline{U}_{iijk})^{2}}\,. \tag{3.58}$$

where, p, q, and r represent the indexing of the neighbouring cells in the x, y, and z directions. It is useful to explain the meaning of each term in the above equation, making it clear how the reconstruction comparison is performed. The variable $U_{pqr}^{K}(x_{pqr},y_{pqr},z_{pqr})$ is the reconstruction polynomial derived for a neighbouring cell, pqr, and evaluated at the cell center of cell pqr. Variable $U_{ijk}^{K}(x_{pqr},y_{pqr},z_{pqr})$ is the value obtained by applying the reconstruction polynomial of cell ijk, $U_{ijk}^{K}(x,y,z)$, to the cell center of the neighbouring cell, pqr. The average value of U in cell ijk, $\overline{U}_{iijk}$ is used as reference value to normalize the distance measured in the numerator of Equation (3.58). It is important to observe that the actual range for α is $-\infty<\alpha\leq 1$, and it will be closer to unity as the solution becomes smoother. With progressive mesh refinement the reconstruction in neighbouring cells will become more similar and in the limit of a perfect

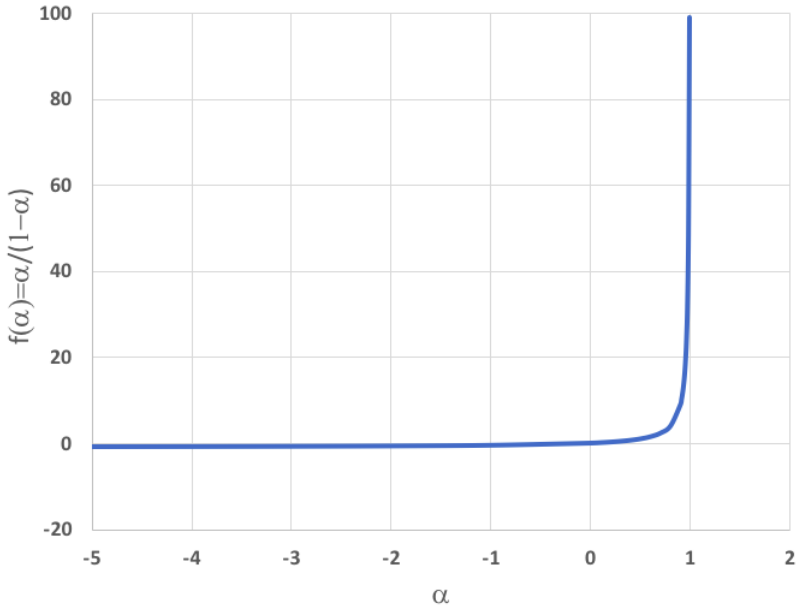

Figure 3.4: Variation of function $f(\alpha) = \frac{\alpha}{1-\alpha}$

match between these reconstructions, as the mesh spacing tends to zero, the coefficient α will tend to unity.

The actual smoothness indicator, S, is then calculated as function of α as

$$S = \frac{\alpha}{\max((1-\alpha), \epsilon)} \frac{(M-N)}{N-1} \,. \tag{3.59}$$

where, ϵ is a reference small number to avoid division by zero, M is the size of the stencil, and N is the number of unknown derivatives. The idea of using M and N here is to non-dimensionalize the coefficient, S, with respect to the stencil size in order to keep the order of magnitude of S comparable across different stencils sizes. A pass/no-pass cutoff value, S_c, is compared to the calculated value of S. The smoother the solution the higher the value of S. The cutoff value has been demonstrated to detect discontinuous regions very well when set to the range $1,000$-$5,000$ [17]. The behaviour of the function $f(\alpha) = \alpha/(1-\alpha)$ is depicted in Figure 3.4 showing its rapid growth as α approaches unity.

If the value of the smoothness indicator is below the set cutoff, the hybrid procedure is activated, the cell is flagged as under-resolved and the reconstruction type is locally switched to a limited, piecewise linear reconstruction, as explained in the general discussion of slope limiters in Section 3.2.2. This switching procedure defines the hybrid approach characteristic of the CENO scheme and allows it to handle discontinuities in a monotonic fashion as well as deal with smooth

extrema to high accuracy.

3.4.6 High-Order Treatment of Inviscid Fluxes

Once the solution is reconstructed to the desired order of accuracy at the cell boundary, the inviscid flux calculation can be performed by the solution of a Riemann problem [140] between the states given by the reconstruction of the solution on each cell adjacent to the boundary. The Riemann solver solution will be of high-order as long as the reconstruction used to calculate the function values at the boundaries is of high-order [162]. The AUSM$^+$-up approximate Riemann solver of Liou [137] is used [69]. Additionally, the accuracy of the integration method used to integrate the flux numerically should, therefore, not degrade the spatial accuracy given by the reconstruction method. As discussed in Section 3.3.4 the high-order integration of the surface flux is performed by using a two-dimensional Gauss-Legendre quadrature combined with the trilinear transformation, as given by Equation (3.27). The number of Gauss quadrature points is increased as a function of the order of the reconstruction. In the three-dimensional case, we use $N_g = 1$ for first- and second-order schemes, and $N_g = 4$ for third- and fourth-order schemes [17], to ensure that the spatial accuracy of the scheme is preserved.

3.4.7 High-Order Treatment of Viscous Fluxes

In order to achieve a consistent order of accuracy for the entire spatial discretization scheme, the elliptic operators (viscous terms) appearing in the Navier-Stokes equations for the reactive mixture must also be calculated based on the high-order reconstruction scheme presented in section 3.2.1. One important difference now is that the elliptic terms appearing in Equations (2.78), (2.79) and (2.80) are not only dependent on the solution variables at the interface but also on the solution variables gradients at these interfaces. These dependencies can be expressed as

$$\vec{\mathbf{F}^{\mathrm{V}}} \cdot \vec{n} = \vec{\mathbf{F}^{\mathrm{V}}}(\mathbf{U}_{left}, \nabla\mathbf{U}_{left}, \mathbf{U}_{right}, \nabla\mathbf{U}_{right}, \vec{n}, \eta = 0) \, . \tag{3.60}$$

Following the work by Ivan and Groth [61] for two-dimensional flows, the treatment adopted here for the elliptic fluxes evaluation also relies on obtaining K^{th}-order accurate gradient by the differentiation of the K^{th}-exact reconstruction polynomial used for each of the solution variables. The solution value and gradient is calculated by simple arithmetic means of the left and right values [61]. Therefore, starting with the K-exact reconstruction polynomial defined by

$$U^K_{ijk}(x,y,z) = \sum_{p_1=0}^{K} \sum_{p_2=0}^{K} \sum_{p_3=0}^{K} (x - x_{ijk})^{p_1} \, (y - y_{ijk})^{p_2} \, (z - z_{ijk})^{p_3} \, D_{p_1 p_2 p_3} \, , \tag{3.61}$$

the gradients of the reconstruction are directly given by differentiating the polynomial of Equation (3.61) with respect to the three directions x, y and z arriving at

$$\frac{\partial U^K_{ijk}(x,y,z)}{\partial x} = \sum_{\substack{p_1=0 \\ (p_1+p_2+p_3\leq K)}}^{K}\sum_{p_2=0}^{K}\sum_{p_3=0}^{K} p_1(x-x_i)^{p_1-1}(y-y_i)^{p_2}(z-z_i)^{p_3}D_{p_1p_2p_3}\,, \tag{3.62a}$$

$$\frac{\partial U^K_{ijk}(x,y,z)}{\partial y} = \sum_{\substack{p_1=0 \\ (p_1+p_2+p_3\leq K)}}^{K}\sum_{p_2=0}^{K}\sum_{p_3=0}^{K} p_2(x-x_i)^{p_1}(y-y_i)^{p_2-1}(z-z_i)^{p_3}D_{p_1p_2p_3}\,, \tag{3.62b}$$

$$\frac{\partial U^K_{ijk}(x,y,z)}{\partial z} = \sum_{\substack{p_1=0 \\ (p_1+p_2+p_3\leq K)}}^{K}\sum_{p_2=0}^{K}\sum_{p_3=0}^{K} p_3(x-x_i)^{p_1}(y-y_i)^{p_2}(z-z_i)^{p_3-1}D_{p_1p_2p_3}\,. \tag{3.62c}$$

The constant terms D_{000}, present in Equation (3.61), drops out in the above expressions for the derivatives.

As was the case for the hyperbolic fluxes, the left and right reconstructions at a given interface may not yield a unique solution and solution gradient value at the interface. For the viscous fluxes, the interface solution values and solution gradients are calculated simply by directly averaging the right and left state and gradients at a quadrature point at the interface, obtained by means of the respective reconstruction polynomials on the right and left cell sharing that interface [61]. Considering a cell interface in the x-direction, the arithmetic means of both the solution and its gradients are obtained as follows:

$$U_{i+\frac{1}{2},j,k} = \frac{(U_{left}+U_{right})}{2}\,, \tag{3.63}$$

$$\nabla U_{i+\frac{1}{2},j,k} = \frac{(\nabla U_{left}+\nabla U_{right})}{2}\,. \tag{3.64}$$

The above expression for the elliptic discretization has been considered by Ollivier-Gooch and Altena [163] and Ivan and Groth [61] and was successfully applied to the advection-diffusion equation by Ivan and Groth [61]. It was observed that for uniform Cartesian grids, an increase of one order of magnitude in accuracy is obtained due to error cancellation. For $K = 1$ and $K = 3$ cases, orders of accuracy $K = 2$ and $K = 4$ were observed. The analysis by Ivan and Groth indicate that this particular behaviour can only be expected on uniform Cartesian grids,

where error cancellations due to the mesh symmetry occurs, but not on arbitrary grids. In light of this, Ivan and Groth guarantee the order of accuracy of the discretization for arbitrary grids by always increasing the order of the reconstruction scheme by one. Equations (3.62) for the solution gradients have leading truncation error terms which are one order less than the K^{th}-order solution reconstruction polynomial, given by Equation ((3.28)). As such, in order to obtain a K^{th}-order accurate spatial discretization (for elliptic operators and the Navier-Stokes equations), a K^{th}-order reconstruction polynomial is used. For example, to achieve a fourth-order scheme, piecewise quartic reconstruction, with $K = 4$, is therefore required, as proposed by Ivan and Groth [61]. It is also worth mentioning that the solution reconstruction used for the viscous fluxes calculations does not require limiting, as is the case for the inviscid fluxes.

After performing the averaging procedure using the left and right solution values at each quadrature point, the last step remaining is the Gauss quadrature integration, in the same fashion as performed for the inviscid fluxes, using Equation (3.27).

3.4.8 High-Order Treatment of Source Terms

Similarly to what was described for the viscous fluxes, the source vector integration is also performed based on the unlimited reconstructions. Also, the source terms, as can be seen in Equation (2.81), depend not only the reconstructed solution variables but also on the reconstructed spatial gradient of the solution variables. The source term of interest in this work contains terms related to chemistry and turbulence modelling and these terms are also dependent on the solution and gradient. According to the methodology presented in Section 3.3.4, a Gauss-Legendre quadrature method is adopted, applying the modifications shown in Equation (3.25) to handle volumetric integrations in non-Cartesian elements by means of a trilinear transformation.

According to the order of the scheme being used the number of quadrature points may vary. To get a fourth-order accuracy, a $K = 4$ reconstruction is performed and a Gauss-Legendre quadrature using $n = 2$ points per-direction is used. If two points per direction are used it implies that 2^3=8 points are used in total per cell for each cell.

3.4.9 Time Marching

The time integration of the coupled non-linear ordinary differential equations (ODEs) represented in Equation 3.5 is solved by using a time marching procedure. For a more extensive discussion on the available options, including implicit and explicit schemes, the textbook of Lomax *et al.* [13] is suggested. In this work, only explicit procedures are considered, and in par-

ticular the explicit second and fourth-order Runge-Kutta time-marching schemes are employed. The effective time step is calculated based on inviscid, viscous and chemical constraints, given by the Courant-Friedrichs-Lewy (CFL) stability criteria, the viscous von Neumann stability criteria, and a chemical time criteria based on the magnitude of the chemical source terms as discussed by Hernàndez-Pérez [69].

3.4.10 Boundary Conditions

The current implementation makes use of ghost cells to enforce high-order boundary conditions. The use of ghost cells, as well as alternative ways of enforcing boundary conditions, including the use of constrained reconstructions, were investigated previously by Ivan and Groth [148, 23]. The constrained reconstruction option is not considered in this work, but is mentioned again in the closing sections as suggestion for future work.

The ghost cells approach, chosen for its simplicity of implementation and adequacy to the present goals, is applied by artificially extending the solution domain beyond its boundaries, creating additional layers of cells. For these ghost-cells, the cell-averaged values are pre-specified by the boundary conditions. In general, the high-order CENO scheme used here will require four ghost cells in each direction, since a two-layer stencil is needed and to those two layers extra cells are added for the calculation of the smoothness indicator on the stencil. A more comprehensive discussion on the minimum number of ghost cells and its relation to the smoothness indicator is provided by Rashad [24].

3.4.11 Parallel Multi-Block Implementation

The multi-block finite-volume scheme considered in this study has been previously used for the solution of several classes of problems, including not only the Euler and Navier-Stokes equations as discussed here, but also MHD [164], Gaussian moment closure equations in 2D[11] and in 3D [165]. The numerical scheme presented here takes advantage of the existing parallel multi-block architecture of the implementation, gaining a lot of flexiblity to handle large meshes in a multi-processor computational environment. Ghost cells are used for the interblock communications which makes used of the message passing interface (MPI) library [166, 167] and the C++ programming language. The number of cells in each direction Nc_x,Nc_y and Nc_z is constant for all the blocks, but a variable number of blocks is permitted on each processor adding greater flexibility to the approach [60, 168]. Also, the multiblock strategy shows important advantages when considering AMR [60]. Figure 3.5, as presented by Rashad [24], illustrates the overlapping ghost cells in both two-dimensional and three-dimensional multi-block meshes.

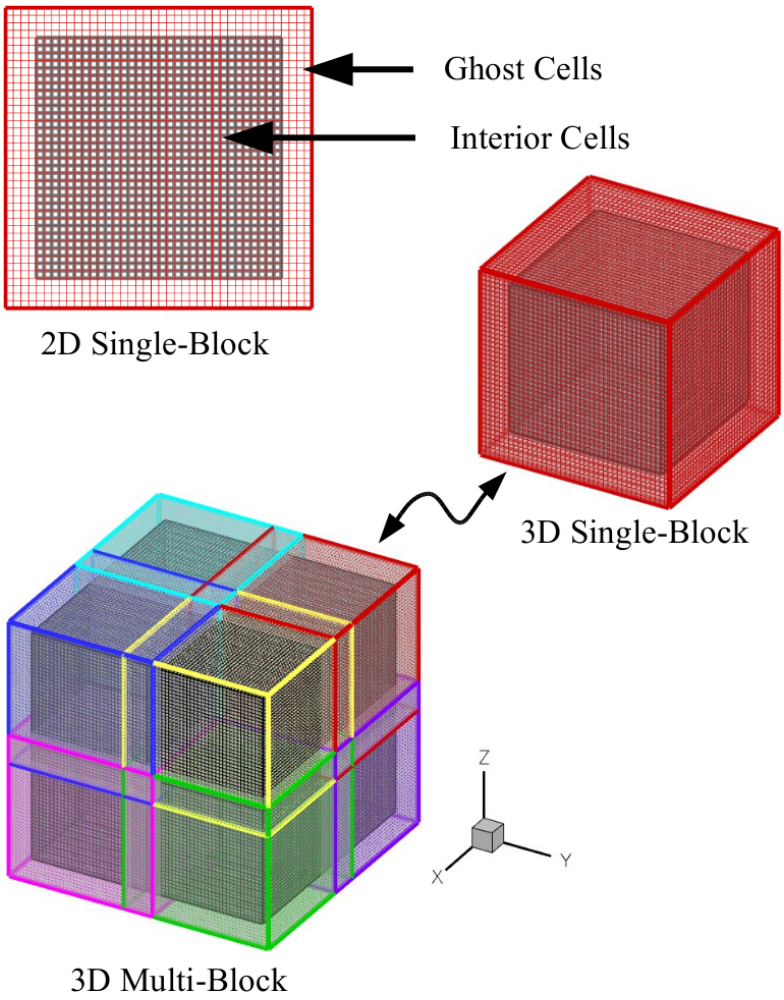

Figure 3.5: Distribution of ghost cells for multi-block hexahedral meshes in 2D and 3D.

3.5 Verification of Aspects of Numerical Solution Method

The verification and validation of the proposed high-order CENO finite-volume spatial discretization procedure have been demonstrated quite extensively in previous studies by Ivan *et al.* [152], Susanto *et al.* [164], Charest *et al.* [155], Freret *et al.* [169] for both 2D and 3D inviscid and laminar compressible flows, as well as ideal MHD plasma flows. Nevertheless, additional verification of the current implementation of the CENO scheme has been carried out here for the 3D multi-block hexahedral meshes and the reactive flow applications of interest.

In this section, the results of the additional verification studies involving several test cases for the current implementation of the proposed CENO scheme are presented for 3D hexahedral, multiblock mesh. For these verification studies, non-reactive cases are considered. Each of the tests aims at testing the consistency of a different component of the implementation, allowing

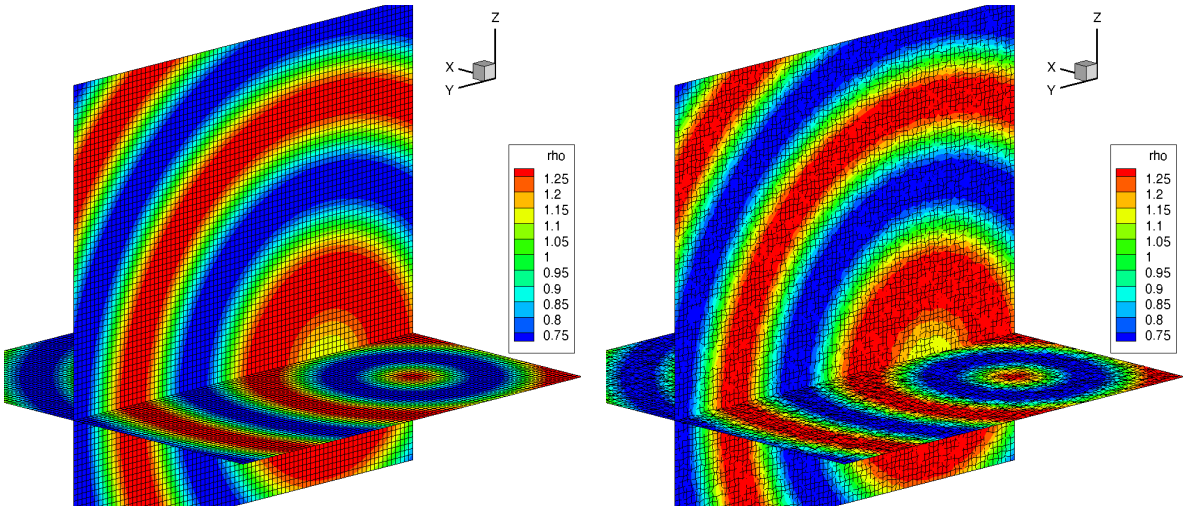

(a) Cut planes showing radial cosine function reconstructed on Cartesian mesh (CENO 5^{th}) order

(b) Cut planes showing radial cosine function reconstructed on hexahedral mesh (CENO 5^{th}) order

Figure 3.6: Cut planes comparing the 5^{th} order reconstruction function working on hexahedral (disturbed) mesh as expected in comparison to the Cartesian mesh

for the verification of the implementation and solution method.

3.5.1 High-Order Reconstruction of Prescribed Functions

Smooth Trigonometric Function

The first test considered herein is the verification of the high-order CENO solution reconstruction for three-dimensional Cartesian as well as general hexahedral meshes, by studying the reconstruction of prescribed functions. Remembering that a hexahedral cell may in general have non-planar faces, the representative general hexahedral meshes were obtained here by randomly perturbing originally uniform Cartesian meshes. As a first case, reconstruction of a radial cosine function was examined on a solution domain of size ($20\,\mathrm{m} \times 20\,\mathrm{m} \times 20\,\mathrm{m}$). For this smooth and continuous function, the goal was to establish that the formal order of accuracy of the reconstruction was achieved on hexahedral elements. Furthermore, as the reconstruction process relies on the evaluation of volumetric integrals for the cell volume itself and centroid locations, as well as to integrate the geometric moments required to construct the least-squares problem for the reconstruction, this test case also provided a confirmation of the effectiveness of the trilinear transformation and volumetric quadrature for the general non-Cartesian hexahedral elements.

The computed distributions of the reconstructed radial cosine function on both three-dimensional Cartesian and disturbed hexahedral meshes are illustrated in Figure 3.6. Furthermore, it is

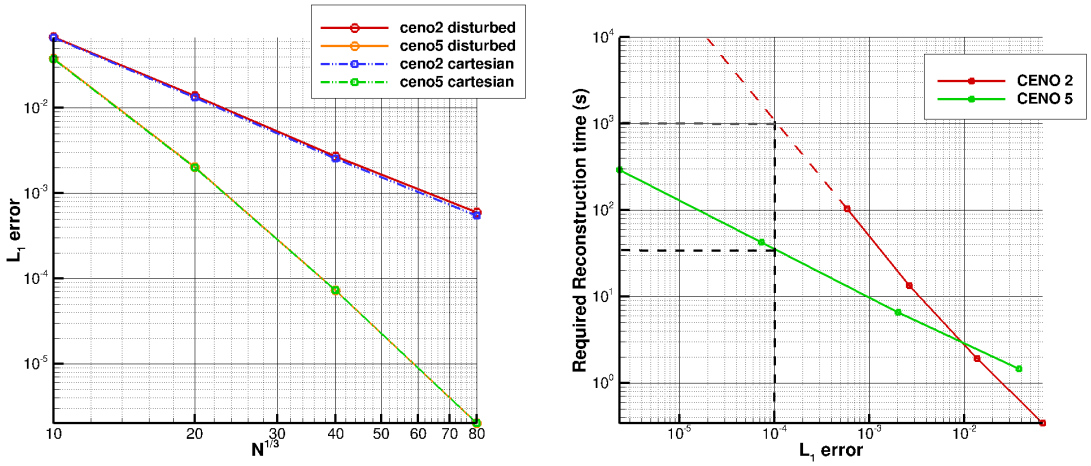

(a) Error Analysis for Radial Cosine function using 2^{nd} and 5^{th} order accuracy on Cartesian and hexahedral (disturbed) mesh

(b) Analysis of time required to achieve a desired error level with a given reconstruction. Comparison between 2^{nd} and 5^{th} order.

Figure 3.7: Error Analysis demonstrating proper order of accuracy for the CENO scheme in a disturbed mesh and time required for desired error level based on order of the reconstruction.

shown in Figure 3.7(a) that the expected orders of accuracy of the $K=2$ and $K=4$ schemes are achieved on both regular and perturbed meshes. An interesting result is also found by comparing the time required to perform the solution reconstruction with different orders of accuracy for the meshes considered as depicted in Figure 3.7(b). One can see that for a given error the time required by the second-order scheme may be orders of magnitude higher than the time required by the corresponding fifth-order scheme.

Non-Smooth Abgrall Function

In order to investigate the CENO solution reconstruction procedure for non-smooth functions, the well-known Abgrall function [170] was considered. By construction, this function contains several solution discontinuities in order to present challenges to any reconstruction scheme hoping to enforce solution monotonicity. For this case, the functionality and reliability of the smoothness indicator used in the hybrid CENO reconstruction procedure is also demonstrated. The main goal here was to show that consistent results can also be obtained using the general hexahedral elements. This two-dimensional function is extruded in the z-direction and applied to a three-dimensional domain. Progressive refinements are considered by increasing the number of elements in both x and y directions only and keeping the number of elements in z-direction constant. Therefore we can asses the generic hexahedral implementation with a simple two-dimensional function.

Considering the number of discontinuous regions within the domain, as shown in Figure 3.8(b),

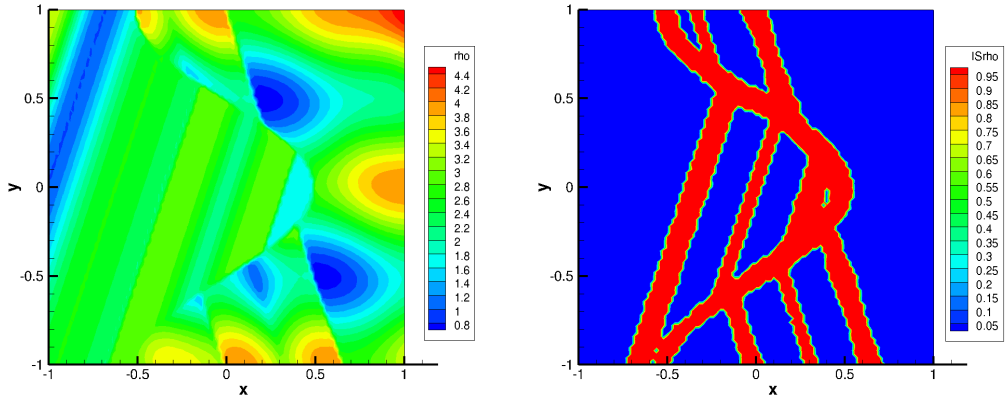

(a) Fifth-Order CENO reconstruction on a hexahedral (disturbed) mesh - contour of ρ for Abgrall function

(b) Fifth-Order CENO reconstruction on a hexahedral (disturbed) mesh - contour of the smoothness indicator for variable ρ for the Abgrall function

Figure 3.8: Demonstration of the smoothness indicator use with disturbed hexahedral cells flagging the discontinuous regions in the field of variable ρ for the Abgrall function.

it is expected that the high-order hybrid CENO scheme will reduce to a low-order mode in a high number of cells, reducing the overall order of accuracy. Although this is true, one can see from Figure 3.9 that, while the high-order scheme exhibits a grid-convergence rate or order of accuracy (slope) that is similar to the first-order scheme, it is also evident that the absolute value of the error for the high-order reconstructed solution is considerably smaller than that of the usual first-order scheme. For the target solution error given in the figure, a much fewer number of cells ($100 \times 100 = 10{,}000$) is required by the high-order to scheme to achieve the same accuracy as the first-order scheme on a fine mesh ($180 \times 180 = 32{,}400$). Extrapolating this result to a fully three-dimensional case, where the function could also vary in the z-direction, the ratio $(180^3)/(100^3)$ indicates that about 5.8 times more cells would be required by the low-order scheme to return the same level of error as the high-order CENO approach.

3.5.2 Non-Reactive Inviscid Flow — Wave Propagation

Partial verification of the implementation of the high-order inviscid flux function is achieved here by solving a simple wave propagation problem on a periodic domain. A periodic sinusoidal field was initialized for the density field, ρ, and a uniform x-direction velocity of u=100 m/s was applied. The magnitude of the velocity components in the y and z directions were taken to be zero and a uniform pressure of p=101,325 Pa was assumed. The expected exact solution for the density, ρ, after a full period (20 ms) is the same as the initial solution distribution, without lags in phase or amplitude decays associated with the numerical discretization scheme. In

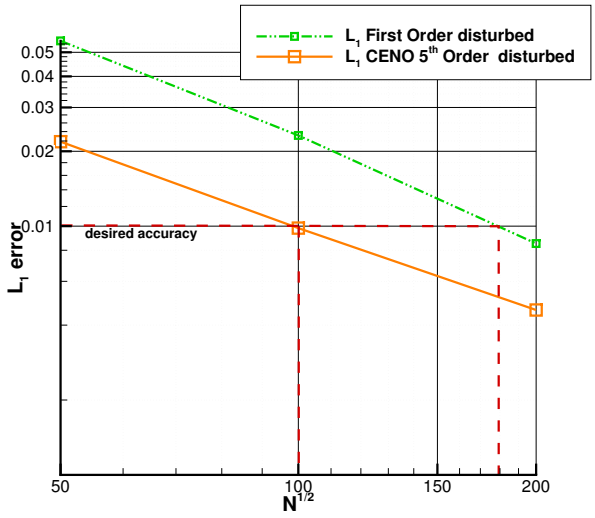

Figure 3.9: Comparison of L_1-error obtained with first and fifth-order reconstruction. Dashed lines exemplify the smaller number of cells required by high-order scheme for a given error, despite slopes being similar due to large number of cells flagged as discontinuous.

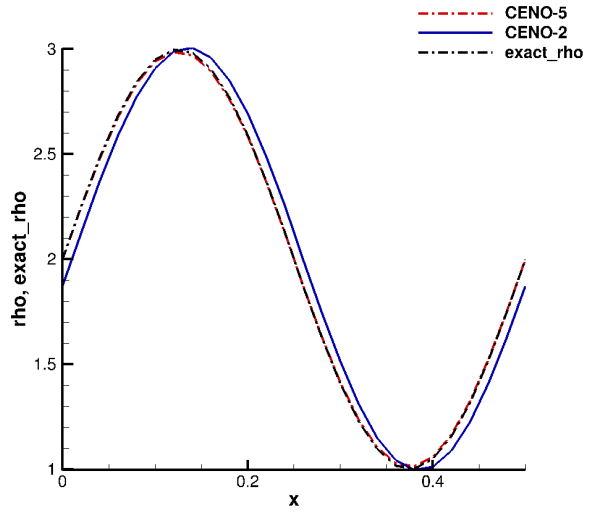

Figure 3.10: Comparison of final wave shape after one full period for second-order and fifth-order spatial scheme

Figure 3.10, the predicted results of the standard second-order scheme and a fifth-order scheme showing that the high-order scheme provides a better representation of the solution after one full period of simulation, recovering the initial wave shape as expected. This simulation is a one-dimensional problem simulated in a three-dimensional domain, allowing the testing of the generic hexahedral. The numerical results presented in Figures 3.11(a) and 3.11(b) demonstrate that the same solutions are obtained for both Cartesian and generic hexahedral meshes, indicating the correct behaviour for the generic hexahedral treatment with the trilinear transformation was achieved. Ivan *et al.* [2] have also shown that the desired orders of accuracy (up to 4^{th}) can be

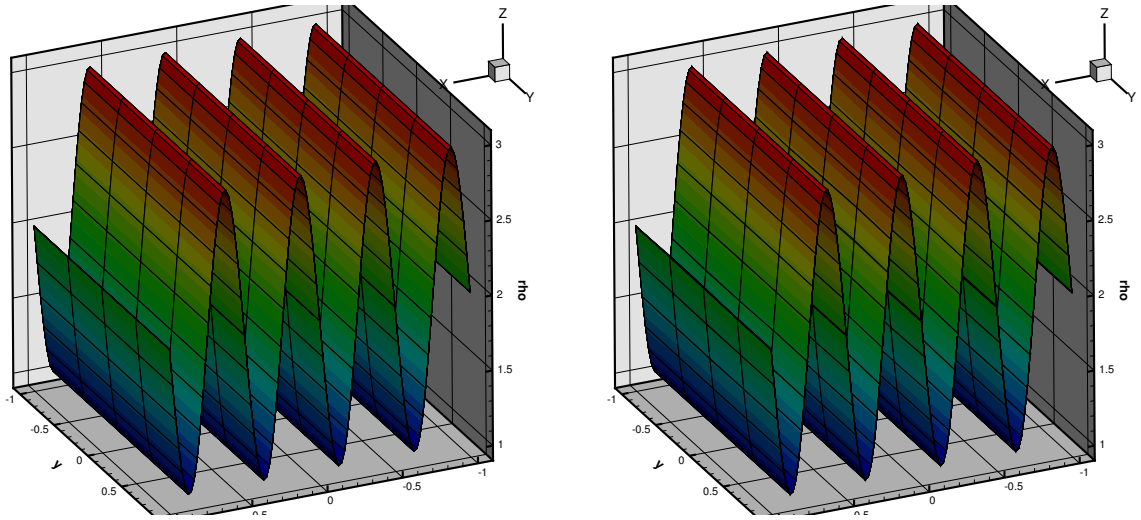

(a) Fifth-Order CENO on a Cartesian mesh - solution after one full cycle (20ms) - 100 elements in x-direction

(b) Fifth-Order CENO on a hexahedral (disturbed) mesh - solution after one full cycle (20ms) - 100 elements in x-direction

Figure 3.11: Contour plot of a sinusoidal density wave travelling in x-direction at constant speed u =100 m/s. Comparative demonstration of solution using hexahedral and Cartesian cells.

obtained for this case.

3.5.3 Non-Reactive Inviscid Flow — Shock-Cube Problem

The high-order CENO scheme, in particular the actuation of the smoothness indicator, is further verified through application of the scheme to an inviscid three-dimensional shock-box problem in which both both uniform Cartesian and distorted hexahedral computational mesh were considered. The problem is a generalization of the one-dimensional shock-tube problem for a 1 m$\times$1 m$\times$1 m three-dimensional domain. In this case, for $x \leq 0$, $y \leq 0$, $z \leq 0$, the solution is initialized to an initial state defined as

$$\begin{aligned} \rho_l &= 1.225 \text{ kg/m}^3 \,, \\ u_l &= v_l = w_l = 0 \text{ m/s} \,, \\ p_l &= 101.325 \text{ kPa} \,, \end{aligned} \tag{3.65}$$

and the remainder of the domain is initialized to a high-density, low-pressure state, defined as

$$\begin{aligned} \rho_r &= 9.8 \text{ kg/m}^3 \,, \\ u_r &= v_r = w_r = 0 \text{ m/s} \,, \\ p_r &= 1,013.25 \text{ kPa} \,. \end{aligned} \tag{3.66}$$

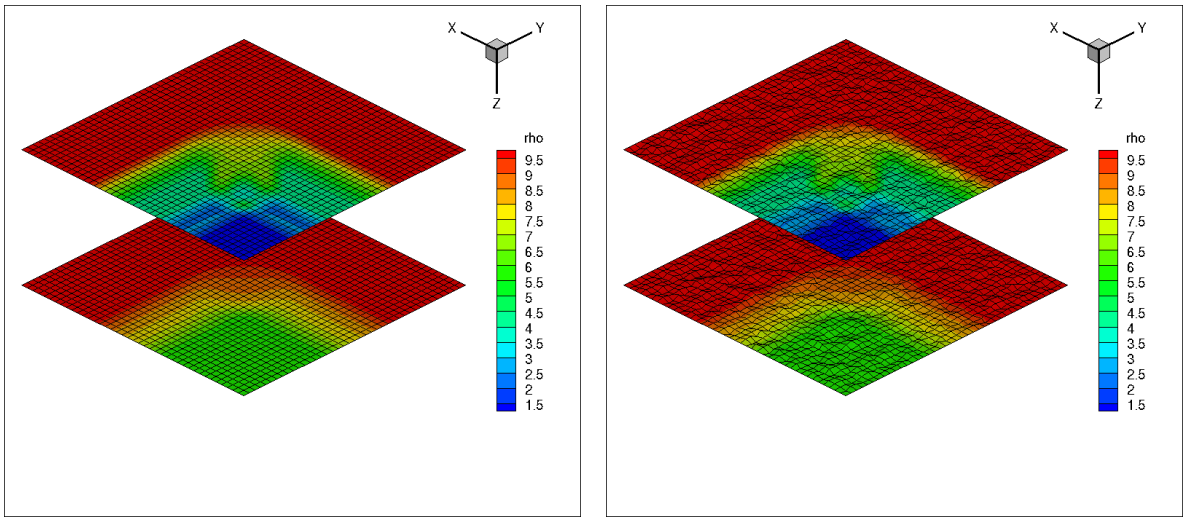

(a) Fifth-Order CENO on a Cartesian mesh (b) Fifth-Order CENO on distorted hexahedral mesh

Figure 3.12: Density variation for the shock-box problem shown on selected cut planes in the domain: $t = 0.5$ ms, 40^3 grid.

The simulation is allowed to progress for 0.5 ms. This time is sufficient to allow the propagating waves interact with each other, but for not enough time to allow the waves to travel beyond the boundaries of the solution domain.

Figures 3.12(a) and 3.12(b) show the corresponding density variation on two cut planes of constant z coordinates for both the Cartesian and disturbed hexahedral mesh. Additionally, Figures 3.13(a) and 3.13(b) depict the regions that are flagged (in red) by the smoothness indicator. They correspond to regions of the solution having under-resolved or discontinuous features on both meshes. This case demonstrates the shock capturing capabilities of the CENO scheme, and provides support for its correct implementation.

3.5.4 Non-Reactive Viscous Flow — Decay of Isotropic Turbulence

In order to provide an initial verification of the high-order implementation of the viscous fluxes for the proposed CENO scheme using LES before preceding to the reactive flow cases, the decay of a three-dimensional homogeneous isotropic turbulence field in the non-reactive case was first considered here. It should be noted that the rate of decay of the isotropic turbulence at relatively high Reynolds numbers is expected to be proportional to $t^{-1.25}$, according to both experiments and DNS results [171]. A 2π m $\times$ 2π m $\times$ 2π m solution domain was considered and an isotropic turbulence field was introduced, following the methodology presented by Rogallo [172]. The boundaries of this solution domain are assumed to be periodic in all directions. Following other previous grid convergence studies [24, 173], the turbulence decay was evaluated using two grid

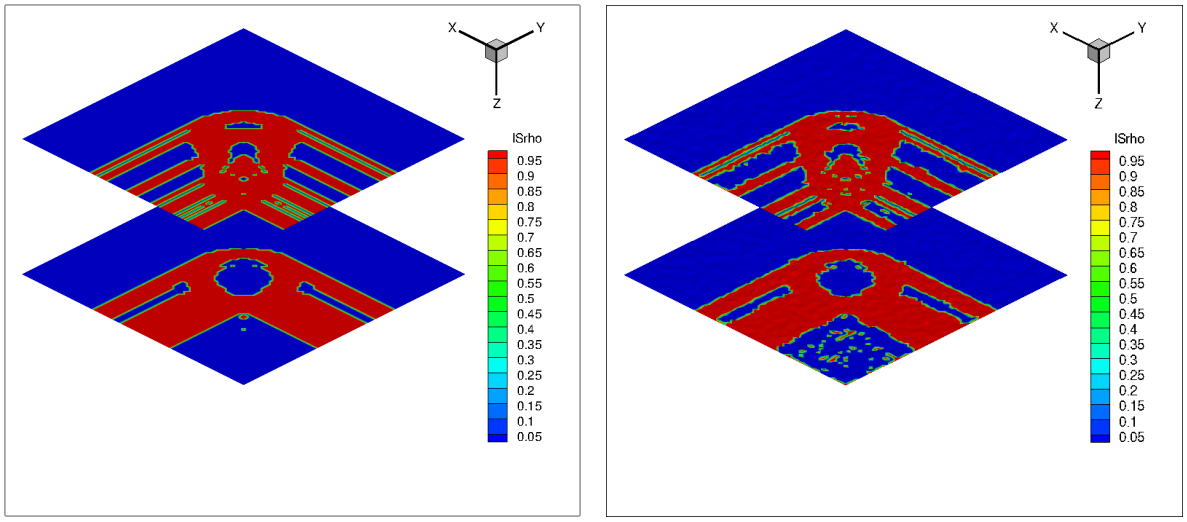

(a) Cartesian mesh (b) Hexahedral mesh

Figure 3.13: Contours of smoothness indicator for variable ρ flagging the discontinuities in the solution which shall be solved by the reduced order scheme to enforce monotonicity

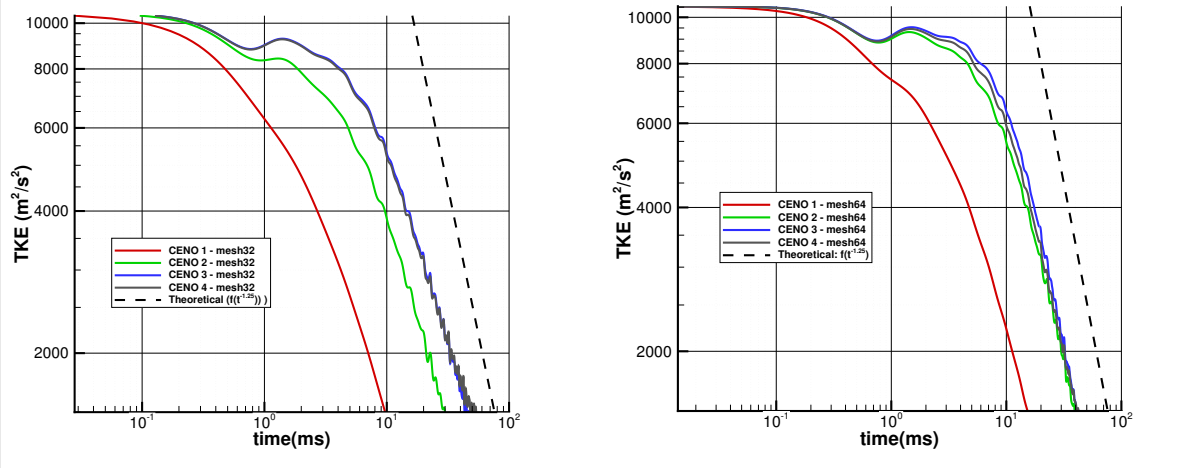

(a) Decay of Turbulent Kinetic Energy on $(32\times32\times32)$ mesh for several spatial discretization schemes (b) Decay of Turbulent Kinetic Energy on $(64\times64\times64)$ mesh for several spatial discretization schemes

Figure 3.14: Comparison of the Decay of Isotropic Turbulence using the high-order implementation of the viscous fluxes

sizes comprising of $(32\times32\times32)$ cells and $(64\times64\times64)$ cells. The Smagorinsky SFS model[174] was used in the non-reactive simulations with a Smagorinsky constant, C_S=0.1.

The LES results presented in Figures 3.14(a) and 3.14(b) show the predictions of the decay of the isotropic turbulent field within the domain as obtained by the proposed CENO finite-volume scheme on the two meshes. Results are presented for various orders, without monotonicity

enforcement, so as to highlight the effect of the increasing order of accuracy of the scheme on the preservation of turbulent content within the domain.

It can be seen that for both the $(64 \times 64 \times 64)$ and the $(32 \times 32 \times 32)$ meshes the solution for the different spatial schemes (2^{nd}, 3^{rd} and 4^{th}-orders) evolve to a similar turbulent kinetic energy decay rate, matching the expected theoretical rate shown with the black dashed lines. This can be interpreted as a verification of the gradient calculations and the other operations pertaining to the high-order viscous flux evaluations.

For both meshes, and more visibly for the coarse $(32 \times 32 \times 32)$ mesh, it can be seen that the third- and fourth-order CENO schemes hold the turbulent content for longer time, than the first- and second-order schemes. This also matches the expected behaviour, since the higher-order spatial schemes are showing a less dissipative behaviour than the lower-order schemes.

By comparing the results in the $(64 \times 64 \times 64)$ mesh with the results of the $(32 \times 32 \times 32)$ it can be seen that the achievement of the asymptotic decay rate is delayed in time for all the schemes, also bringing the second-order scheme curve closer to the third- and fourth-order schemes. Consistent with the expectations, both mesh refinement and the increase in spatial order of accuracy are contributing to the longer preservation of the turbulent content in the domain by reducing the numerical dissipation.

Chapter 4

LES Results for Premixed Flames

As discussed in the introductory chapter, this thesis represents the first application of the proposed high-order CENO scheme to the LES of premixed laboratory flames. The flame selected for the numerical studies performed here is a laboratory Bunsen-type flame studied in previous experimental work by Yuen and Gülder [3]. Several flames for this burner geometry have also been considered in other numerical studies [104, 68, 88, 120] using the same computational framework used here, except with second-order temporal and spatial discretizations. A brief description of the experimental results used here for comparison is first provided. The chapter then follows with a description of the numerical setup used for the cases studied. The metric used for comparison of the numerical prediction with experimental results is defined and the LES results are organized and presented in sets containing the solution obtained for different meshes using each discretization scheme. An analysis of the results is made by evaluating and comparing the difference between the numerical and the experimental results for the flame height for both low- and high-order schemes.

4.1 Description of the Experimental Setup

The experimental data considered in the present work as a reference for the assessment of the high-order LES simulations were obtained by Yuen and Gülder [3] using an axisymmetric Bunsen-type burner that has a 11.2 mm diameter burner nozzle, with an annular pilot flame. The available experimental data for the flame temperature and flow velocity were obtained using Rayleigh scattering and particle interference velocimetry (PIV) measurements. A schematic representation of the experimental equipment and setup is shown in Figure 4.1.

While a range of premixed flames are considered by Yuen and Gülder [3], the particular premixed flame studied in this work is a lean methane/air mixture with an equivalence ratio of ϕ=0.7.

The turbulent characteristics of the inflow are summarized in Table 4.1. By directly plotting the values for Λ/δ_L and u'/s_L for this case in the premixed flames diagram presented in Figure 2.2, it can be seen that this flame lies just above the flamelet regime in the thin-reactions zone, making it a somewhat challenging case to consider. This diagram is replotted and shown in Figure 4.2, including the experimental point of interest here in red.

4.2 Mesh and Numerical Setup

Information concerning the different meshes used here in the LES of the lean premixed methane-air flame of interest are presented in Table 4.2. In this study, a minimum of 3 meshes (A, B and C) were used for each order of the spatial schemes considered (second-, third- and fourth-order CENO schemes). For the standard second-order spatial scheme, a fourth refinement level for the mesh was considered which included more than 6.5 million (6,553,600) hexahedral elements

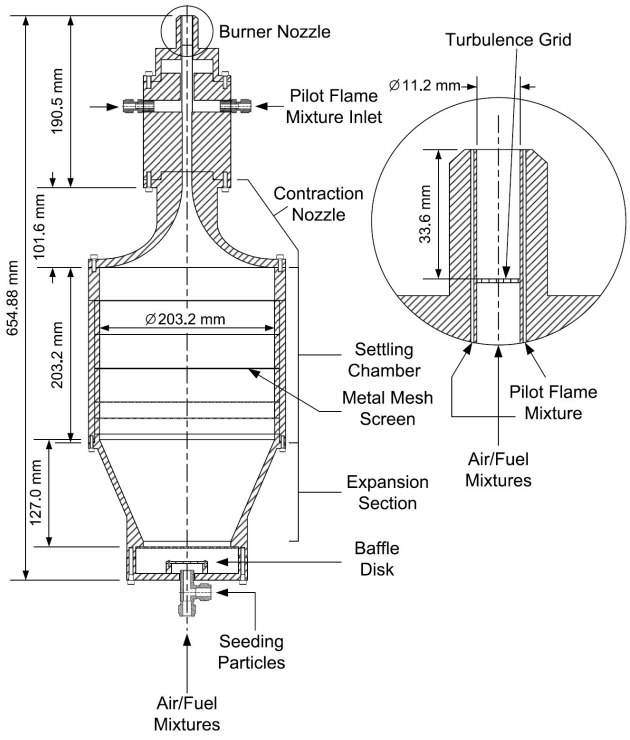

Figure 4.1: Experimental apparatus of Yuen and Gülder [3].

ϕ	Λ	λ	η	u'	s_L	δ_L	u'/s_L	Λ/δ_L
	mm	mm	mm	m/s	m/s	mm		
0.7	1.790	0.460	0.02935	2.92	0.201	0.11	14.38	16.64

Table 4.1: Summary of turbulence scales and flow conditions for case N

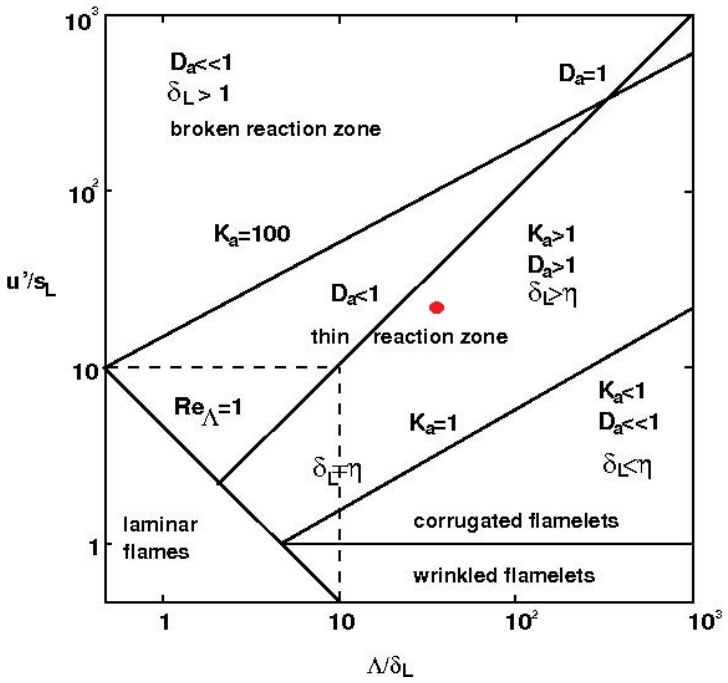

Figure 4.2: Premixed turbulent combustion regime diagram, as appearing in Peters [1] showing the experimental condition of interest here in red.

mesh	$N_{cells,blk,i}$	$N_{cells,blk,j}$	$N_{cells,blk,k}$	Total Cells	Mesh Alias
A	8	8	8	204800	coarse
B	4	4	4	691200	medium
C	6	6	6	1638400	fine
D	16	16	8	6553600	finest

Table 4.2: List of meshes used

(mesh D). Each of the mesh was a structured multi-block hexahedral grid in which the number of blocks is kept constant for all the meshes and the increased refinement was achieved by changing the number of cells per block. A total of $N_{blk,i} \times N_{blk,j} \times N_{blk,k}$ =3200 blocks are used in each case. When combined with a varying number of cells per block, this produced the 4 meshes with increasing resolution summarized in Table 4.2.

For each of the meshes described above, the cylindrical shaped computational domain used to represent the burner and flame was discretized as a cylindrical multi-block mesh with diameter of 0.05 m and a height of 0.1 m. In Figures 4.3(a) (YZ plane cut) and 4.3(b) (XY plane cut) the blocking structure of the mesh is shown, depicting the O-grid structure in the transversal plane and the use of non-orthogonal blocks.

The average mesh length, h, for the four grids was computed as $h = (h_x h_y h_z)^{1/3}$ and the filter width, Δ, was calculated as $\Delta = f_{\mathrm{FGR}} h$. A baseline value of f_{FGR}=2 was used for mesh C

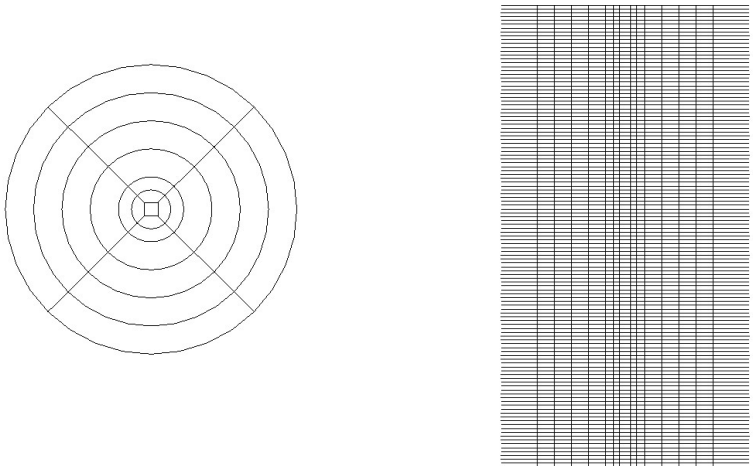

(a) Mesh - XY Plane cut (b) Mesh - YZ Plane cut

Figure 4.3: Transversal and longitudinal cuts showing the block structure used for meshing the Bunsen Burner flame

(fine), following the suggestions of Shahbazian *et al.* [68] and Hernàndez-Pérez *et al.* [88] in which the same burner and flame was considered. A fixed filter-width is adopted for all the meshes by changing f_{FGR} as a function of the average element size accordingly. The respective values of f_{FGR} used for each mesh are reported in Table 4.3. One particular set of results using the second-order spatial scheme was also generated using varying filter width (keeping f_{FGR}=2 for all the meshes) and the pertinent discussions are given in Section 4.4.6 below.

4.2.1 Summary of LES Simulations

All of the LES computations were performed using an explicit Runge-Kutta time marching scheme with second-order (RK2) or fourth-order (RK4) formulations, depending on the case. Three different spatial discretization schemes were examined: a second-order scheme based on limited, linear reconstructions (LLR), a third-order spatial scheme using CENO (CENO3) and a fourth-order spatial scheme using CENO (CENO4). For the CENO3 and CENO4 simulations a contracted two-layer, central stencil with 56 neighbours was used. The modified laminar flame based PDF (MLPDF) of Jin *et al.* [127] is chosen for use with the FPI tabulation in all the studies presented here, as explained in Chapter 2. In the present study, the FPI tabulation utilized 155 points in the progress variable space for most of the cases and a sensitivity test was done using a smaller table with 61 points. Table 4.3 provides a complete summary of each of the LES simulations performed for the Bunsen flame in this study, listing the simulation or case name, the mesh size, the time and spatial discretization scheme, the size of the FPI table and the filter-to-grid ratio used for each case. The case names have been chosen to help

identify the key parameters used for each simulation. The cases are named using a standard string: LES-**M**-**ST**-fgr**F**. The bold faced variables, **M**,**S**,**T** and **F** stand for the value of each key parameter. Variable **M** represents the respective mesh used for the case (mesh A, B, C or D). Variable **S** corresponds to the order of the spatial discretization scheme (**S**=2 for the LLR scheme, **S**=3 for the CENO3 scheme and **S**=4 for the CENO4 scheme). Variable **T** corresponds to the order of the time discretization scheme (**T**=2 for RK2 and **4** for RK4). Variable **F** is a number representing the filter to grid ratio used for that particular case. As an example, the LES-A-42-fgr1 case utilizes mesh A, was run with the CENO4 spatial discretization scheme, a RK2 time-marching scheme and the filter to grid ratio used was f_{FGR}=1.

The LES setup used here for the initial and boundary conditions for the lean premixed flame follows those previously used in similar studies for the same flame and operating conditions studied here [111, 69]. The turbulent inflow at the exit of the burner nozzle is modelled here as an uniform inflow profile of reactants superimposed onto a homogeneous isotropic turbulent field. The inflow homogeneous isotropic turbulent field was pre-generated using the procedure of Rogallo [172] and using the turbulent spectrum of Haworth and Poinsot [175]. The turbulence field is generated to match the value of turbulence intensity, u', and integral length scale, from the experiments. This procedure for specifying the inflow turbulence has been previously tested and validated for the flame of interest [69]. The axial inflow is modelled as a subsonic inflow at the inlet and subsonic outflow (fixed pressure) at the top and side of the cylinder. The pilot flame is represented by a uniform inflow of combustion products for the given equivalence ratio, in

CASE	CASE NAME	MESH	MESH SIZE	TIME	SPATIAL	FPI	f_{FGR}
1	LES-A-22-fgr1	A	204800	**RK2**	**LLR**	155	1
2	LES-B-22-fgr1p5	B	691200	**RK2**	**LLR**	155	1.5
3	LES-C-22-fgr2	C	1638400	**RK2**	**LLR**	155	2
4	LES-D-22-fgr3.2	D	6553600	**RK2**	**LLR**	155	3.2
5	LES-A-44-fgr1	A	204800	**RK4**	**CENO4**	155	1
6	LES-B-44-fgr1p5	B	691200	**RK4**	**CENO4**	155	1.5
7	LES-C-44-fgr2	C	1638400	**RK4**	**CENO4**	155	2
8	LES-A-42-fgr1	A	204800	**RK2**	**CENO4**	155	1
9	LES-B-42-fgr1p5	B	691200	**RK2**	**CENO4**	155	1.5
10	LES-C-42-fgr2	C	1638400	**RK2**	**CENO4**	155	2
11	LES-A-32-fgr1	A	204800	**RK2**	**CENO3**	155	1
12	LES-B-32-fgr1p5	B	691200	**RK2**	**CENO3**	155	1.5
13	LES-C-32-fgr2	C	1638400	**RK2**	**CENO3**	155	2
14	LES-A-22-fgr2	A	204800	**RK2**	**LLR**	155	2
15	LES-B-22-fgr2	B	691200	**RK2**	**LLR**	155	2
16	LES-D-22-fgr2	D	6553600	**RK2**	**LLR**	155	2
17	LES-B-42-fgr1p5-ngqp1	B	691200	**RK2**	**CENO4**	155	1.5
18	LES-B-42-fgr1p5-rt	B	691200	**RK2**	**CENO4**	61	1.5

Table 4.3: List of cases run including the spatial and time scheme used

the annular region from the Bunsen-burner nozzle to the external diameter of the domain. The domain is initialized with a constant pressure field and the burner and pilot inflow conditions. A laminar flame profile is assumed in the beginning of the calculations, located at the external diameter of the nozzle. The simulations are run for a simulation time of $t = 9$ ms, sufficient to reach a stabilized flame height (a quasi-steady flame was achieved for 5 ms $\leq t \leq$ 9 ms).

4.2.2 Predictions of Instantaneous Flame Structures

Some preliminary insights into the LES for the lean premixed flame of interest are obtained by analysing the predictions of instantaneous flame structures of some key parameters of the flow.

In Figures 4.4(a) and 4.4(b), instantaneous contours of the temperature field in the flame are shown for the second-order spatial discretization scheme (Case 1, LES-C-22-fgr2 and for the fourth-order spatial discretization scheme (Case 7, LES-A-44-fgr2), respectively. These contours were evaluated at a simulation time of $t = 9$ ms, when the simulated flames had reached a quasi-steady state behaviour. Both LES results were obtained with the same mesh (mesh C, fine). It can be clearly seen that the high-order scheme yields a shorter flame than that of the second-order scheme flame. This observation is also illustrated in instantaneous isosurfaces of the progress variable shown in Figures 4.5(a) and 4.5(b), where it can be seen that the high-order scheme provides a flame that evolves more rapidly towards the fully burned stages. A flame wrinkling characteristic of turbulent flames is also recognizable in these plots. Particularly, the higher-order scheme also provides a thinner, hotter flame in the upper half region of the plots. In the next sections, a more quantitative analysis is provided comparing the behaviour of the different discretization schemes for the meshes of interest.

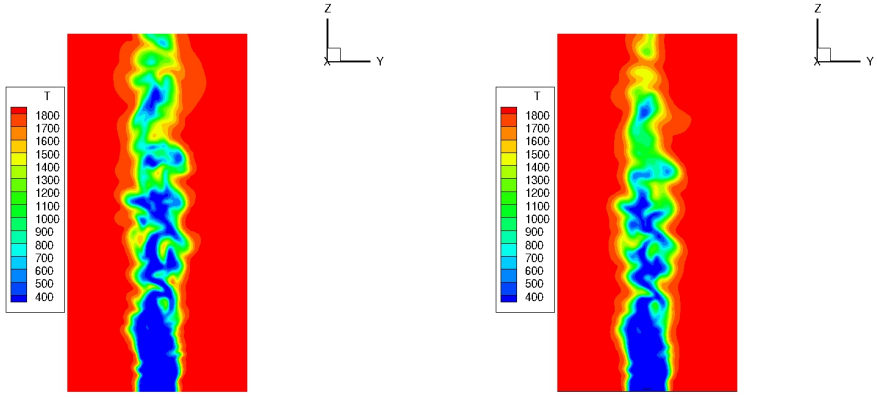

(a) Case 1, LES-C-22-fgr2 (b) Case 7, LES-C-44-fgr2

Figure 4.4: Instantaneous temperature contours at mid plane for second and fourth-order spatial discretization schemes

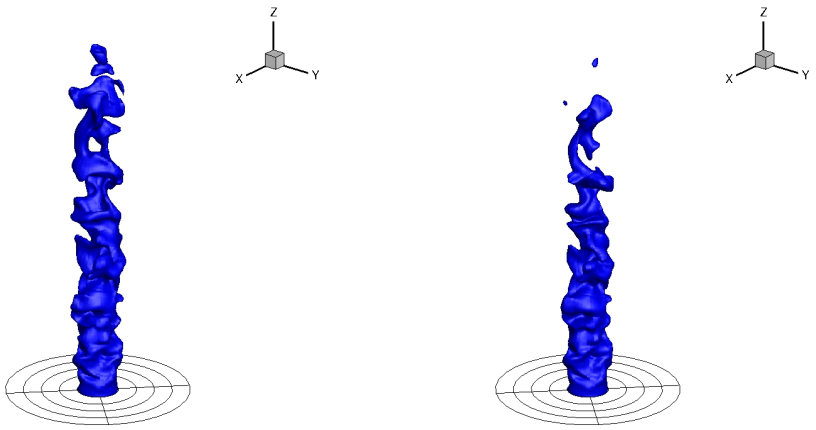

(a) Case 1, LES-C-22-fgr2 (b) Case 7, LES-C-44-fgr2

Figure 4.5: Instantaneous isosurfaces of the progress variable for second and fourth-order spatial discretization schemes at at a simulation time of $t=9$ ms

4.3 Predicted Contours of Averaged Progress Variable

A flame height for the Bunsen-type premixed, H, can be defined based on the time-average of two-dimensional profiles of the progress variable contours. In Figure 4.6, experimentally measured values of the time averaged progress variable contours based on the temperature is shown. The progress variable based on the temperature field is defined as:

$$c = \frac{T - T_{\mathrm{u}}}{T_{\mathrm{b}} - T_{\mathrm{u}}}\,, \tag{4.1}$$

where T, T_{u}, and T_{b} are respectively the local, unburned, and burned gas temperatures. The actual range of experimental measurements was confined to the upper regions of the flame above the burner due to reflections from the burner. However, the limits of the experimental contour plot presented here were adjusted to match those that are used for the numerical results, which consider the whole numerical domain. This is done to allow for a better visual comparison of the results.

Estimates of the flame height based on the progress variable contours criteria has been adopted previously by Hernàndez-Pérez [69] and Shahbazian *et al.* [111] in their simulations of premixed flames. The flame height is an attractive metric for assessing the LES predictions since it is directly related to the turbulent burning rate or fuel consumption, where a higher burning rate is associated with a shorter flame and vice-versa. In the present work, three different contours for the normalized progress variable, c=0.3, c=0.4 and c=0.5 are used in the characterization of the flame height.

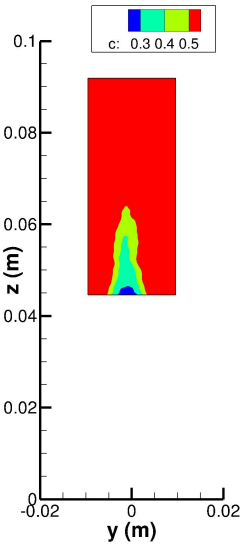

Figure 4.6: Experimental contours of the progress variable.

For the numerical results, the simulations were run until the time varying solution achieves a quasi-steady behaviour. Snapshots were taken separated by a 0.25 ms interval, after the burning rate had reached a quasi-steady within $t=5$ ms to $t=9$ ms. A sensitivity analysis of the resulting flame height predictions to this procedure was performed by studying the variation of the flame height to the number of snapshots used in the time averaging of the progress variable data for one of the cases studied (Case 2, LES-B-22-fgr1.5, mesh B, medium refinement). In Figure 4.7, it can be seen that the flame height exhibits little variation with increasing number of slices ranging from 10-25. Based on these findings a total of 13 slices was selected and used for all cases presented here. This number is considered to be appropriate for the comparative purposes of this study.

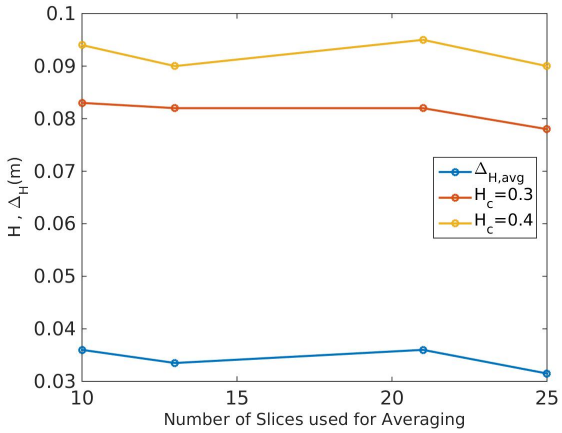

Figure 4.7: Variation of the flame height by varying the number of slices used for averaging

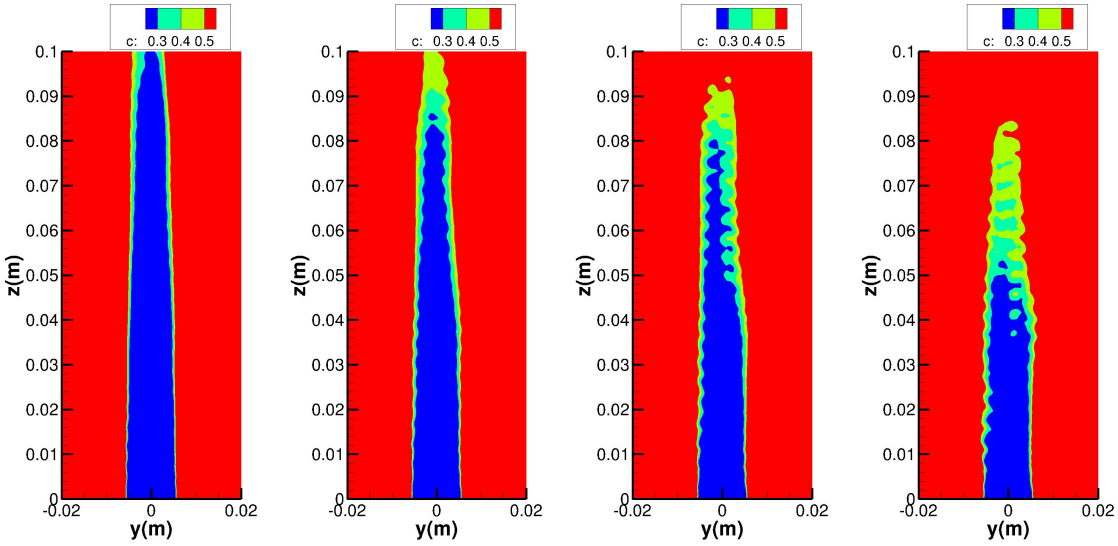

(a) Case 1 - coarse (b) Case 2 - medium (c) Case 3 - fine (d) Case 4 - finest

Figure 4.8: Normalized progress variable contours for 2nd order spatial scheme (LLR) with second-order discretization in time (RK2)

Having established the procedure for time averaging of the progress variable, the predicted LES results can now be examined. In Figure 4.8, the normalized progress variable contours are shown for the second-order spatial discretization scheme (LLR) using a second-order time marching procedure (RK2) for different meshes. It can be seen from these plots that for the coarsest mesh (Figure 4.8(a)) the higher contours (c=0.4 and c=0.5) are actually not represented properly within the domain and only the lowest contour, for c=0.3, is visible in the domain. The next three figures show a progressively lower flame, as the mesh is refined, remembering that for this second-order case a *finest* mesh (mesh D) is also considered.

A similar set of results of contours are generated for the fourth-order CENO spatial scheme (CENO 4) using a fourth-order time marching (RK4) and are shown in Figure 4.9. Starting with Figure 4.9(a), it can be seen that even for the coarse mesh the three selected contours can be represented within the computational domain, showing a much shorter flame than that observed in Figure 4.8(a) for the same mesh but with the standard second-order spatial scheme. The progressively refined meshes B and C, presented in Figures 4.9(b) and 4.9(c) respectively, show a lowering of the flame heights as expected. These flames are also significantly lower than the flames obtained with the second-order spatial scheme for the same meshes B and C (Figures 4.8(b) and 4.8(c) respectively).

Moving to the next set of results, generated using the fourth-order spatial scheme (CENO4) and a second-order time marching scheme (RK2), the same expected trend is observed. In Figure

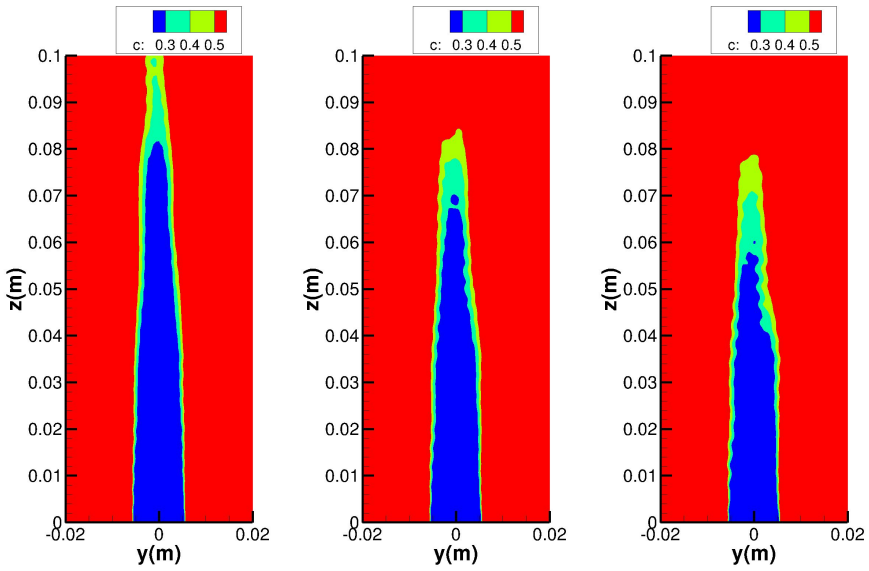

(a) Case 5 - coarse (b) Case 6 - medium (c) Case 7 - fine

Figure 4.9: Normalized progress variable contours for 4^{th} order spatial scheme (CENO4) with fourth-order discretization in time (RK4)

4.10 the decreasing flame height with increased mesh resolution is represented. Particularly it can be seen that the predicted contours of the progress variable are extremely similar to those obtained for the RK4 time marching scheme with the same spatial discretization. By directly comparing Figures 4.10(a) with 4.9(a) some slightly different details are noted in the top of the c=0.4 contours. When moving to the solutions obtained for the finer meshes B and C, represented in figures 4.10(b) and 4.10(c), respectively, the differences between the predicted contours of the progress variable on the same meshes obtained with the second- and fourth-order time marching are even less noticeable. It would seem that the LES solutions for the average flame height obtained using the RK4 and RK2 time marching schemes are practically identical, indicating that spatial accuracy may be more important than temporal accuracy, where the time step is related via Courant condition to the mesh spacing, for the flame and geometry of interest.

A fourth set of results is presented, for the same three meshes studied with the fourth-order spatial scheme, but now using a third-order CENO spatial scheme (CENO3), combined with a second-order time marching scheme (RK2). The predicted contours for the study of the flame height for this scheme are given in Figure 4.11. The results obtained for the third-order spatial scheme also follow the same expected trend of decreasing heights with increased mesh refinement. Moreover, the results are also very similar to those obtained with the fourth-order spatial scheme. Visually, there are very few differences in the predicted contours of the progress variable on the

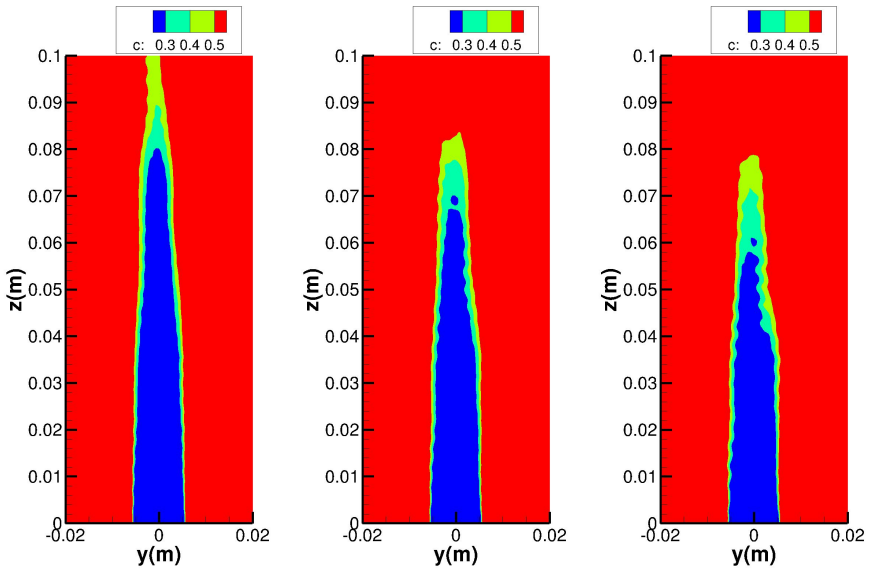

(a) Case 8 - coarse (b) Case 9 - medium (c) Case 10 - fine

Figure 4.10: Normalized progress variable contours for 4^{th} order spatial scheme (CENO4) with second-order discretization in time (RK2)

finest mesh as shown in Figures 4.11(c) and 4.10(c). From an engineering perspective, the predicted distributions of the progress variable are almost identical, the primary differences being well within the maximum accuracy that can be achieved by the visual inspection of the flame envelopes.

4.4 Analysis of the Predicted Flame Heights

A more quantitative assessment of the time-averaged LES results can be carried out by plotting the predicted flame heights obtained for each value of the normalized progress variable for each mesh and for each combination of spatial and time discretization studied above. All this data is compiled in the plots provided in Figure 4.12. The four figures on the left, figures 4.12(a), 4.12(c), 4.12(e) and 4.12(g), show the flame heights, H, as measured in the normalized progress variable contours as a function of $N^{1/3}$, where N is the total number of mesh elements. The progressively decreasing heights with increased mesh resolution are clearly represented for each set of result. More interesting than looking at the actual flame height, H, is to consider the difference, $\Delta_H = H_{num} - H_{exp}$, between the flame heights obtained numerically, H_{num}, and the experimental value of the flame height, H_{exp}, for each level of the normalized progress variable, c, studied here. These results are also plotted as a function of $N^{1/3}$, and are given in Figures 4.12(b), 4.12(d),4.12(f) and 4.12(h)). Interestingly, it can be noted that for each scheme,

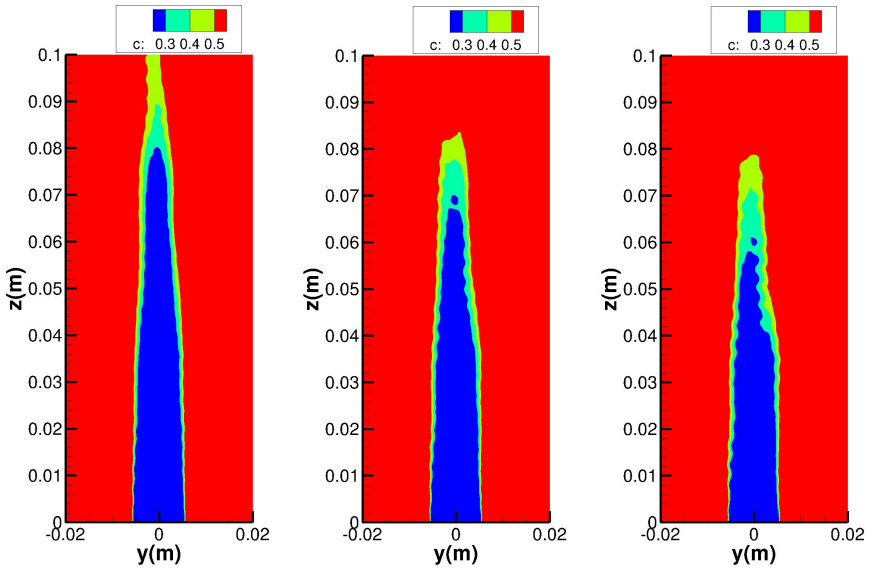

(a) Case 11 - coarse (b) Case 12 - medium (c) Case 13 - fine

Figure 4.11: Normalized progress variable contours for 3rd order spatial scheme (CENO3) with second-order discretization in time (RK2)

for a given mesh, the differences in flame height relative to the reference experimental values calculated for the three heights essentially collapse on each other within a range much smaller than the predicted flame heights. One objective way of analysing the trends verified here is to average the errors obtained for all the heights, for each mesh, producing a single metric as will be presented in the next section.

It can be seen from the plots of Figure 4.12 that the errors for the different values of the normalized progress variable collapse within a limited range. Also, despite presenting some fluctuations as the mesh is refined, in general the errors for all the three measured heights are reduced at similar rates with the progressive refinements. This suggests that a single metric, an average error, $\Delta_{H,avg}$, can be adopted for the comparison of the different methods. This average error relative to experimental result is defined as

$$\Delta_{H,avg} = \frac{\Delta_{H,c=0.3} + \Delta_{H,c=0.4} + \Delta_{H,c=0.5}}{3} \tag{4.2}$$

The values for $\Delta_{H,avg}$ can then be investigated as a function of the different mesh sizes and numerical schemes studied. This is represented in the plots given in Figure 4.13. Figure 4.13(a) shows the variation of the difference between the numerical and experimental average flame heights as a function of the number of elements of the mesh, N. It can be seen that the average error decays, presenting an asymptotic behaviour as the mesh becomes finer for all the schemes.

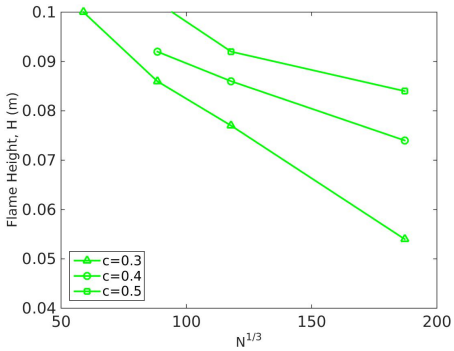

(a) Flame Height, LLR-RK2

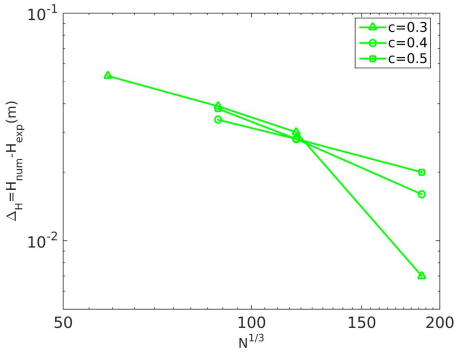

(b) Δ_H, LLR-RK2

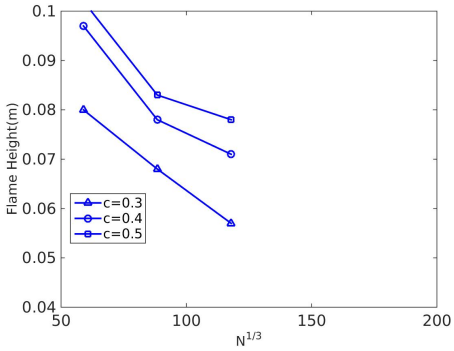

(c) H, CENO4-RK4

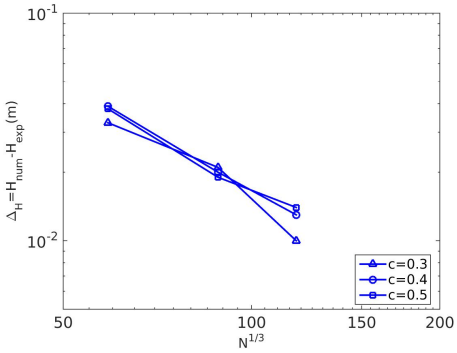

(d) Δ_H, CENO4-RK4

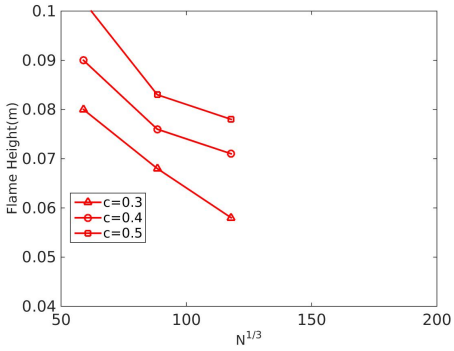

(e) H, CENO4-RK2

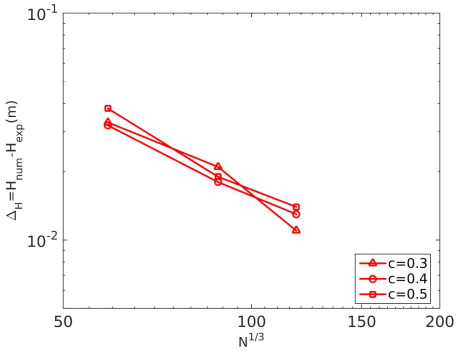

(f) Δ_H, CENO4-RK2

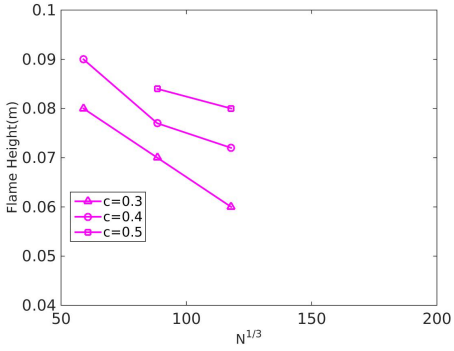

(g) H, CENO3-RK2

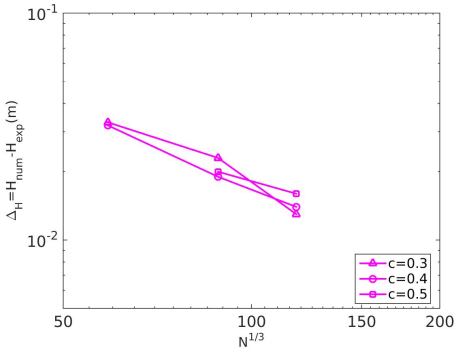

(h) Δ_H, CENO3-RK2

Figure 4.12: Flame height, H, and difference in flame height compared to Experiment (Δ_H), for different discretization schemes

For the particular case of the second-order spatial scheme, where the simulation of the mesh D (finest) was conducted, it can be seen that rapidly diminishing returns are realized with the progressive mesh refinement and less relative variation in the flame height is seen with the aggressive refinements between meshes C (fine) and D (finest) when compared with the very high variation obtained in the flame height when refining from mesh B (medium) to mesh C (fine).

In Figure 4.13(b), the values for $\Delta_{H,avg}$ are now plotted as a function of the cubic root of the total number of elements, $N^{1/3}$, which can be seen as the inverse of the average element length, or the actual spatial discretization scale of the scheme.

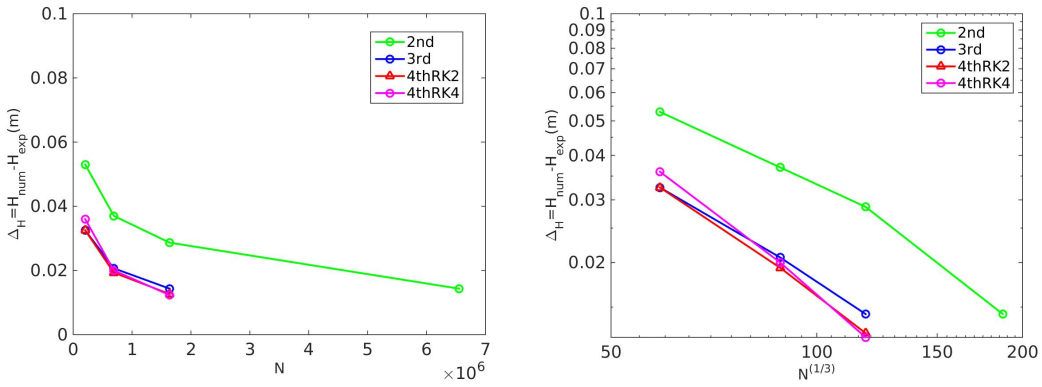

(a) $\Delta_{H,avg}$ as a function of total number of elements, N

(b) $\Delta_{H,avg}$ as a function of $N^{1/3}$

Figure 4.13: Average error in flame height compared to experimental results for different numerical schemes and mesh resolutions

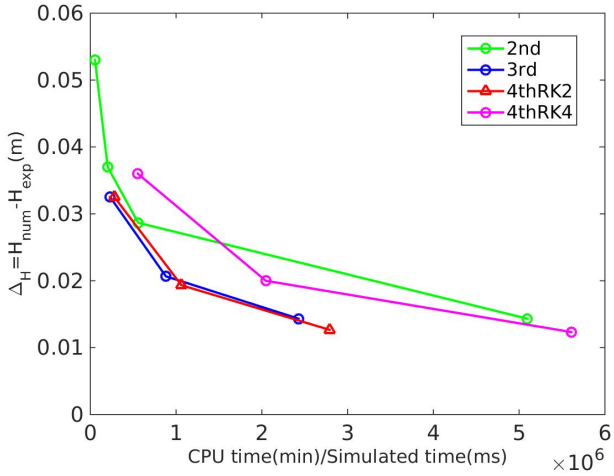

Figure 4.14: Average error in flame height as a function of computational cost

By comparing the absolute value of the error for the different schemes it can be seen that all the plots are presenting an asymptotic behaviour towards similar levels. It can also be seen that for a given mesh, the higher-order schemes (third and fourth-order) can provide a lower error (closer to the experiments) than the second-order scheme. For example, the high-order scheme provides on a mesh of only 1.6 million elements an average flame height that is only achievable with the second-order scheme for meshes larger than 6 million elements.

It is clear that the high-order schemes can provide a more accurate solution representation for a given mesh resolution but the computational cost per cell of the high-order scheme is also higher than the computational cost per cell of the second-order spatial scheme. The need for a more complex polynomial reconstruction and also the use of higher-order quadratures directly impose a significant computational overhead to the high-order scheme. A more complete understanding of the behaviour of high-order schemes is achieved when the error calculated for progressively refined meshes of each scheme is compared with the actual computational cost of obtaining the solutions.

Using the averaged flame height error (average of the differences between numerical and experimental for each contour level of c) as accuracy measure, the results shown in Figure 4.13(a) are now plotted against the actual cost of each simulation. The cost unit is represented in CPU time (in minutes) required to perform 1 ms of calculation. This re-scaling based on computational cost is shown in Figure 4.14. It can be seen that for a lower accuracy, for example, when the errors are of the order of 3 cm, the costs are similar, around 5 $\times 10^5$ cost units for all the schemes but the fourth-order in space and time, which is more costly. Nevertheless, for increasing accuracy, the high-order spatial discretization become more competitive and for errors around 1 to 1.5 cm, the CENO4 and CENO3 high-order spatial discretization schemes combined with second-order time marching scheme would provide the same average flame height of the second-order spatial scheme while requiring only about half of the computational cost.

4.4.1 Comparison of CENO4-RK4 and LLR-RK2 Results

The second-order spatial scheme with second-order time marching scheme is considered here to be the baseline result (green curve). By comparing this baseline with the predictions of the fourth-order spatial discretization with fourth-order time marching scheme (CENO4-RK4, magenta curve) the cost required for the same level of accuracy are actually comparable and not much advantage is achieved by the use of the high-order discretization in time and space. In fact, the magenta line (CENO4-RK4) does cross the green (LLR-RK2) line at around 1.5 $\times 10^6$ cost units. This suggests that at this point the high-order scheme would become more advantageous (lower error at lower cost). The two lines converge again towards each other for

further decreasing error, indicating that the two costs become actually comparable for very low error.

4.4.2 Comparison of CENO4-RK2 and CENO4-RK4 Results

In trying to isolate the effects of the high-order spatial discretization from those potentially arising from the high-order time-marching, the fourth-order spatial scheme with second-order time marching was also studied. These numerical LES results confirm some initial indications that, for the case studied here, the spatial discretization is playing a more significant role than the time marching discretization in the solution error. It was seen directly from the contours, which have been translated into the flame height predictions as a function of mesh size plots, that the results obtained for the fourth-order spatial scheme using a high-order time marching scheme were very close, if not virtually identical to those obtained with the fourth-order spatial discretization and a second-order time marching scheme. In the explicit type of time marching schemes that are used here, the costs of the second- and fourth-order (RK2 and RK4) schemes are directly proportional to the order of the scheme, since the fourth-order scheme requires twice the number of evaluations of the integrand functions for the integration in time. This effect of reduced cost with virtually no loss in solution quality is reflected in Figure 4.14 when comparing the magenta (CENO4-RK4) line with the red (CENO4-RK2) line, showing that the costs of the CENO4-RK4 is at less than half of that of the CENO4-RK2 scheme for the same given error.

4.4.3 Comparison of CENO4-RK2 and LLR-RK2 Results

Considering the fourth-order spatial scheme CENO4-RK2 (red line) compared with the second-order in space scheme LLR-RK2 (magenta line), Figure 4.14 shows that, for the cases studied here, using a fourth-order spatial scheme combined with a second-order time marching scheme is less costly than using the second-order in space and time scheme. Figure 4.14 shows that the two schemes are comparably efficient for errors up to around 3 cm. Below that, the CENO4-RK2 scheme starts to perform better, providing an averaged error at the 1-1.5 cm with approximately half of the cost of the LLR-RK2 scheme for this case.

4.4.4 Comparison of CENO3-RK2, CENO4-RK2, LLR-RK2 Results

Since the time marching scheme showed little influence for the results presented for the fourth-order spatial scheme, the runs with the third-order spatial scheme were performed using the second-order time marching scheme. From the contour plots, it was previously noted that the CENO3-RK2 scheme provides a very similar solution to those obtained with the CENO4-RK2 scheme. In the cost comparison plot, Figure 4.14, the CENO3-RK2 (blue line) follows the

CENO4-RK2 line almost exactly, with the differences being well within the visual accuracy of the height readings from the contour plots. This result is not so surprising in the sense that the implementation of the CENO3 scheme is actually very similar to the CENO4 scheme. The stencils used are of the same size, despite the number of unknown derivatives in the least-squares problem being lower for the CENO3 scheme. Also, the number of quadrature points is kept the same. The main difference between the two schemes becomes the actual reconstruction polynomial. This provides some computational savings associated with the third-order spatial scheme which reflects in a slightly lower cost for the same given mesh when compared to the CENO4-RK2 scheme. Consequently, the performance of the third-order spatial scheme in comparison with the second-order spatial scheme becomes comparable to the findings outlined previously for the CENO4-RK2 scheme and LLR-RK2 results.

4.4.5 CENO Fourth-Order - Parameter Variations

A sensitivity analysis is conducted for two parameters of the numerical method developed here. Having as a baseline Case 9, LES-B-42-fgr1.5, obtained using the CENO4-RK2 scheme on mesh B, one case was repeated with all the parameters fixed as in Case 9 but reducing the number of volumetric quadrature points to 1 point, instead of 8 points originally used for all the high-order cases (this originates Case 17, LES-B-42-fgr1.5-ngqp1). The other case also departs from Case

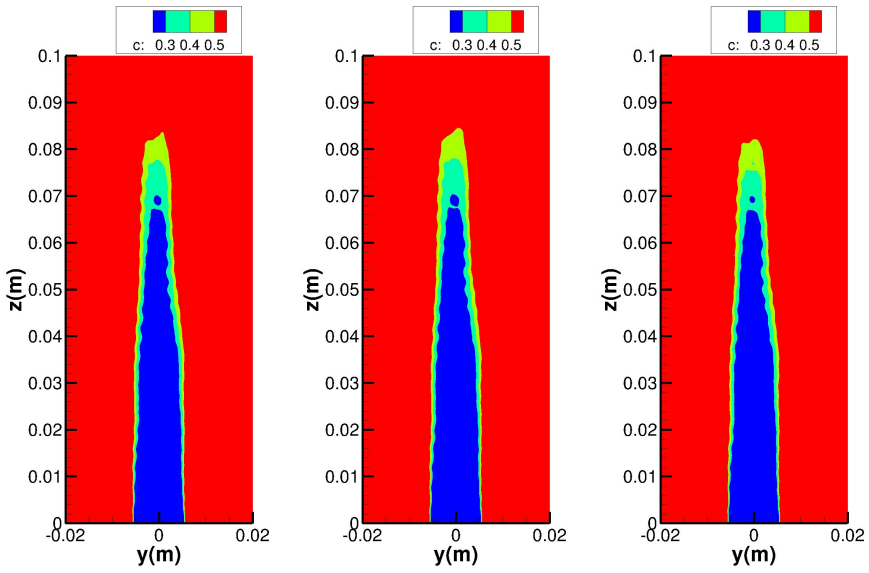

(a) Case 9 (b) Case 18 - Reduced FPI Table (c) Case 17 - Reduced volume quadrature points

Figure 4.15: Normalized progress variable contours for varying table size, and for reduced number of volumetric quadrature points

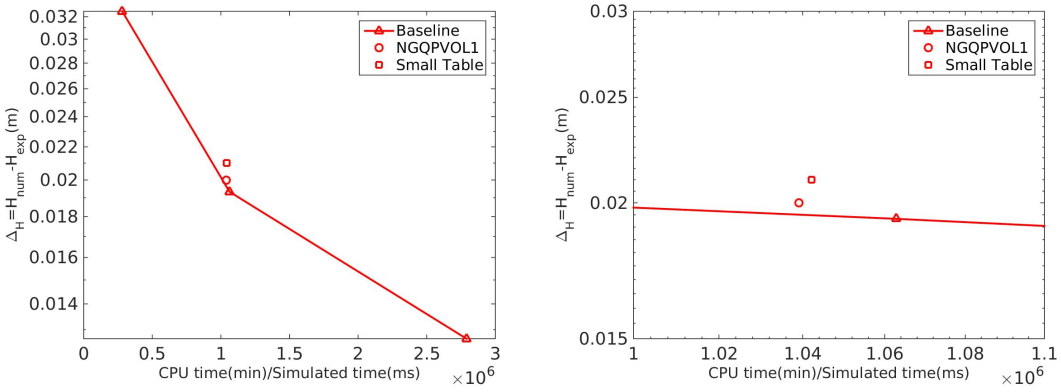

(a) $\Delta_{H,avg}$ vs. Computational cost (b) $\Delta_{H,avg}$ vs. Computational cost (detail)

Figure 4.16: Effect of parameters variation in cost

9 but now the sensitivity to the size of the FPI table is studied (this originates case Case 18, LES-B-42-fgr1.5-rt). The original FPI table discretizes the 1D laminar flame in 155 intervals. The reduced version of this table discretizes the 1D laminar flame in 61 intervals. In Figure 4.15 the contours for these three cases are depicted.

From these contours we can plot the average difference in flame height compared to the experimental results, and the results are plotted in Figure 4.16(a).

It can be seen that there is very little variation in the error between the three cases and the flame heights are well within the accuracy of interpolating the heights from the progress variable contours. It can also be seen that the effect of the table size is slightly more notable than the reduction of the number of volumetric quadrature points. The idea of adjusting the range of the plots aimed to emphasize the differences but it is important to highlight that these differences, however existing and showing the right trends, are recognized to be not quantitatively significant from an engineering standpoint.

4.4.6 Effect of the Filter-to-Grid Ratio

All the results presented previously used a fixed average filter width through all meshes by adjusting the filter-to-grid ratio accordingly to compensate for the different average element sizes for the meshes studied. Another set of results was generated for the second-order spatial scheme with second-order time marching but now using a fixed filter-to-grid ratio through all the meshes, therefore changing the effective filter-width with varying mesh resolution. This comparison is summarized in Figure 4.17.

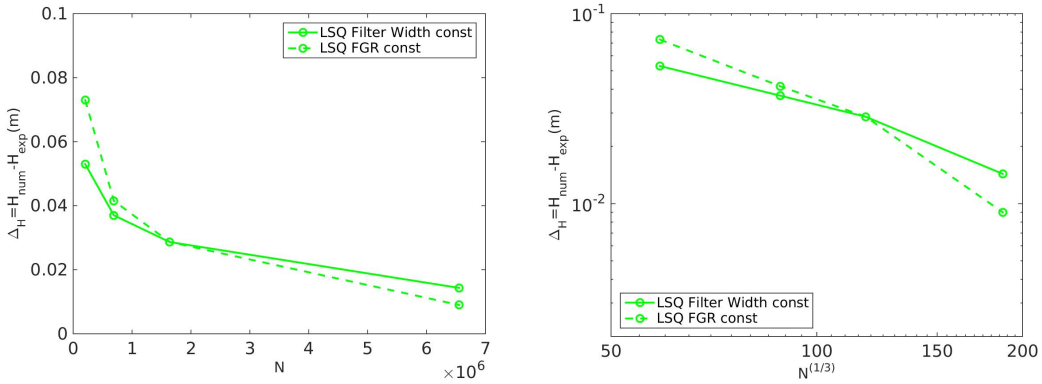

(a) $\Delta_{H,avg}$ as a function of total number of elements, N

(b) $\Delta_{H,avg}$ as a function of $N^{1/3}$

Figure 4.17: Average error in flame height compared to experimental results for different numerical schemes and mesh resolutions

Case	Mesh million elem.	time	spatial	f_{FGR}	Resolved TKE %
1	0.2	RK2	LLR	1.00	83.5
2	0.7	RK2	LLR	1.50	83.8
3	1.6	RK2	LLR	2.00	84.4
4	6.5	RK2	LLR	3.20	84.3
5	0.2	RK4	CENO4	1.00	83.4
6	0.7	RK4	CENO4	1.50	85.1
7	1.6	RK4	CENO4	2.00	85.2
8	0.2	RK2	CENO4	1.00	83.2
9	0.7	RK2	CENO4	1.50	85.1
10	1.6	RK2	CENO4	2.00	85.2
11	0.2	RK2	CENO3	1.00	82.9
12	0.7	RK2	CENO3	1.50	84.7
13	1.6	RK2	CENO3	2.00	85
14	0.2	RK2	LLR	2.00	57
15	0.7	RK2	LLR	2.00	75.1
3	1.6	RK2	LLR	2.00	84.4
16	6.5	RK2	LLR	2.00	93.2

Table 4.4: Percentage of resolved turbulence for each simulation

The baseline case, with the fine mesh (mesh C), with a a filter-to-grid ratio f_{FGR}=2, is kept the same for both sets of LES results. The filter-to-grid-ratio f_{FGR}=2 is used for all the points in the dashed green line. It can be seen that for the meshes coarser than mesh C the constant filter-to-grid ratio yields larger filters, therefore less resolved content and larger differences between numerical and experimental results than those obtained with the constant filter width (dashed line). The same effect is exhibited for the finest mesh (mesh D), but now the filter width in the

full green line is higher than the filter width used for mesh D in the dashed line. The dashed line is presenting a slower convergence, similar to a DNS-like behaviour since the filter width is also being reduced with the consecutive meshes of increasing resolution.

From Table 4.4 it can be seen that for all the sets of numerical results where the filter-width was held constant by varying f_{FGR} accordingly with increasing mesh resolution, the percentage of resolved turbulent kinetic energy (TKE) was almost constant and within typical LES ranges, at about 80-85%. This happened for LLR-RK2 (cases 1-4), CENO4-RK4(cases 5-7), CENO4-RK2(cases 8-10) and CENO3-RK2(cases 11-13). The effect of reducing the filter-width with finer meshes, by keeping f_{FGR} constant in the LLR-RK2 set (cases 14-16 and case 3), can also be assessed by analysing the data from Table 4.4. The percentage of resolved turbulence increases with increasing mesh refinement and decreasing filter-width. This demonstrates the trend towards a DNS-like solution, where 100% of turbulence would be resolved. A very small percentage of turbulence is being resolved on the coarse mesh in case 14 (57%), and a significant amount of turbulence (around 93%) is being solved for on the finest mesh in case 16.

Chapter 5

Conclusions

The importance of combustion science to our society is largely recognized. Ground, air and sea transportation, energy generation and several fields of the transformation industry are among the applications that heavily rely on combustion as means of transforming stored energy in fuels into usable energy. Combustion phenomena are very complex and involve, in the vast majority of practical applications, complex geometries, complex flows, and complex chemistry mechanisms. More restrictive environmental regulations and crescent efforts towards more sustainable energy conversion systems stimulate the need to study alternative fuel options, presenting additional challenges to combustion system developments. Numerical modelling can further assist the development of combustion devices and, along with experimental studies, can continue to contribute to a better understanding of combustion processes and new fuels. The costs associated with simulation of combustion flows, considering complex turbulence and chemistry interactions in complex geometries, involving a wide range of time-scales are usually very high. Efforts towards increasing the representativeness of numerical simulations of combustion flows and making these calculations more computationally affordable are of high interest.

In this thesis, the use of a high-order finite-volume formulation was investigated by extending the CENO finite-volume scheme to three-dimensional reactive flows. In order to deal with complex geometries, a block-based structured mesh using generic hexahedral elements, allowing non-planar faces was considered. To be able to simulate complex turbulent features, a LES approach was selected, combined with a chemistry model based on presumed conditional moments and precomputed tabulated chemistry using the FPI techniques, allowing to introduce elements of complex chemistry into the simulation.

The details of the physical modelling based on the Navier-Stokes equations for thermally perfect gases were presented along with the turbulence and chemistry modelling options. The resulting

filtered Navier-Stokes equations coupled with the PCM-FPI transport equations generate a set of partial differential equations for which the numerical method developed here was applied. The high-order CENO method uses a hybrid reconstruction approach based on a fixed central stencil. The discretization of the inviscid fluxes combines an unlimited high-order K-exact least-squares reconstruction technique based on the optimal central stencil with a monotonicity-preserving, limited, linear, reconstruction algorithm. Switching in the hybrid procedure is determined by a smoothness indicator such that the unlimited high-order reconstruction is retained for smooth solution content that is fully resolved and reverts to the limited lower-order scheme, enforcing solution monotonicity, for regions with abrupt variations (i.e., discontinuities and under-resolved regions). The high-order viscous fluxes are computed based on a K-order accurate cell interface gradient derived from the unlimited, cell-centered, reconstruction.

Preliminary verification results were presented for several non-reacting problems with the aim of testing different components of the implementation. Successful tests were performed for the reconstruction of smooth and non-smooth functions on Cartesian and generic hexahedral meshes. The implementation of the hyperbolic fluxes was tested by applying the method developed here to a wave propagation problem using generic hexahedral meshes and to a shock-tube problem where the performance of the smoothness indicator was tested. The decay of isotropic turbulence in a cubic domain was also tested, verifying the implementation of the high-order viscous terms.

In order to validate the whole framework for LES of reactive flows, the case selected was a laboratory turbulent premixed flame of methane/air for which extensive experimental results exist. The study presented concentrates on the application of the numerical method developed here to simulate the laboratory Bunsen-burner flame, comparing the performance of the new method with a baseline second-order accurate scheme. The metric used to evaluate the quality of the solution was to compare the flame-height as extracted from the normalized progress variable contours and measure an error (difference) between the values obtained numerically and the experimental results. The flame heights are determined for three different levels of constant progress variable and the errors for these three heights are averaged constituting a single metric. These averaged differences are computed for three different meshes for the high-order cases and for four different meshes in the second-order case. The results are compared based on the grid resolution and also based on the computational cost associated with each of these grid resolutions.

5.1 Findings of the Research

For the LES results for a premixed flame presented in this study, the following comments can be made:

1. The results obtained show that the high-order (both fourth and third order in space) methods provided a significantly more accurate description of the flame in comparison to the second-order method for a same given mesh, as indicated by the flame height measurements.

2. The fourth-order spatial discretization combined with a fourth-order time marching scheme provides better agreement with experimental results than the second-order spatial discretization with second-order time discretization. A mesh size reduction of about 4 times could be achieved for same accuracy using the fourth-order scheme. However, it did not present significant computational savings compared to the fully (space and time) second-order scheme, mostly due to the overhead of the expensive time marching scheme without notable benefits for this problem. This indicates that the efficiency of the current high-order implementation may need to be reconsidered and improved.

3. The combination of a second-order time marching scheme with the fourth-order spatial discretization provided very similar results to those obtained with the fourth-order discretization in time and space. This suggests that for this problem the time discretization errors were not dominant and the time evolution was sufficiently resolved with the second-order time marching scheme. Sources of lower-order information are still in use in the high-order formulation, as, for example, the linear interpolation of the tabulation and the use of a piecewise-linear reconstruction inherent to the high-order method in regions where the solution is non-smooth. These elements can influence the global error decreasing the formal order of accuracy of the method. The formal global order of the method can not be assessed with this particular case due to the lack of an exact mathematical solution to the problem. Nevertheless, it can be seen from the results presented herein that an asymptotic behaviour of the error in flame height used for all the schemes is clear, helping to support the use of this metric.

4. The error plots presented indicate that the fourth-order scheme combined with second-order time marching was able to provide significant cost savings when compared to the second-order spatial scheme, specially for very low levels of error. These are very encouraging results, indicating that the higher accuracy of the method benefited the final

solution process and the gains observed by having a better solution for the same mesh were translated into significant computational cost savings as shown in the error plots.

5. The use of a third-order spatial scheme combined with a second-order time-marching scheme showed very little to no deterioration in the quality of the solution when compared with the fourth-order spatial scheme. This fact is actually not so surprising if one remembers the way in which these schemes were tested: both of these methods use the same number of quadrature points and the same stencil with 56 neighbours. The only difference between the two formulations being the size of the reconstruction polynomial, which was smaller for the third-order scheme. However, the lower accuracy of the third-order polynomial had low impact in the final solution. Actually the effect of having a simpler reconstruction function in the third-order scheme reflected in a slightly lower computational cost for the third-order cases, basically compensating for the also small loss in accuracy of the result. Based on these tests it can be seen that the cost of the reconstruction itself is a relatively significant portion of the total cost, since this is the only significant difference between the third and fourth-order schemes. Further tests to explore these findings would include the use of the third-order scheme with a smaller stencil (using 26 neighbours to retrieve 20 derivatives in the reconstruction). Another idea is to try to use the same third-order scheme with only one quadrature point per face and see the effect in the cost. The accuracy of the quadrature would be lower but it would still be using a high-order reconstruction, so this could give interesting insights on which aspects of the high-order scheme are providing greater benefit to the final solution.

6. The sensitivity tests indicated very little influence of the number of volumetric quadrature points, both in quality of the result as in cost. The number of volumetric quadrature points affect properties that are pre-calculated (volumetric cell properties) and therefore does not influence the run cost. The source terms calculation is directly affected but does not seem to be a major cost component. This can be explained by recognizing that the source terms calculation requires 8 unlimited reconstructions (state and derivatives). The face quadratures, for the flux calculations, use 4 points per face and this was kept fixed for the calculations with 1 or 8 points per volume. The face calculations require, therefore, 4 reconstructions per face, per side of the face (left and right). These face reconstructions may also require limiting and a piecewise-linear reconstruction for the case of the inviscid fluxes. Also, the flux calculations are performed for 6 faces. This suggests that the face calculations are probably dominating the costs related to the right hand side evaluations. The little reduction in quality and cost by using a reduced FPI table do not justify pursuing it as a cost savings alternative for these cases.

7. The inflow turbulence intensity from the burner used in the numerical results presented was imposed as a top hat, uniform profile in the inlet boundary based on the turbulence intensity values measured close to the center of the nozzle. More recent experiments [176] with the same geometry have shown that the actual turbulence intensity profile is not actually uniform and due to the shear at the nozzle walls the turbulence levels present a peak at the outer-diameter of the nozzle. In this sense it is known that the turbulence intensity values used in the simulations presented here are lower than what was effectively present in the experiments. Sensitivity studies were performed assuming also a uniform profile but using a turbulence intensity level that accounts for the contribution of the peaks due to wall-shear. These studies indicated that an increase of about 30% in the total turbulent energy is achieved by accounting for the peaks contribution at the inlet and this would represent a decrease of about 10% in the computed flame heights. This increase in turbulent intensity would be expected to lower all the numerical flame heights presented with probably little effect to the comparative nature of the results presented here.

8. Considering a large scale problem, like the one studied, other benefits of using high-order formulation can be acknowledged. Despite being of relatively smaller importance if compared to the global cost of the calculation, the ability to obtain a more accurate solution with a coarser mesh using high-order formulation offers two other advantages compared to a low-order formulation: lower storage requirements and lower post-processing cost. For the case of the finest mesh used here, the averaging process during post-processing of the results can easily take a couple hours to be concluded, potentially half a day or a day if more slices were used. This post-processing time and the storage requirements scale linearly with the mesh size and may become significant specially when considering the analysis of multiple cases.

From the comments above it can be said that the implementation of the CENO scheme was successfully performed and evaluated. A reduction in mesh size of about 4 times was achieved for same accuracy, depending on the desired level of accuracy. The gains in computational cost measured for the presented results were close to a factor of 2 (more than half the cost for the same level of error) for the CENO4-RK2 scheme, but some observations are required. There is a tolerance that is associated with reading the flame heights from the contours, which can be said to be within 2 mm, that is the scale used for the y-axis in the contours. Also, the errors for each height are averaged, and despite collapsing within a relatively narrow range compared to the total flame height for most cases, for some cases the difference between heights are of the order of 5 mm. It is recognized that variations of this order can affect the shape of the

averaged error curves for the different schemes, potentially changing the exact effect in the cost. Rather than focusing on the absolute numbers obtained the results presented here are in line with the trends expected for the application of high-order numerical schemes: higher accuracy for the same mesh, higher cost per cell, competitive/winning overall computational cost for same accuracy at low level of errors. This certainly encourages further research on the application of high-order schemes to combustion problems, specially if combined with other cost optimization techniques, which is foreseen to be the path for even more significant savings.

5.2 Summary of the Contributions of the Present Work

This study represents the first implementation of the compressible, high-order CENO finite-volume scheme for the LES of reactive flows using a PCM-FPI chemistry model. The goals of the present work were to implement and assess the capabilities of the high-order scheme for a turbulent premixed laboratory flame. The main contributions of this research are:

- Implementation and testing of the trilinear transformation within the high-order finite-volume framework, extending the ability of the code to handle non-orthogonal hexahedral elements;
- Development and extension of the high-order framework to handle reactive flows by implementing a high-order version of the solver for the LES of turbulent premixed flames using the PCM-FPI model (tabulated chemistry coupled with a presumed PDF);
- Performance of the first high-order CENO scheme LES computation of a laboratory-scale premixed flames of a Bunsen-type flame. The LES results represent the first application of the high-order CENO scheme to reactive flows using a fully compressible formulation;
- A systematic cost assessment was performed comparing the fourth-order spatial scheme, third-order spatial scheme and second-order spatial scheme using different mesh refinements for the premixed Bunsen burner laboratory flame. This allowed the identification of the benefits of the high-order scheme in reducing the error for a given spatial resolution and reducing the overall computational cost required to achieve lower errors according to the solution quality criteria adopted here based on flame height.

5.2.1 Suggestions for Future Work

Following the encouraging results obtained here, several different paths of further research can be anticipated. The first suggestion is the extension of the sensitivity tests in order to improve

the understanding how the different components of the high-order method (reconstruction polynomial, stencil size, quadrature rule) are affecting the overall cost and accuracy for this problem. By keeping some of the variables constant and varying others in a controlled way the cost versus error curve can be assessed and the sensitivity to these variables better understood.

Aiming at the solution of more complicated geometries, the extension of the high-order CENO method for reactive flows to unstructured mesh is foreseen as a very useful development. Due to the modularity of the implementation used here, this task is somewhat independent of the system of equations being solved. Basically, it would require a unstructured bookkeeping of neighbours, building a connectivity matrix and the overhead would lie in the definition of the stencils for each cell, which is basically a pre-processing step. The cell operations would require update to deal with tetrahedral cells which is also relatively transparent to the whole high-order CENO implementation.

Another suggestion is the combination of the high-order CENO scheme with adaptive mesh refinement (AMR) for combustion problems. This combination has been implemented and successfully tested for viscous flows [177] and for 3D Magneto-Hydrodynamics simulations [2], demonstrating that substantial savings can be achieved.

The LES implementation used here, relying on a implicit filtering based on the mesh size, is subject to commutation errors of order $\mathcal{O}(\Delta^2)$ [178]. In order to achieve a formally fully high-order implementation, the study of high-order commutative filters should also be considered in future studies. The effect of using explicit high-order filtering could then be evaluated in comparison to the alternative implicit approach used here. One theory for constructing explicit discrete, high-order, commutative filters has been proposed by Vasilyev *et al.* [179]. The development of explicit filters in three dimensions has been previously considered for the LES of compressible flows by Deconinck [171] using the same computational framework of the present work. The extension and application of those findings to the LES of reactive problems is also anticipated.

References

[1] N. Peters. *Turbulent Combustion*. Cambridge University Press, Cambridge, 1st edition, 2000.

[2] L. Ivan, A. Susanto, H. De Sterck, and C.P.T. Groth. High-order Central ENO finite-volume scheme for MHD on three-dimensional cubed-sphere grids. In *Seventh International Conference on Computational Fluid Dynamics (ICCFD7)*, page 1, July 2012.

[3] T.C. Yuen and Ö.L. Gülder. Premixed turbulent flame front structure investigation by rayleigh scattering in the thin reaction zone regime. In *Proceedings of the Combustion Institute*, volume 32, pages 1747–1754, 2009.

[4] IEA. World Energy Outlook 2012. Technical report, International Energy Agency, 2012.

[5] Department of Energy. Basic research needs for clean and efficient combustion of 21^{st} century transportation fuels. http://science.energy.gov/~/media/bes/pdf/reports/files/ctf_rpt.pdf, 2006.

[6] United Nations Intergovernmental Panel on Climate Change. Climate change 2013 - the physical science basis, 2013.

[7] Embraer S.A, Boeing S.A, FAPESP and UNICAMP. Flightpath to aviation biofuels in Brazil: Roadmap for sustainable aviation biofuels in Brazil, 2013.

[8] International Civil Aviation Organization (ICAO). The challenges for the development and deployment of sustainable alternative fuels in aviation, 2013.

[9] Azul linhas aereas realiza voo experimental bem sucedido com biocombustivel. `http://www.embraer.com/en-US/ImprensaEventos/Press-releases/noticias/Pages/Azul-Linhas-Aereas-realiza-voo-experimental-bem-sucedido-com-biocombustivel.aspx`, 2012. Accessed: 2015-01-30.

[10] R.W. Bilger. The role of combustion technology in the 21st century. In T. Echekki and E. Mastorakos, editors, *Turbulent Combustion Modeling Advances, New Trends and Perspectives*, Fluid Mechanics and its Applications, pages 3–18. Springer, 2011.

[11] J. G. McDonald and C. P. T. Groth. Numerical modeling of micron-scale flows using the gaussian moment closure. Paper 2005-5035, AIAA, June 2005.

[12] G. A. Bird. *Molecular Gas Dynamics and the Direct Simulation of Gas Flows*. Clarendon Press, Oxford, 1994.

[13] H. Lomax, T. Pulliam, and D. Zingg. *Fundamentals of Computational Fluid Dynamics*. Springer-Verlag, New York, 2001.

[14] Z.J. Wang, K. Fidkowski, R. Abgrall, F. Bassi, D. Caraeni, A. Cary, H. Deconinck, R. Hartmann, K. Hillewaert, H.T. Huynh, N. Kroll, G. May, P. Persson, B. van Leer, and M. Visbal. High-order CFD methods: current status and perspective. *International Journal for Numerical Methods in Fluids*, 72(8):811–845, 2013.

[15] A. Jameson. A proof of the stability of the spectral difference method for all orders of accuracy. *Journal of Scientific Computing*, 45:348–358, 2010.

[16] A. Harten, B. Enquist, S. Osher, and S. R. Chakravarthy. Uniformly high order accurate essentially non-oscillatory schemes, iii. *Journal of Computational Physics*, 71:231–303, 1987.

[17] L. Ivan and C. P. T. Groth. High-order Central ENO finite-volume scheme with adaptive mesh refinement. Paper 2007-4323, AIAA, June 2007.

[18] G.-S. Jiang and C.-W. Shu. Efficient implementation of weighted ENO schemes. *Journal of Computational Physics*, 126:202–228, 1996.

[19] O. Friedrich. Weighted essentially non-oscillatory schemes for the interpolation of mean values on unstructured grids. *Journal of Computational Physics*, 144:194–212, 1998.

[20] C. Hu and C.-W. Shu. Weighted essentially non-oscillatory schemes on triangular meshes. *Journal of Computational Physics*, 150:97–127, 1999.

[21] T. J. Barth. Recent developments in high order k-exact reconstruction on unstructured meshes. Paper 93-0668, AIAA, January 1993.

[22] T. J. Barth and P. O. Fredrickson. Higher order solution of the Euler equations on unstructured grids using quadratic reconstruction. Paper 90-0013, AIAA, January 1990.

[23] L. Ivan and C. P. T. Groth. High-order Central ENO finite-volume scheme with adaptive mesh refinement. Paper 2007-4323, AIAA, June 2007.

[24] R. Rashad. Development of a high-order finite-volume method for the Navier-Stokes equations in three dimensions. Master's thesis, University of Toronto, 2009.

[25] S. De Rango and D.W. Zingg. Higher-order spatial discretization for turbulent aerodynamic computations. *AIAAJ*, 39:1296–1304, 2001.

[26] Chi-Wang Shu. High-order finite difference and finite volume WENO schemes and discontinuous Galerkin methods for CFD. *International Journal of Computational Fluid Dynamics*, 17(2):107–118, 2003.

[27] S. van der Hoeven, B. Boersma, H. J.J. Jonker, and D. J. E. M. Roekaerts. Development of a large eddy simulation code for turbulent non-premixed jet flames. In *2nd ECCOMAS Thematic Conference on Computational Combustion*, TU Delft, 2007.

[28] L. Vervisch, R. Hauguel, P. Domingo, and M. Rullaud. Three facets of turbulent combustion modelling: DNS of premixed V-flame, LES of lifted nonpremixed flame and RANS of jet-flame. *Journal of Turbulence*, 4:1–36, 2004.

[29] B. Cockburn and C-W. Shu. TVB Runge-Kutta local projection discontinous Galerkin finite-element method for conservation laws II: General framework. *Mathematics of Computation*, 52:411, 1989.

[30] B. Cockburn, S.-Y. Lin, and C-W. Shu. TVB Runge-Kutta local projection discontinous Galerkin finite-element method for conservation laws III: One-dimensional systems. *Journal of Computational Physics*, 84:90, 1989.

[31] F. Bassi and S.Rebay. High-order accurate discontinuous finite element solution of the 2D euler equations. *Journal of Computational Physics*, 138:251–285, 1997.

[32] J. Yan and C.-W. Shu. Local discontinuous Galerkin methods for partial differential equations with higher order derivatives. *Journal of Scientific Computing*, 17(1-4):27–47, 2002.

[33] G.J. Gassner, F. Lörcher, C.-D. Munz, and J.S. Hesthaven. Polymorphic nodal elements and their application in discontinuous Galerkin methods. *Journal of Computational Physics*, 228(5):1573 – 1590, 2009.

[34] S. A. Orszag. Analytical theories of turbulence. *Journal of Fluid Mechanics*, 41:363–386, 1970.

[35] D.C. Wilcox. *Turbulence Modeling for CFD*. DCW Industries, 2006.

[36] H. Pitsch. Large-eddy simulation of turbulent combustion. *Annual Review of Fluid Mechanics*, 38:453–482, 2006.

[37] B. Cuenot. The flamelet model. In T. Echekki and E. Mastorakos, editors, *Turbulent Combustion Modeling Advances, New Trends and Perspectives*, Fluid Mechanics and its Applications, pages 3–62. Springer, 2011.

[38] T. Echekki and E. Mastorakos. Turbulent combustion: Concepts, governing equations and modeling strategies. In T. Echekki and E. Mastorakos, editors, *Turbulent Combustion Modeling Advances, New Trends and Perspectives*, Fluid Mechanics and its Applications, pages 19–39. Springer, 2011.

[39] C.D. Pierce and P Moin. Progress variable approach for large-eddy simulation of non-premixed turbulent combustion. *Journal of Fluid Mechanics*, 504:73–97, 2004.

[40] S. Cant. RANS and LES modelling of premixed turbulent combustion. In T. Echekki and E. Mastorakos, editors, *Turbulent Combustion Modeling Advances, New Trends and Perspectives*, Fluid Mechanics and its Applications, pages 63–90. Springer, 2011.

[41] J. A. Van Oijen and L. P. H. De Goey. Modeling of premixed laminar flames using flamelet-generated manifolds. *Combustion Science and Technology*, 161:113–137, 2000.

[42] Olivier Gicquel, Nasser Darabiha, and Dominique Thévenin. Laminar premixed hyrogen/air counterflow flame simulations using flame prolongation of ILDM with differential diffusion. In *Proceedings of the Combustion Institute*, volume 28, pages 1901–1908, 2000.

[43] M. Yaldizli, K. Mehravaran, and F.A. Jaberi. Large-eddy simulations of turbulent methane jet flames with filtered mass density function. *International Journal of Heat and Fluid Flow*, 53(11–12):2551–2562, 2010.

[44] G. Albouze, T. Poinsot, and L. Y. M. Gicquel. Chemical kinetics modelisation and LES combustion model effects on a perfectly premixed burner. In *Compte Rendus de Mecanique*, volume 337, 6-7, pages 318–328, 2009.

[45] T. Poinsot. Using LES to study reacting flows and instabilities in annular combustion chambers. In *8th International ERCOFTAC Symposium on Engineering Turbulence Modelling and Measurements (ETMM)*, 2010.

[46] B. Franzelli, E. Riber, L.Y.M. Gicquel, and T. Poinsot. Large Eddy Simulation modelling of combustion instabilities in a lean partially premixed swirled flame. *Combustion and Flame*, 159:621–637, 2012.

[47] O. Desjardins, G. Blanquart, G. Balarac, and H. Pitsch. High order conservative finite difference scheme for variable density low mach number turbulent flows. *Journal of Computational Physics*, 227(15):7125 – 7159, 2008.

[48] Peter Gerlinger. Multi-dimensional limiting for high-order schemes including turbulence and combustion. *Journal of Computational Physics*, 231(5):2199 – 2228, 2012.

[49] M.R.H. Sheikhi, T.G. Drozda, P. Givi, F.A. Jaberi, and S.B. Pope. Large eddy simulation of a turbulent nonpremixed piloted methane jet flame (Sandia flame D). *Proceedings of the Combustion Institute*, 30:549–556, 2005.

[50] Y. Lv and M. Ihme. Higher-order discontinuous galerkin method for application to realistic combustion problems. In *14th International Conference on Numerical Combustion*, volume 32, San Antonio, USA, 2013.

[51] L.D. Owen, S.M. Guzik, and X. Gao. A high-order adaptive algorithm for multispecies gaseous flows on mapped domains. *Computers and Fluids*, 170:249–260, 2018.

[52] C. P. T. Groth and S. A. Northrup. Parallel implicit adaptive mesh refinement scheme for body-fitted multi-block mesh. Paper 2005-5333, AIAA, June 2005.

[53] S. A. Northrup and C. P. T. Groth. Parallel implicit adaptive mesh refinement scheme for unsteady fully-compressible reactive flows. Paper 2013-2043, AIAA, June 2013.

[54] S. A. Northrup and C. P. T. Groth. Solution of laminar combusting flows using a parallel implicit adaptive mesh refinement algorithm. Fourth International Conference on Computational Fluid Dynamics, Ghent, Belgium, July 10–14, 2006, July 2006.

[55] S. A. Northrup and C. P. T. Groth. Prediction of unsteady laminar flames using a parallel implicit adaptive mesh refinement algorithm. In *Proceedings of the U. S. National Combustion Meeting, Ann Arbor, Michigan, U.S.A., May 17–20, 2009*, page paper 23H3, 2009.

[56] S. A. Northrup. *A Parallel Implicit Adaptive Mesh Refinement Algorithm for Predicting Unsteady Fully-Compressible Reactive Flows*. PhD thesis, University of Toronto, 2013.

[57] X. Gao and C. P. T. Groth. A parallel adaptive mesh refinement algorithm for predicting turbulent non-premixed combusting flows. *International Journal of Computational Fluid Dynamics*, 20(5):349–357, 2006.

[58] X. Gao and C. P. T. Groth. Parallel adaptive mesh refinement scheme for turbulent non-premixed combusting flow prediction. Paper 2006-1448, AIAA, January 2006.

[59] X. Gao and C. P. T. Groth. A parallel solution-adaptive method for three-dimensional turbulent non-premixed combusting flows. *Journal of Computational Physics*, 229(5): 3250–3275, 2010.

[60] X. Gao. *A Parallel Solution-Adaptive Method for Turbulent Combusting Flows.* PhD thesis, University of Toronto, September 2008.

[61] L. Ivan and C. P. T. Groth. High-order Central ENO finite-volume scheme with adaptive mesh refinement for the advection-diffusion equation. In *Proceedings of the 5th International Conference on Computational Fluid Dynamics, Seoul, Korea, July 7–11*, 2008.

[62] L. Ivan and C. P. T. Groth. High-order solution-adaptive central essentially non-oscillatory (CENO) method for viscous flows. *Journal of Computational Physics*, 257:830–862, 2013.

[63] M.R.J. Charest, C.P.T. Groth, and P.Q. Gauthier. High-order CENO finite-volume scheme for low-speed viscous flows on three-dimensional unstructured mesh. In *Seventh International Conference on Computational Fluid Dynamics (ICCFD7)*, page 1, July 2012.

[64] F. E. Hernández-Pérez, F. T. C. Yuen, C. P. T. Groth, and Ö.L̃. Gülder. LES of a laboratory-scale turbulent premixed Bunsen flame using FSD, PCM-FPI and thickened flame models. *Proceedings of the Combustion Institute*, 33:1365–1371, 2011.

[65] F. E. Hernández-Pérez, C. P. T. Groth, and Ö. L. Gülder. LES of a hydrogen-enriched lean turbulent premixed flame. Paper 2013-1139, AIAA, January 2013.

[66] F. E. Hernández-Pérez, C. P. T. Groth, and Ö. L. Gülder. Assessment of flamelet-based subfilter-scale models for LES of turbulent premixed combustion with comparisons to laboratory-scale flames. submitted to Combustion and Flame, March 2013.

[67] M. M. Salehi, W. K. Bushe, N. Shahbazian, and C. P. T. Groth. Modified laminar flamelet presumed probability density function for LES of premixed turbulent combustion. *Proceedings of the Combustion Institute*, 34:1203–1211, 2013.

[68] N. Shahbazian, C. P. T. Groth, and Ö. L. Gülder. Assessment of presumed PDF models for large eddy simulation of turbulent premixed flames. Paper 2011-781, AIAA, January 2011.

[69] F.E. Hernàndez-Pérez. *Subfilter Scale Modelling for Large Eddy Simulation of Lean Hydrogen-Enriched Turbulent Premixed Combustion.* PhD thesis, University of Toronto, 2011.

[70] P. K. Jha and C. P. T. Groth. Parallel adaptive mesh refinment scheme with presumed conditional moment and FPI tabulated chemistry for turbulent non-premixed combustion. Paper, AIAA, January 2011-0281.

[71] P. K. Jha. *Modelling Detailed-Chemistry Effects on Turbulent Diffusion Flames Using a Parallel Solution-Adaptive Scheme.* PhD thesis, University of Toronto, October 2011.

[72] T. Poinsot and D. Veynante. *Theoretical and Numerical Combustion.* R.T. Edwards Inc., 2005.

[73] D. Veynante and Luc Vervisch. Turbulent combustion modeling. *Progress in Energy and Combustion Science*, 28:193–266, 2002.

[74] S. Turns. *An Introduction to Combustion.* McGraw-Hill, New York, 2000.

[75] S. Gordon and B. J. McBride. Computer program for calculation of complex chemical equilibrium compositions and applications I. analysis. Reference Publication 1311, NASA, 1994.

[76] B. J. McBride and S. Gordon. Computer program for calculation of complex chemical equilibrium compositions and applications ii. users manual and program description. Reference Publication 1311, NASA, 1996.

[77] C. R. Wilke. A viscosity equation for gas mixtures. *Journal of Chemical Physics*, 18: 517–519, 1950.

[78] W. C. Gardiner. *Combustion Chemistry.* Springer-Verlag New York Inc., Boca Raton, 1984.

[79] Chung K. Law. *Combustion Physics.* Cambridge University Press, 2006.

[80] H. Tennekes and J. L. Lumley. *A First Course in Turbulence.* The MIT Press, Cambridge, Massachussets, 1983.

[81] Stephen B. Pope. *Turbulent Flows.* Cambridge University Press, Cambridge, 2000.

[82] A. N. Kolmogorov. Local structure of turbulence in an incompressible fluid for very large Reynolds number. *Comptes rendus (Doklady) de l'Academie des Scinces de l'U.S.S.R*, 31: 301–305, 1941.

[83] A. W. Skiba, T. M. Wabel, C. D. Carter, S. D. Hammack, J. E. Temme, and James F. Driscoll. Premixed flames subjected to extreme levels of turbulence part i: Flame structure and a new measured regime diagram. *Combustion and Flame*, 189:407–432, 2018.

[84] E. Garnier, N. Adams, and P. Sagaut. *Large Eddy Simulation for Compressible Flows.* Springer, 2009.

[85] J.W. Deardorf. A numerical study of three-dimensional turbulent channel flow at large Reynolds numbers. *Journal of Fluid Mechanics*, 41:453–480, 1970.

[86] M. P. Martín, U. Piomelli, and G. V. Candler. Subgrid-scale models for compressible large-eddy simulations. *Theoretical and Computational Fluid Dynamics*, 13:361–376, 2000.

[87] D. Knight, G. Zhou, N. Okong'o, and V. Shukla. Compressible large eddy simulation using unstructured grids. Paper 98-0535, AIAA, January 1998.

[88] F.E. Hernàndez-Pérez, F.T.C. Yuen, C.P.T. Groth, and Ö.L.Gulder. LES of a laboratory-scale turbulent premixed Bunsen flame using FSD, PCM-FPI and thickened flame models. *Proceedings of the Combustion Institute*, 33:1365–1371, 2011.

[89] M. Boger, D. Veynante, H. Boughanem, and A. Trouvé. Direct numerical simulation analysis of flame surface density concept for large eddy simulation of turbulent premixed combustion. In *Proceedings of the Combustion Institute*, volume 27, pages 917–925. The Combustion Institute, 1998.

[90] U. Schumann. Subgrid scale model for finite difference simulations of turbulent flows in plane channels and annuli. *Journal of Computational Physics*, 18(4):376 – 404, 1975.

[91] A. Yoshizawa and K. Horiuti. A statistically-derived subgrid-scale kinetic energy model for large-eddy simulation of turbulent flows. *Journal of the Physical Society of Japan*, 54: 2834–2839, 1985.

[92] A. Y. Klimenko. Multicomponent diffusion of various scalars in turbulent flow. *Fluid Dynamics*, 25:327–334, 1990.

[93] R. W. Bilger. Conditional moment methods for turbulent reacting flows. *Physics of Fluids*, 5:436–444, 1993.

[94] S. B. Pope. PDF methods for turbulent reactive flows. *Progress in Energy and Combustion Science*, 11:119–192, 1985.

[95] F. T. M. Nieuwstadt and J. P. Meeder. Large-eddy simulation of air pollution dispersion: a review. In O. Métais and J. H. Ferziger, editors, *New tools in turbulence modelling*, pages 264–280. Les Editions de Physique - Springer Verlag, 1997.

[96] D. Veynante, A. Trouvé, K. N. C. Bray, and T. Mantel. Gradient and countergradient scalar transport in turbulent premixed flames. *Journal of Fluid Mechanics*, 332:263–293, 1997.

[97] D.B. Spalding. Mixing and chemical reaction in steady confined turbulent flames. *Symposium (International) on Combustion*, 13(1):649 – 657, 1971.

[98] T. D. Butler and P. J. O'Rourke. A numerical method for two dimensional unsteady reacting flows. In *Proceedings of the Combustion Institute*, pages 1503–1515. The Combustion Institute, 1977.

[99] G.Wang, M.Boileau, and D.Veynante. Implementation of a dynamic thickened flame model for large eddy simulations of turbulent premixed combustion. *Combustion and Flame*, 158: 2199– 2213, 2011.

[100] P.S. Volpiani, T. Schmitt, and D. Veynante. A posteriori tests of a dynamic thickened flame model for large eddy simulations of turbulent premixed combustion. *Combustion and Flame*, 174:166 – 178, 2016.

[101] S. B. Pope. The evolution of surfaces in turbulence. *International Journal of Engineering Science*, 26(5):445–469, 1988.

[102] S.M. Candel and T.J. Poinsot. Flame stretch and the balance equation for the flame area. *Combustion Science and Technology*, 70(1-3):1–15, 1990.

[103] E. R. Hawkes and R. S. Cant. A flame surface density approach to large-eddy simulation of premixed turbulent combustion. In *Proceedings of the Combustion Institute*, volume 28, pages 51–58. The Combustion Institute, 2000.

[104] W. Lin. *Large-Eddy Simulation of Premixed Turbulent Combustion Using Flame Surface Density Approach*. PhD thesis, University of Toronto, 2010.

[105] S. Osher and J. A. Sethian. Fronts propagating with curvature dependent speed: algorithms based on Hamilton-Jacobi formulations. *Journal of Computational Physics*, 79: 12–49, 1988.

[106] S. B. Pope. The application of PDF transport equations to turbulent reactive flows. *Journal of Non-Equilibrium Thermodynamics*, 7:1–14, 1982.

[107] D.C. Haworth and S.B. Pope. Transported probability density function methods for Reynolds-averaged and large-eddy simulations. In T. Echekki and E. Mastorakos, editors, *Turbulent Combustion Modeling Advances, New Trends and Perspectives*, Fluid Mechanics and its Applications, pages 119–142. Springer, 2011.

[108] A. Kronenburg and E. Mastorakos. The conditional moment closure. In T. Echekki and E. Mastorakos, editors, *Turbulent Combustion Modeling Advances, New Trends and Perspectives*, Fluid Mechanics and its Applications, pages 91–117. Springer, 2011.

[109] A.Y. Klimenko and R.W. Bilger. Conditional moment closure for turbulent combustion. *Progress in Energy and Combustion Science*, 25:595–687, 1999.

[110] W. K. Bushe and H. Steiner. Conditional moment closure for large eddy simulation of nonpremixed turbulent reacting flows. *Physics of Fluids*, 11:1896–1906, 1999.

[111] N. Shahbazian, M. Salehi, C. P.T. Groth, and Ö. L. Gülder. Performance of conditional source-term estimation model for LES of turbulent premixed flames in thin reaction zones regime. *Proceedings of the Combustion Institute*, 35(2):1367 – 1375, 2015.

[112] N. Shahbazian. *Subfilter Scale Combustion Modelling for Large Eddy Simulation of Turbulent Premixed Flames*. PhD thesis, University of Toronto, 2015.

[113] G. P. Smith, D. M. Golden, M. Frenklach, N. W. Moriarty, B. Eiteneer, M. Goldenberg, C. T. Bowman, R. K. Hanson, S. Song, W. C. Gardiner, V. V. Lissianski, and Z. Qin. GRI-Mech 3.0. http://www.me.berkeley.edu/gri_mech/.

[114] Zhuyin Ren, Stephen B. Pope, Alexander Vladimirsky, and John M. Guckenheimer. The invariant constrained equilibrium edge preimage curve method for the dimension reduction of chemical kinetics. *The Journal of Chemical Physics*, 124(11):114111, 2006.

[115] V. Bykov and U. Maas. The extension of the ILDM concept to reaction-diffusion manifolds. *Combustion Theory and Modelling*, 11(6):839–862, 2007.

[116] U. Maas and S.B. Pope. Simplifying chemical kinetics: Intrinsic low-dimensional manifolds in composition space. *Combustion and Flame*, 88(3-4):239 – 264, 1992.

[117] P. K. Jha and C. P. T. Groth. Evaluation of flame-prolongation of ILDM and flamelet tabulated chemistry approaches for laminar flames. Paper 2011-0206, AIAA, January 2011.

[118] B. Fiorina, R. Baron, O. Gicquel, L. Vervisch, S. Carpentier, and N. Darabiha. Modelling non-adiabatic partially premixed flames using flame-prolongation of ILDM. *Combustion Theory and Modelling*, 7:449–470, 2003.

[119] D. Goodwin and H. K. Moffat. Cantera. http://code.google.com/p/cantera/.

[120] F.E. Hernàndez-Pérez, C.P.T. Groth, and Ö.L. Gülder. Large-eddy simulation of lean hydrogen-methane turbulent premixed flames in the methane-dominated regime. *Internation Journal of Hydrogen Energy*, 39:7147 – 7157, 2014.

[121] Jéremy Galpin, Alexandre Naudin, Luc Vervich, Olivier Colin Christian Angelberger, and Pascale Domingo. Large-eddy simulation of a fuel-lean premixed turbulent swirl-burner. *Combustion and Flame*, 155:247–266, 2008.

[122] P. Domingo, L. Vervisch, S. Payet, and R. Hauguel. DNS of a premixed turbulent V flame and LES of a ducted flame using a FSD-PDF subgrid scale closure with fpi-tabulated chemistry. *Combustion and Flame*, pages 566–586, 2005.

[123] B. Fiorina, O. Gicquel, L. Vervisch, S. Carpentier, and N. Darabiha. Premixed turbulent combustion modeling using tabulated detailed chemistry and PDF. In *Proceedings of the Combustion Institute*, volume 30, pages 867–874, 2005.

[124] P. Domingo, L. Vervisch, and D. Veynante. Large-eddy simulation of a lifted methane jet flame in a vitiated coflow. *Combustion and Flame*, 152:415–432, 2008.

[125] V. Subramanian, P. Domingo, and L. Vervisch. Large eddy simulation of forced ignition of an annular bluff-body burner. *Combustion and Flame*, 157:579–601, 2010.

[126] K. N. C. Bray, M. Champion, P. A. Libby, and N. Swaminathan. Finite rate chemistry and presumed pdf models for premixed turbulent combustion. *Combustion and Flame*, 146:665–673, 2006.

[127] B. Jin, R. Grout, and W. K. Bushe. Conditional source-term estimation as a method for chemical closure in premixed turbulent reacting flow. *Flow Turbulence Combust.*, 81: 563–582, 2008.

[128] M. M. Salehi and W. K. Bushe. Presumed PDF modeling for RANS simulation of turbulent premixed flames. *Combustion Theory and Modelling*, 14:381–403, 2010.

[129] Fluent. *Fluent 6.2 User Guide*. Fluent Inc., Centerra Resource Park, 10 Cavendish Court, Lebanon, NH 03766, USA, 2005.

[130] S. Chakravarthy, O. Peroomian, U. Goldberg, and S. Palaniswamy. The CFD++ computational fluid dynamics software suite. SAE Technical Paper 985564, SAE, 1998.

[131] S. K. Godunov. Finite-difference method for numerical computations of discontinuous solutions of the equations of fluid dynamics. *Matematicheskii Sbornik*, 47:271–306, 1959.

[132] J. J. Gottlieb and C. P. T. Groth. Assessment of Riemann solvers for unsteady one-dimensional inviscid flows of perfect gases. *Journal of Computational Physics*, 78:437–458, 1988.

[133] P. L. Roe. Approximate Riemann solvers, parameter vectors, and difference schemes. *Journal of Computational Physics*, 43:357–372, 1981.

[134] A. Harten, P. D. Lax, and B. van Leer. On upstream differencing and Godunov-type schemes for hyperbolic conservation laws. *SIAM Review*, 25(1):35–61, 1983.

[135] B. Einfeldt. On Godunov-type methods for gas dynamics. *SIAM Journal on Numerical Analysis*, 25:294–318, 1988.

[136] T. Linde. A practical, general-purpose, two-state HLL Riemann solver for hyperbolic conservation laws. *International Journal for Numerical Methods in Fluids*, 40:391–402, 2002.

[137] Meng-Sing Liou. A sequel to AUSM, part II: AUSM$^+$-up for all speeds. *Journal of Computational Physics*, 214:137–170, 2006.

[138] A. Harten. Recent developments in shock-capturing schemes. Report 91-8, ICASE, January 1991.

[139] E. Hewitt and R. Hewitt. The Gibbs-Wilbraham phenomenon: An episode in Fourier analysis. *Archive for History of Exact Sciences*, 21(2):129–160, 1979. ISSN 0003-9519.

[140] E. F. Toro. *Riemann Solvers and Numerical Methods for Fluid Dynamics: A Practical Introduction*. Springer, University of London, London, 2009.

[141] M. Berger, M. Aftosmis, and S. Murman. Analysis of slope limiters on irregular grids. Paper 2005-0490, AIAA, 2005.

[142] T. J. Barth and D. C. Jespersen. The design and application of upwind schemes on unstructured meshes. Paper 89-0366, AIAA, January 1989.

[143] M. J. Berger and R. J. LeVeque. An adaptive Cartesian mesh algorithm for the Euler equations in arbitrary geometries. Paper 89-1930, AIAA, June 1989.

[144] R. Mittal and G. Iaccarino. Immersed boundary methods. *Annual Review of Fluid Mechanics*, 37(1):239–261, 2005.

[145] R.L. Naff, T.F. Russell, and J.D. Wilson. Shape functions for velocity interpolation in general hexahedral cells. *Computational Geosciences*, 6:285–314, 2002.

[146] O.C. Zienkiewicz and R.L. Taylor. *The Finite Element Method*, volume 1. Butterworth-Heinemann, fifth edition, 2000.

[147] C. A. Felippa. A compendium of FEM integration formulas for symbolic work. *Eng. Comput.*, 21(8):867–890, 2004.

[148] L. Ivan and C. P. T. Groth. High-order central ENO scheme for hyperbolic conservation laws on body-fitted multi-block mesh. In *Proceedings of the 14th Annual Conference of the CFD Society of Canada, Kingston, Ontario, Canada, July 16-18, 2006*, pages 317–324. CFD Society of Canada, 2006.

[149] L. Ivan and C. P. T. Groth. High-order finite-volume scheme with adaptive mesh refinement. In *Proceedings of the 54th Annual Conference Aerodynamics Symposium of the Canadian Aeronautics and Space Institute, Toronto, Canada, April 24–26, 2007*. CASI, to be published, 2007.

[150] A. Harten. High resolution schemes for hyperbolic conservation laws. *Journal of Computational Physics*, 49:357–393, 1983.

[151] A. Harten. On a class of high resolution total-variation-stable finite-difference schemes. *SIAM Journal on Numerical Analysis*, 21:1–23, 1984.

[152] L. Ivan, H. De Sterck, S. A. Northrup, and C. P. T. Groth. Hyperbolic conservation laws on three-dimensional cubed-sphere grids: A parallel solution-adaptive simulation framework. *Journal of Computational Physics*, 255:205–227, 2013.

[153] L. Freret, C. P. T. Groth, T. B. Nguyen, and H. De Sterck. High-order finite-volume scheme with anisotropic adaptive mesh refinement: Efficient inexact newton method for steady three-dimensional flows. Paper 2017-3297, AIAA, June 2017.

[154] L. Freret, , L. Ivan, H. De Sterck, and C. P. T. Groth. A high-order finite-volume method with anisotropic AMR for ideal MHD flows. Paper 2017-3297, AIAA, June 2017.

[155] M. R.J. Charest, C. P. T. Groth, and P.Q. Gauthier. A high-order central eno finite-volume scheme for three-dimensional low-speed viscous flows on unstructured mesh. *Communications in Computational Physics*, 17:615–656, 2015.

[156] A. Harten and S. R. Chakravarthy. Multi-dimensional ENO schemes for general geometries. Report 91-76, ICASE, September 1991.

[157] J. G. McDonald, M. R.J. Charest, and C. P. T. Groth. High-order ceno finite-volume schemes for multi-block unstructured mesh. Paper 2011-3854, AIAA, 2011.

[158] C. F. Ollivier-Gooch. High-order ENO schemes for unstructured meshes based on least-squares reconstruction. Paper 97-0540, AIAA, January 1997.

[159] K. Nicholson. *Linear Algebra With Applicaitons*. PWS Publishing Company, Boston, 1995.

[160] G.H. Golub and C.F. van Loan. *Matrix Computations*. The Johns Hopkins University Press, Baltimore, USA, 2013.

[161] C. F. Ollivier-Gooch. Quasi-ENO schemes for unstructured meshes based on unlimited data-dependent least-squares reconstruction. *Journal of Computational Physics*, 133:6–17, 1997.

[162] C. Hirsch. *Numerical Computation of Internal and External Flows, Volume 2, Computational Methods for Inviscid and Viscous Flows*. John Wiley & Sons, Toronto, 1990.

[163] C. F. Ollivier-Gooch and M. Van Altena. A high-order accurate unstructured mesh finite-volume scheme for the advection-diffusion equation. *Journal of Computational Physics*, 181(2):729–752, 2002.

[164] A. Susanto, L. Ivan, H. De Sterck, and C.P.T. Groth. High-order central ENO finite-volume scheme for ideal MHD. *Journal of Computational Physics*, 250(0):141 – 164, 2013.

[165] C. K. S. Lam and C. P. T. Groth. Numerical prediction of three-dimensional non-equilibrium gaseous flows using the Gaussian moment closure. Paper 2011-3401, AIAA, June 2011.

[166] X. Gao and C. P. T. Groth. A parallel adaptive mesh refinement algorithm for predicting turbulent non-premixed combusting flows. *International Journal of Computational Fluid Dynamics*, 20(5):349–357, 2006.

[167] W. Gropp, E. Lusk, and A. Skjellum. *Using MPI*. MIT Press, Cambridge, Massachussets, 1999.

[168] S. A. Northrup. A parallel adaptive-mesh refinement scheme for predicting laminar diffusion flames. Master's thesis, University of Toronto, 2004.

[169] L. Freret, L. Ivan, and H. De Sterck C. P. T. Groth. High-order finite-volume method with block-based AMR for magnetohydrodynamics flows. *Journal of Scientific Computing*, 2018.

[170] R. Abgrall. On essentially non-oscillatory schemes on unstructured meshes: Analysis and implementation. *Journal of Computational Physics*, 114:45–58, 1994.

[171] W. Deconinck. Design and application of discrete explicit filters for large eddy simulation of compressible turbulent flows. Master's thesis, University of Toronto, 2012.

[172] R. S. Rogallo. Numerical experiments in homogeneous turbulence. NASA Technical Memorandum 81315, 1981.

[173] P. Regmi. A high-order finite-volume scheme for large-eddy simulation of premixed flames on multi-block cartesian mesh. Master's thesis, University of Toronto, 2012.

[174] J. Smagorinski. General circulation experiments with the primitive equations. i: The basic experiment. *Monthly Weather Review*, 91(3):99–164, 1963.

[175] D. C. Haworth and T. J. Poinsot. Numerical simulations of Lewis number effects in turbulent premixed flames. *Journal of Fluid Mechanics*, 244:405–436, 1992.

[176] P. Tamadonfar and Ö.L.Gulder. Flame brush characteristics and burning velocities of premixed turbulent methane/air bunsen flames. *Combustion and Flame*, 161:3154 – 3165, 2014.

[177] L. Ivan and C. P. T. Groth. High-order central ENO scheme with adaptive mesh refinement for hyperbolic conservation laws. *Communications in Computational Physics*, 2013. submitted for publication.

[178] S. Ghosal and P. Moin. The basic equations for the large eddy simulation of turbulent flows in complex geometry. *Journal of Computational Physics*, 118:24–37, 1995.

[179] O. V. Vasilyev, T. S. Lund, and P. Moin. A general class of commutative filters for LES in complex geometries. *Journal of Computational Physics*, 146:82–104, 1998.